Vector Boson Scattering Processes: Status and Prospects

Diogo Buarque Franzosi (ed.)[g,d], Michele Gallinaro (ed.)[h], Richard Ruiz (ed.)[i], Thea K. Aarrestad[c], Mauro Chiesa[o], Flavia Cetorelli[l], Antonio Costantini[k], Ansgar Denner[t], Stefan Dittmaier[f], Robert Franken[t], Pietro Govoni[l], Tao Han[p], Ashutosh V. Kotwal[a], Jinmian Li[r], Kristin Lohwasser[q], Kenneth Long[c], Yang Ma[p], Luca Mantani[k], Matteo Marchegiani[e], Mathieu Pellen[f], Giovanni Pelliccioli[t], Karolos Potamianos[n], Jürgen Reuter[b], Timo Schmidt[t], Christopher Schwan[m], Michał Szleper[s], Rob Verheyen[j], Keping Xie[p], Rao Zhang[r]

[a]*Department of Physics, Duke University, Durham, NC 27708, USA*
[b]*Deutsches Elektronen-Synchrotron (DESY) Theory Group, Notkestr. 85, D-22607 Hamburg, Germany*
[c]*European Organization for Nuclear Research (CERN) CH-1211 Geneva 23, Switzerland*
[d]*Department of Physics, Chalmers University of Technology, Fysikgården 1, 41296 Göteborg, Sweden*
[e]*Swiss Federal Institute of Technology (ETH) Zürich, Otto-Stern-Weg 5, 8093 Zürich, Switzerland*
[f]*Universität Freiburg, Physikalisches Institut, Hermann-Herder-Straße 3, 79104 Freiburg, Germany*
[g]*Physics Department, University of Gothenburg, 41296 Göteborg, Sweden*
[h]*Laboratório de Instrumentação e Física Experimental de Partículas (LIP), Lisbon, Av. Prof. Gama Pinto, 2 - 1649-003, Lisboa, Portugal*
[i]*Institute of Nuclear Physics, Polish Academy of Sciences, ul. Radzikowskiego, Cracow 31-342, Poland*
[j]*University College London, Gower St, Bloomsbury, London WC1E 6BT, United Kingdom*
[k]*Centre for Cosmology, Particle Physics and Phenomenology (CP3),*
Université Catholique de Louvain, Chemin du Cyclotron, B-1348 Louvain la Neuve, Belgium
[l]*Milano - Bicocca University and INFN, Piazza della Scienza 3, Milano, Italy*
[m]*Tif Lab, Dipartimento di Fisica, Università di Milano and INFN, Sezione di Milano, Via Celoria 16, 20133 Milano, Italy*
[n]*Department of Physics, University of Oxford, Clarendon Laboratory, Parks Road, Oxford OX1 3PU, UK*
[o]*Dipartimento di Fisica, Università di Pavia and INFN, Sezione di Pavia, Via A. Bassi 6, 27100 Pavia, Italy*
[p]*Pittsburgh Particle Physics, Astrophysics, and Cosmology Center, Department of Physics and Astronomy,*
University of Pittsburgh, Pittsburgh, PA 15260, USA
[q]*Department of Physics, Sheffield University, UK*
[r]*College of Physics, Sichuan University, Chengdu 610065, China*
[s]*National Center for Nuclear Research, ul. Pasteura 7, 02-093 Warszawa, Poland*
[t]*Universität Würzburg, Institut für Theoretische Physik und Astrophysik, Emil-Hilb-Weg 22, 97074 Würzburg, Germany*

Abstract

Insight into the electroweak (EW) and Higgs sectors can be achieved through measurements of vector boson scattering (VBS) processes. The scattering of EW bosons are rare processes that are precisely predicted in the Standard Model (SM) and are closely related to the Higgs mechanism. Modifications to VBS processes are also predicted in models of physics beyond the SM (BSM), for example through changes to the Higgs boson couplings to gauge bosons and the resonant production of new particles. In this review, experimental results and theoretical developments of VBS at the Large Hadron Collider, its high luminosity upgrade, and future colliders are presented.

Keywords: Standard Model, Beyond Standard Model, Vector Boson Scattering, Vector Boson Fusion, Colliders

arXiv:2106.01393v2 [hep-ph] 15 Apr 2022

Contents

April 18, 2022

Part I
Introduction

The importance of the vector boson scattering (VBS) and vector boson fusion (VBF) processes in understanding the electroweak (EW) sector is well-established in high energy physics. At scattering energies far above the EW scale, the longitudinal modes of the weak bosons are manifestations of the Nambu-Goldstone bosons originating from the spontaneous breaking of EW symmetry. Probing their interactions therefore helps unveil the dynamics behind the Higgs mechanism [1, 2, 3, 4]. Moreover, VBS is relevant to testing the gauge structure of EW interactions due to the contribution of quartic interactions and their interplay with trilinear couplings, which leads to potentially large gauge cancellations. These are unique features of VBS processes. It is thus extremely important to achieve precise predictions in the Standard Model (SM) of particle physics as well extensively investigate beyond-the-Standard Model (BSM) scenarios, both in the context of specific models and effective field theory (EFT) frameworks. The importance of VBS physics has also been well-documented in the literature as reviewed by Refs. [5, 6, 7, 8, 9, 10].

Measurement of VBS processes are at last possible at the Large Hadron Collider (LHC), where the unprecedented energies and integrated luminosities of data sets allowed for the first observations of such rare interactions [11, 12, 13, 14, 15]. The Run 3 of the LHC's data taking is scheduled to start in 2022. And with the High-Luminosity extension (HL-LHC), the available data will enable the community to move beyond first observations and into the domain of precision measurements, aiming at the ambitious goal of isolating the transverse and longitudinal components of VBS. Future colliders can likewise improve this picture in several aspects, including direct exploration of when EW symmetry is approximately restored.

In light of the experimental, phenomenological, and theoretical advancements surrounding VBS, as well as the mandates of the 2020 European Strategy Update [16, 17], it is timely to produce a picture of the current state-of-the art in the field with a focus on the instruments and concepts that will be needed for future developments. We start in Part II, where current measurements and analysis techniques of VBS are summarized. In Part III, projections for the HL-LHC are reviewed for both the SM and BSM scenarios. In Part IV, the nature of VBS processes itself and prospects for measurements at future colliders are discussed. Finally, we conclude with an outlook in Part V.

Part II
VBS at the LHC

1 Current results on VBS from the LHC

At the LHC, the ATLAS and CMS Collaborations first studied diboson production via VBS in the $W^\pm W^\pm$, $W\gamma$, and $Z\gamma$ fi-

nal states at $\sqrt{s} = 8$ TeV in the LHC Run 1 [18, 19, 20, 21, 22, 23, 24] using the leptonic decay modes of weak bosons. These states were further investigated during the first full year of data taking at 13 TeV, when the $W^{\pm}W^{\pm}$, WZ, and ZZ channels were first observed [11, 12, 13, 14, 15], also using the leptonic decay modes. The first study of VBS using semi-leptonic decays was also made with this data set, targeting WZ/WW events where one of the boson decays to a boosted hadronic jet. A summary of these results can be found in Ref. [25] and references therein.

With the nearly $\mathcal{L} = 140$ fb^{-1} of data collected by each of the ATLAS and CMS collaborations during the LHC's second run of data-taking (Run 2), the experimental outlook for searches and measurements of VBS processes is very bright. The initial searches have rapidly been extended, with several results reaching high-statistical significance for observation and becoming measurements in their own right. In particular, the WZ and $W^{\pm}W^{\pm}$ processes have been observed and measured differentially [11, 15]. The search for the VBS ZZ production with leptonic decays was also updated with $\mathcal{L} = 137$ fb^{-1} by CMS [26, 27], exceeding the 3σ threshold for evidence but not yet reaching a 5σ observation. A 5σ observation of ZZ in the leptonic channels was achieved with $\mathcal{L} = 139$ fb^{-1} by ATLAS [28]. In addition, the first experimental search for polarized VBS production was performed in the $W^{\pm}W^{\pm}$ channel [29], a measurement widely considered a major priority for the HL-LHC. Additional results with $\mathcal{L} = 137$ fb^{-1} have been released [30, 31] and others are expected soon.

The following summary briefly discusses the current state of the experimental studies of VBS processes. While some focus is placed on results obtained by the CMS collaboration, comparable findings have been achieved by ATLAS. It is worth stressing that having results from both experiments is of utmost importance for addressing the physics goals of the LHC program and the high-energy community as a whole. Further details can be found in the relevant references.

1.1 Results on scattering of massive vector bosons

Due to its distinctive signature and low background, the same-sign $W^{\pm}W^{\pm} \rightarrow W^{\pm}W^{\pm} \rightarrow \ell_i^{\pm}\ell_j^{\pm}\nu\nu$ process is the "golden" channel of VBS processes. Unlike other VBS modes, the quantum chromodynamics (QCD)-induced production of $W^{\pm}W^{\pm}$ events is significantly subdominant with respect to the EW contribution. Therefore, the dominant backgrounds are VBS-like events from WZ production (EW or QCD-induced) or events with non-prompt leptons imitating true same-sign lepton events. Consequently, VBS WZ production is a significant background to the $W^{\pm}W^{\pm}$ process. Because estimating the WZ process as background is analogous to measuring the VBS WZ process as signal, the CMS Collaboration has performed these measurements simultaneously, fully exploiting the nearly 140 fb^{-1} as a tool to probe the SM [32]. Similarly, ATLAS reports the observation of WZ scattering in the $3\ell\nu$ channel with a statistical significance exceeding 5σ using 36 fb^{-1} of 13 TeV data [33]; sensitivity to the semi-leptonic channel is presently at the 2.5σ level with the same data set [34].

In the CMS analysis, the $W^{\pm}W^{\pm}$ and WZ processes are treated as independent signals in a single maximum likelihood fit. The
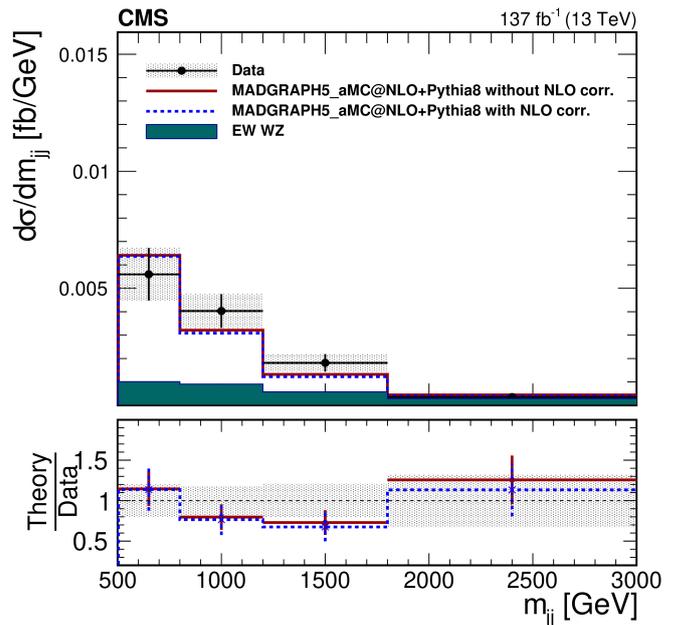
Figure 1.1: The unfolded results for the WZjj process from Ref. [32]. The contribution of the EW production and the impact of NLO EW corrections are shown.

likelihood is built from binned distributions of the invariant mass of the two VBS-tagged jets m_{jj} and the dilepton mass $m_{\ell\ell}$ in the $W^{\pm}W^{\pm}$ signal selection region, as well as from the output of a boosted decision tree (BDT) discriminant in the WZ signal region. Several observables are used as the inputs to the BDTs, including the jet and lepton transverse momenta, dilepton mass and transverse momentum, transverse WW mass, difference in azimuthal angle between leptons and between jets, and others [32]. Control regions are also used to constrain the modeling of top quark and non-prompt lepton backgrounds. The resulting measurements have a statistical significance of well over 5σ for each process, and unfolded differential distributions are produced for comparison with theoretical predictions. In particular, the impact of the next-to-leading (NLO) EW corrections, which are known to be larger than pure QCD corrections for VBS processes [35, 36, 37], are studied, as shown in Fig. 1.1. (For related details on theoretical predictions, see Section 3.)

This analysis was recently extended to perform the first study of a VBS process separated by the polarization of the vector bosons [29]. Because the polarization is not a Lorentz-invariant quantity, its definition is reference frame dependent. Therefore, the analysis independently measures the cross sections of polarized states using the polarization defined in the parton-parton center-of-mass frame and in the W boson pair center-of-mass frame. The analysis exploits BDTs trained to distinguish between the polarization states. Figure 1.2 shows the BDT score (left) and the dijet invariant mass distribution (right). The BDT distribution summarizes the discrimination of signal and background. Due to the lack of statistical power, the combined cross section for at least one longitudinally polarized boson is reported, with a statistical significance of 2.3σ (3.1σ) observed
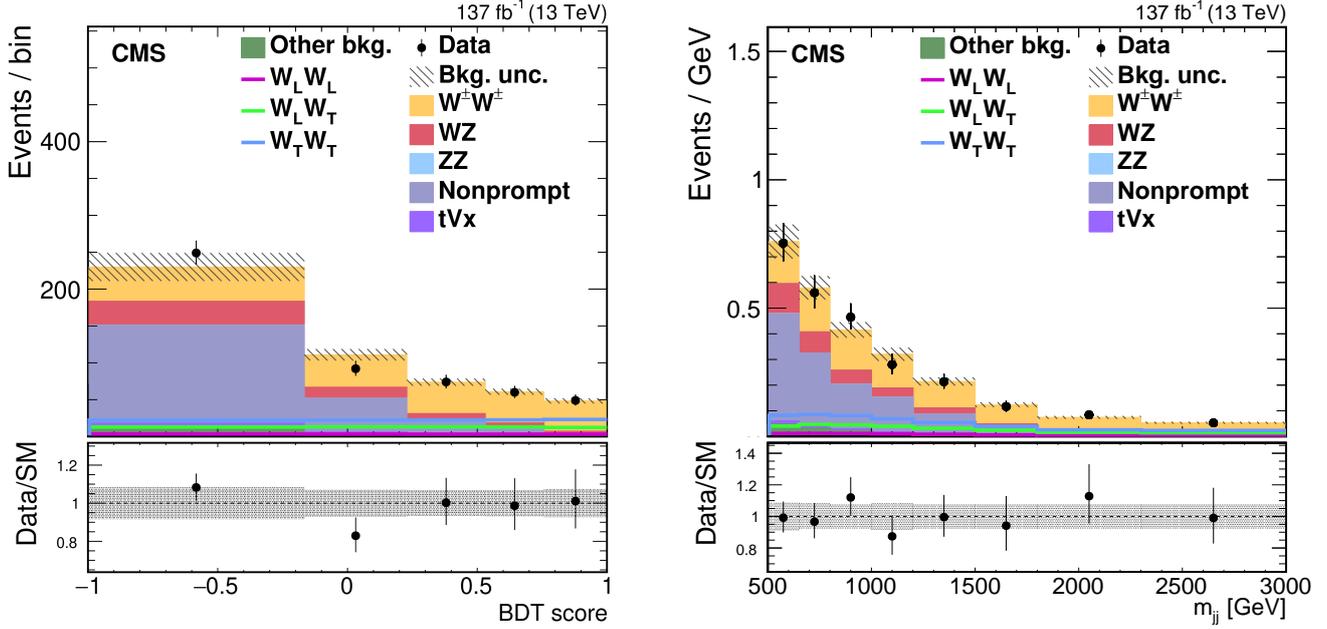
Figure 1.2: *Left:* The distribution of the BDT discriminant used to extract the signal strength for the polarized components of the *WW* cross section. *Right:* Dijet invariant mass distribution. Images from Ref. [29].

(expected) in the *WW* center-of-mass frame.

Searches have also been performed for VBS production of *ZZ* pairs [27, 28] using the full Run 2 data set. While the production rate for *ZZ* events is lower than for *WZ* and $W^{\pm}W^{\pm}$, its four-lepton signature is very clean, providing an ideal experimental handle in an otherwise complicated hadronic environment. The QCD-induced *ZZ* process is the overwhelming background in this channel, and includes a contribution from the loop-induced $gg \rightarrow ZZ$ process. This is a small component of the inclusive *ZZ* production rate but can be relevant in VBS-like regions of phase space. This contribution is estimated using state-of-the-art merged simulations for accurate modeling of the *ZZjj* state [38, 39, 40]. The analysis is driven by a matrix-element likelihood approach. The resulting measurement provides observed (expected) evidence of VBS *ZZ* production at 4.0 (3.5) standard deviations.

1.2   Results on vector boson scattering with photons

The ATLAS and CMS Collaborations have also performed measurements of the VBS production of a massive vector boson and a photon in the *Wγ* [41] and *Zγ* [42, 43, 44] channels. These measurements were performed using approximately 36 fb^{-1} or the full Run 2 data set, and exploit similar analysis strategies. Considerable backgrounds due to non-prompt photons are estimated using data-driven techniques. The QCD-induced production is the leading background in both cases. The background is estimated using Monte Carlo simulation with the normalization constrained with control regions in data. Results are extracted from a binned maximum likelihood fits, where the likelihood is built from a two-dimensional distribution of selected events (Fig. 1.3). The *Zγ* analysis from CMS exploits the m_{jj} and the rapidity separation of the tagged jets $\Delta\eta_{jj}$, whereas
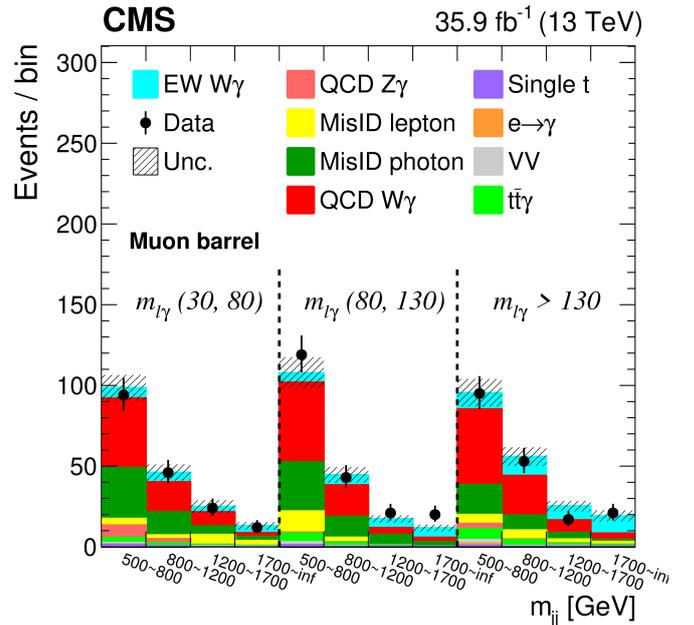
Figure 1.3: The two-dimensional distribution of m_{jj} and $m_{\ell\gamma}$ used to extract the EW *Wγ* cross section, from Ref. [41]

the m_{jj} and the photon and lepton invariant mass $m_{\ell\gamma}$ are used in the *Wγ* analysis. Results are combined with the corresponding measurements made at 8 TeV [21, 23], under the assumption of the SM production rate, to reach high statistical significance of around 5σ. Separately, ATLAS has observed the $Z\gamma \rightarrow \nu\bar{\nu}\gamma$ final state with more then 5σ statistical sensitivity [44].

1.3 Constraints on anomalous couplings

All channels are used to place constraints on anomalous dimension-8 EFT interactions. In general, the operator formulation proposed in Ref. [45] is used. Variables sensitive to the total energy of the interaction, for example, the diboson mass, are exploited to search for signs of higher-energy modifications to the vector boson interactions. A summary of the current constraints at 95% Confidence Level (C.L.) by CMS for the mixed longitudinal and transverse operator $F_{M,7}$ is shown in Fig. 1.4. Though they are not yet sensitive to the SM VBS production rates, the production of diboson events with one vector boson decaying hadronically is a particularly powerful channel for these searches due to the higher cross section from hadronic vector boson decays. Results using these final states are presented in Ref. [26]. Related constraints on anomalous couplings using VBS signatures have been reported by ATLAS using the full Run 2 data set [46].

1.4 Summary

In summary, the ATLAS and CMS Collaborations have recently produced many new results studying diboson production via VBS processes. These results include the first observations of several new processes, measurements of helicity-polarized cross sections, and constraints on anomalous couplings. Most of these measurements have exceeded the traditional metric for observations, and several have sufficient accuracy to enable unfolded results. Following the LHC Run 2, these measurements are quickly leaving the era of discovery and are approaching a new era of precision measurements. VBS measurements will soon be sensitive to the polarization fractions of the production mechanism, providing an important probe of the EW sector of the SM. For prospects at the HL-LHC, see Part 4.

2 Polarization and τ lepton studies in VBS

The study of the interactions between vector bosons offers an important test of the SM for its sensitivity to gauge boson self-couplings. It provides a direct probe of the triple and quartic gauge boson couplings. Precise measurements can shed light on the EW symmetry breaking and probe new physics processes at multi-TeV energy scales. The scattering amplitude of vector bosons, such as $V^+V^- \rightarrow V^+V^-(V = W, Z)$, is expected to increase with center-of-mass energy. Unless there is a cancellation, it will eventually diverge and will lead to a violation of unitarity [1, 2]. The divergent behavior at high energies is more acute for the scattering of longitudinally polarized vector bosons. However, this divergence is canceled by the contribution of the Higgs boson exchanges in the s and t channels, provided that the Higgs boson couplings to vector bosons are those expected in the SM. Any modification of these couplings would interfere in this delicate cancellation. If the Higgs boson's couplings to weak bosons deviate from SM predictions, cancellations may not be as effective and the diboson scattering amplitude may increase with energy.

In addition, there are many BSM scenarios that predict a cross section increase of VBS processes, through extended Higgs sectors or new resonances. Hence, VBS processes provide both a window to new physics processes as well as a constraint on fundamental Higgs boson properties and anomalous Higgs couplings. However, measuring VBS processes is experimentally challenging due to the small cross sections. VBS processes are rare and have been studied in different final states. Final states with light leptons, *i.e.*, electrons and muons, are those where the signal-over-background ratio is larger and have been studied first. However, τ leptons are more complicated to identify due to the larger backgrounds (misidentification rates for hadronic τ decays are typically one or two orders of magnitude larger than for electrons or muons) and have not been included in these studies yet.

In addition to inclusive and differential cross sections, polarization measurements of W and Z bosons in diboson production provide stringent tests of the SM and its couplings. Polarization studies provide an additional handle and a further discrimination between signal and background. In particular, the study of longitudinally polarized VBS processes, that is to say when VBS is mediated by initial- and final-state weak bosons that are in their longitudinal helicity state, is an important probe of particle interactions at the highest energies, both at the LHC and at future colliders, and it will help further understanding fundamental interactions and the SM gauge structure.

2.1 Polarization

One of the most promising ways to measure VBS processes uses events containing two leptonically-decaying, same-sign $W^\pm$ bosons produced in association with two jets, $pp \rightarrow W^\pm W^\pm jj$. However, the angular distributions of the leptons in the W boson rest frame, which are commonly used to fit polarization fractions, are not readily available in this process due to the presence of two neutrinos in the final state. Advanced analysis methods that make use of Machine Learning and other similar techniques can be used to reconstruct the angular distributions from measurable event kinematics and study the polarization fractions. It is also possible to define reference frames that are more accommodating to experimental limitations [47, 48].

Polarization measurements are not unique and depend on the reference frame in which they are defined. Polarization fractions and kinematic distributions that define polarization vectors in different reference frames have been employed. The laboratory frame is a natural choice. A definition of the polarization observables in the diboson center-of-mass frame has the advantage that the line-of-flight of the two bosons also defines the longitudinal polarization vectors, and the decay products are directly related to the scattering process. The latter may be better suited to search for deviations from the SM.

Precise calculations at the NLO in QCD of SM polarization observables are available for various multi-boson processes [49, 50, 51, 52, 53, 54]. Predictions with NLO in EW [51, 52] and at next-to-next-to-leading order (NNLO) in QCD [55] are also available, as is the automation at LO for an arbitrary scattering process [47]. Separate polarization measurements for each of the $W^\pm/Z$ bosons might be helpful in investigating CP violation in the interaction between gauge bosons. In the longer

Figure 1.4: Summary of constraints on the couplings to the EFT operator $F_{M,7}$ from experimental measurements. For details, see the URL at http://cern.ch/go/8ghC.

Plot title: aQGC Limits @95% C.L. [TeV^{-4}] — Aug 2020 — CMS, ATLAS — aC summary plots at: http://cern.ch/go/8ghC

Operator	Channel	Limits	$\int L\,dt$	$\sqrt{s}$
$f_{M,0}/\Lambda^4$	WVγ	-7.7e+01, 8.1e+01	19.3 fb^{-1}	8 TeV
	Zγ	-7.1e+01, 7.5e+01	19.7 fb^{-1}	8 TeV
	Zγ	-1.9e+01, 2.0e+01	35.9 fb^{-1}	13 TeV
	Zγ	-7.6e+01, 6.9e+01	20.2 fb^{-1}	8 TeV
	Wγ	-7.7e+01, 7.4e+01	19.7 fb^{-1}	8 TeV
	Wγ	-8.1e+01, 8.0e+00	35.9 fb^{-1}	13 TeV
	ss WW	-3.0e+00, 3.2e+00	137 fb^{-1}	13 TeV
	WZ	-5.8e+00, 5.8e+00	137 fb^{-1}	13 TeV
	γγ→WW	-2.8e+01, 2.8e+01	20.2 fb^{-1}	8 TeV
	γγ→WW	-4.2e+00, 4.2e+00	24.7 fb^{-1}	7,8 TeV
	WV ZV	-6.9e-01, 7.0e-01	35.9 fb^{-1}	13 TeV
$f_{M,1}/\Lambda^4$	WVγ	-1.3e+02, 1.2e+02	19.3 fb^{-1}	8 TeV
	Zγ	-1.9e+02, 1.8e+02	19.7 fb^{-1}	8 TeV
	Zγ	-4.8e+01, 4.7e+01	35.9 fb^{-1}	13 TeV
	Zγ	-1.5e+02, 1.5e+02	20.2 fb^{-1}	8 TeV
	Wγ	-1.2e+02, 1.3e+02	19.7 fb^{-1}	8 TeV
	Wγ	-1.2e+01, 1.2e+01	35.9 fb^{-1}	13 TeV
	ss WW	-4.7e+00, 4.7e+00	137 fb^{-1}	13 TeV
	WZ	-8.2e+00, 8.3e+00	137 fb^{-1}	13 TeV
	γγ→WW	-1.1e+02, 1.0e+02	20.2 fb^{-1}	8 TeV
	γγ→WW	-1.6e+01, 1.6e+01	24.7 fb^{-1}	7,8 TeV
	WV ZV	-2.0e+00, 2.1e+00	35.9 fb^{-1}	13 TeV
$f_{M,2}/\Lambda^4$	WVγ	-5.7e+01, 5.7e+01	20.2 fb^{-1}	8 TeV
	Zγ	-3.2e+01, 3.1e+01	19.7 fb^{-1}	8 TeV
	Zγ	-8.2e+00, 8.0e+00	35.9 fb^{-1}	13 TeV
	Zγ	-2.7e+01, 2.7e+01	20.2 fb^{-1}	8 TeV
	Wγ	-2.6e+01, 2.6e+01	19.7 fb^{-1}	8 TeV
	Wγ	-2.8e+01, 2.8e+01	35.9 fb^{-1}	13 TeV
$f_{M,3}/\Lambda^4$	WVγ	-9.5e+01, 9.8e+01	20.2 fb^{-1}	8 TeV
	Zγ	-5.8e+01, 5.9e+01	19.7 fb^{-1}	8 TeV
	Zγ	-2.1e+01, 2.1e+01	35.9 fb^{-1}	13 TeV
	Zγ	-5.2e+01, 5.2e+01	20.2 fb^{-1}	8 TeV
	Wγ	-4.3e+01, 4.4e+01	19.7 fb^{-1}	8 TeV
	Wγ	-4.4e+01, 4.4e+01	35.9 fb^{-1}	13 TeV
$f_{M,4}/\Lambda^4$	WVγ	-1.3e+02, 1.3e+02	20.2 fb^{-1}	8 TeV
	Zγ	-1.5e+01, 1.6e+01	35.9 fb^{-1}	13 TeV
	Wγ	-4.0e+01, 4.0e+01	19.7 fb^{-1}	8 TeV
	Wγ	-5.0e+00, 5.0e+00	35.9 fb^{-1}	13 TeV
$f_{M,5}/\Lambda^4$	WVγ	-2.0e+02, 2.0e+02	20.2 fb^{-1}	8 TeV
	Zγ	-2.5e+01, 2.4e+01	35.9 fb^{-1}	13 TeV
	Wγ	-6.5e+01, 6.5e+01	19.7 fb^{-1}	8 TeV
	Wγ	-8.3e+00, 8.3e+00	35.9 fb^{-1}	13 TeV
$f_{M,6}/\Lambda^4$	Zγ	-3.9e+01, 4.0e+01	35.9 fb^{-1}	13 TeV
	Wγ	-1.3e+02, 1.3e+02	19.7 fb^{-1}	8 TeV
	Wγ	-1.6e+01, 1.6e+01	35.9 fb^{-1}	13 TeV
	ss WW	-6.0e+00, 6.5e+00	137 fb^{-1}	13 TeV
	WZ	-1.2e+01, 1.2e+01	137 fb^{-1}	13 TeV
	WV ZV	-1.3e+00, 1.3e+00	35.9 fb^{-1}	13 TeV
$f_{M,7}/\Lambda^4$	Zγ	-6.1e+01, 6.3e+01	35.9 fb^{-1}	13 TeV
	Wγ	-1.6e+02, 1.6e+02	19.7 fb^{-1}	8 TeV
	Wγ	-2.1e+01, 2.0e+01	35.9 fb^{-1}	13 TeV
	ss WW	-6.7e+00, 7.0e+00	137 fb^{-1}	13 TeV
	WZ	-1.0e+01, 1.0e+01	137 fb^{-1}	13 TeV
	WV ZV	-3.4e+00, 3.4e+00	35.9 fb^{-1}	13 TeV

x-axis values: −200, 0, 200, 400, 600, 800

term, measuring the scattering of longitudinally polarized vector bosons will provide a fundamental test of the EW breaking.

Measurements of polarized cross sections for VBS processes will be an exciting component of the Run 3 and HL-LHC programs. These analyses will complement on-going LHC measurements of W polarization fractions in the W+jets process [56, 57] and in $t\bar{t}$ events [58], as well as measurements of angular coefficients of lepton pairs in Z boson production [59, 60]. Generically, distributions of angular observables are extremely sensitive to the final state considered and discrepancies from the SM predicted behavior can be used to look for the presence of new interactions. The polarization of a gauge boson can be determined from the angular distribution of its decay products. At the Born level, the expected angular distribution for massless fermions in the rest frame of the parent W boson is given in terms of its helicity fractions [61, 62, 63]. These are commonly represented by the longitudinal helicity fraction f_0, and the left-handed and right-handed transverse helicity fractions f_L and f_R, respectively.

In inclusive Z events, the angular distributions of charged lepton pairs produced via the Drell-Yan neutral current process provide a portal to precisely determine the production process through spin-correlation effects between the initial-state partons and the final-state leptons [64, 65, 66]. In this context, we briefly comment that reports by Refs. [59, 60] of apparent discrepancies between data and theory expectations for the so-called Lam-Tung relation [67], which relates angular coefficients of lepton pairs in the Drell-Yan process, can be alleviated by recent improvements to the predictions' formal accuracy [68].

Polarization measurements of the three helicity fractions of the W and Z bosons were also performed in WZ production at $\sqrt{s} = 13$ TeV [69]. Importantly, this is a stepping stone to measuring helicity fractions in triboson processes, which are related to VBS by crossing symmetry. An analysis of angular distributions of leptons from decays of W and Z bosons was performed in WZ events, and integrated helicity fractions in the detector fiducial region were measured for the W and Z bosons separately. Of particular interest, the longitudinal helicity fraction of pair-produced vector bosons was also measured. The measurements are dominated by statistical uncertainties. Nonetheless, good agreement of the measured helicity fractions of both the W and Z bosons with predictions is observed.

These studies can be extended to VBS processes and, in

particular, to VBS processes that include τ leptons in the final state. This is something that has not been done yet, but it would certainly be an important study to perform.

2.2 The τ lepton and polarization studies

Recent checks of lepton flavor universality violation have sparked renewed interest in measurements involving τ leptons [70, 71, 72, 73]. The τ lepton is the most massive lepton and a third-generation particle. It therefore plays an important role as a probe in BSM searches. Due to their large mass, τ leptons may be particularly sensitive to BSM interactions. For example: the existence of a heavy charged Higgs boson $H^\pm$ may give rise to anomalous τ lepton production in WZ scattering [74, 75, 76]. Similarly, the violation of lepton number symmetry can lead to the anomalous production of same-sign $\tau^\pm\tau^\pm$ pairs in same-sign $W^\pm W^\pm$ scattering [77, 78, 79]. Furthermore, due to its short lifetime, spin information is preserved in the decay products of τ leptons. VBS polarization studies involving τs therefore provide additional information on the underlying production processes as well as additional discriminating power against background processes.

With larger data samples in the Run 3 and HL-LHC eras it is expected that τ leptons will also be included and observed in the studies of VBS processes. The τ lepton is identified through its visible decay products, either hadrons or leptons. The hadronic decay modes of τ leptons represent approximately 65% of all τ decays, mostly in one-prong ($\approx$50%) and three-prong ($\approx$15%) decays, and are characterized by a narrow jet signature. Their identification and reconstruction are difficult and subject to larger backgrounds from incorrectly identified jets. The remaining 35% are leptonic decays, *i.e.*, decaying to electrons or muons with lower p_T and the corresponding neutrinos, and are difficult to distinguish from prompt electron and muon production.

Polarization studies incorporating VBS and τ leptons build on ongoing measurements at the LHC. For example: the τ polarization was measured by ATLAS in $W \to \tau\nu$ decays as the asymmetry of cross sections of left-handed and right-handed τ production, from the energies of the decay products in hadronic τ decays with a single final state charged particle (one prong) [80]. The resulting measurement is in agreement with SM predictions. The τ decay mode exhibiting the highest sensitivity to the τ polarization is $\tau^\pm \to h^\pm\nu$, where $h^\pm = \pi^\pm, K^\pm$, with a branching ratio of about 11.5%. In the τ rest frame, the neutrino (always left-handed) is preferentially emitted opposite to the τ spin orientation. The τ polarization value P provides insight into the Lorentz structure of the τ production mechanism, and gives an indication of the parity violation in the interaction. The angle between the τ direction of flight and the hadronic decay products in the τ rest frame is used as the primary observable sensitive to τ polarization. The τ polarization is inferred from the relative energy fraction carried by charged and neutral hadrons in the hadronic τ decays, and is measured by fitting the observed charged asymmetry distribution.

In $W \to \tau\nu$ decays, the W^+ (W^-) is expected to couple exclusively to a right(left)-handed τ^+ (τ^-) corresponding to a τ polarization of $P = +1$, up to corrections of order $O(m_\tau^2/m_W^2)$.
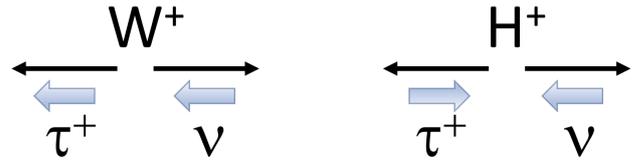
Figure 2.1: A cartoon depicting a spin-1 W boson (left) and a spin-0 charged Higgs boson (right) decaying in their rest frames to a τ lepton and a neutrino. The resulting helicity (larger light-colored shaded arrow) of the τ lepton depends on the originating boson: the τ^+ polarization is $P = +1$ ($P = -1$) if from a W^+ (H^+).

On the other hand, since neutrinos are left-handed, a Minimal Supersymmetric SM (MSSM) charged Higgs boson would couple to left(right)-handed τ^+ (τ^-) τ leptons leading to a prediction of $P = -1$. This is exemplified in Fig. 2.1. The method used for extracting the τ polarization is independent of the production mode and can be applied to other processes.

The polarization of τ leptons produced in $Z/\gamma^* \to \tau\tau$ decays was also measured [81]. Results are in agreement with SM predictions. The final state includes a hadronically decaying τ lepton with a single charged particle, accompanied by another τ decaying leptonically. The leptonic decay is used to trigger, select, and identify the candidate events, while the hadronic decay serves as a spin analyzer.

A good understanding of τ polarization is a powerful discriminating tool in these and other processes containing a τ lepton in the final state, such as same-sign $W^\pm W^\pm$ VBS and charged Higgs production. Similar studies may be performed for future measurements in the decays of the Higgs boson or other final states with high invariant masses. In particular, it may help to distinguish decays of heavy particles where the same final states involving τ leptons are predicted but with different helicity configurations, such as for separating Z and H or new bosons, or for distinguishing W and charged Higgs bosons [82]. Larger statistics to be able to properly select the desired decay modes and a good control of systematic uncertainties are necessary ingredients.

In order to enhance the sensitivity to anomalous quartic gauge couplings (aQGCs), studies of EW boson production through VBS processes include leptons and jets of large transverse momenta in the large diboson mass region m_{VV}. Specific, boosted-object reconstruction algorithms have been developed to retain high efficiency for high-p_T objects. These techniques include reconstruction of hadronically decaying τs as well as electrons, muons, jets, and bosons [83, 84]. Efforts have been deployed to study proton-proton collisions at the LHC. At future, higher energy colliders, further understanding and improvements of these reconstruction tools will become of pivotal importance to be able to fully explore the data at the highest energies.

2.3 Summary

Polarization studies of vector boson final states may provide further understanding of fundamental rules governing particle

interactions. Some polarization studies of VBS processes are discussed in Section 8. Polarization properties carry information of the interaction process and can be studied in the final-state decay products, provided an appropriate understanding of the event kinematics. Detailed studies have been performed in VBS processes and their sensitivity is limited by the size of the data samples. Large data samples are needed to properly model and disentangle the longitudinal and transverse polarization distributions, and kinematic characteristics. The τ lepton, the heaviest and perhaps the most intriguing of the leptons, is so far missing from these studies. Its inclusion will certainly offer an additional handle to probe the SM. With the larger data samples imminently expected at the LHC Run 3 and further in the future at the HL-LHC and at future colliders, the study of τ leptons in VBS process final states may provide additional sensitivity in the search for new physics processes.

3 Precise theoretical predictions for VBS

In this section we describe recent developments and challenges in making precise theoretical predictions for VBS at the LHC. We make some remarks on possible future developments.

3.1 Electroweak corrections to VBS

The increasing experimental precision of VBS measurements requires adequate theoretical predictions. NLO QCD corrections to VBS for leptonic final states and the corresponding irreducible background processes have existed for many years including their matching to parton showers. For a recent review, see Ref. [5]. They are available in VBFNLO [87] as well as the general-purpose generators MadGraph5_aMC@NLO [88, 89], Sherpa [90] and POWHEG [91, 92, 93].

EW corrections to VBS processes, on the other hand, have only been calculated recently. The EW corrections to same-sign WW scattering have been published in Ref. [35], those for WZ scattering in Ref. [85], and the ones for VBS into ZZ bosons in Ref. [86]. The calculation of EW corrections for the scattering of opposite-sign W bosons is ongoing work. For same-sign WW scattering an event generator has been made available based on Powheg [91, 92] and Recola [94, 95] with Collier [96] for the processes $pp \rightarrow \ell^\pm \nu_\ell \ell'^\pm \nu'_\ell jj$, with $\ell, \ell' = e, \mu$ including EW corrections and matched to a QED parton shower and interfaced to a QCD parton shower [37].

The relative EW corrections to fiducial cross sections of VBS processes in the SM turn out to be around -16%, independent of the specific process and the details of event selection. While the EW corrections δ_{EW} for the three processes in Table 3.1 are very close to each other, this is accidental and the expected spread is at the level of a few per cent. The large universal EW corrections for VBS processes can be explained by a Sudakov approximation applied to the $VV \rightarrow VV$ subprocesses.

Following Refs. [97, 98], the leading logarithmic corrections to the scattering of transverse vector bosons, which is the

dominant contribution, can be cast into a simple universal correction factor

$$\delta_{LL} = \frac{\alpha}{4\pi} \left\{ -4C_W^{EW} \log^2\left(\frac{Q^2}{M_W^2}\right) + 2b_W^{EW} \log\left(\frac{Q^2}{M_W^2}\right) \right\}. \quad (3.1)$$

It includes all logarithmically enhanced EW corrections apart from the angular-dependent sub-leading soft-collinear logarithms and applies to all VBS processes that are not mass suppressed, owing to the fact that these scattering processes result from the same SU(2)$_w$ coupling. The constants are given by $C_W^{EW} = 2/s_w^2$ and $b_W^{EW} = 19/(6s_w^2)$, where s_w represents the sine of the weak mixing angle. Further, Q is a representative scale of the $VV \rightarrow VV$ scattering process, which is conveniently chosen as the four-lepton invariant mass $M_{4\ell}$. Using $Q = M_{4\ell}$ event-by-event results in the numbers for $\delta_{EW}^{log,diff}$ shown in the 6th column of Table 3.1, which agree within 2% with the full NLO results. Applying eq. (3.1) directly to the fiducial cross section with the average values for $M_{4\ell}$ obtained from a leading order (LO) calculation (see 7th column of Table 3.1) yields the numbers for $\delta_{EW}^{log,int}$ shown in the 5th column of Table 3.1.

Since the leading logarithmic corrections are universal and only depend on the gauge structure of the theory and the external particles, one expects similar corrections in extensions of the SM that do not modify the gauge sector. For the scattering of longitudinal gauge bosons, smaller corrections are expected since the related coupling factors are smaller. EW corrections to distributions reach -30% to -40% in high energy tails in the TeV range.

3.2 Complete NLO corrections to VBS

Besides VBS diagrams, other diagrams contribute to the same physical final states in scattering processes of the form $pp \rightarrow l_1 \bar{l}_2 l_3 \bar{l}_4 jj$. At leading order the cross sections for processes of the type $pp \rightarrow l_1 \bar{l}_2 l_3 \bar{l}_4 jj$ receive pure EW contributions of orders α^6, QCD-induced contributions of order $\alpha^4\alpha_s^2$, and interference contributions of order $\alpha^5\alpha_s$. At NLO there are corresponding contributions of orders α^7, $\alpha^6\alpha_s$, $\alpha^5\alpha_s^2$, and $\alpha^4\alpha_s^3$. While the $O(\alpha^7)$ contributions can be viewed as EW corrections to the LO EW process and the $O(\alpha^4\alpha_s^3)$ contributions as QCD corrections to the LO QCD-induced process, the other contributions cannot be classified simply as EW or QCD corrections in general. For instance: the contribution at $O(\alpha^6\alpha_s)$ contains QCD corrections to the LO EW process but also EW corrections to the LO interference. A unique assignment can be made within the so-called VBS approximation, where interference between different kinematic channels are neglected.

For same-sign WW scattering, the full NLO corrections of all four orders have been calculated [99]. Since this process is dominated by the EW diagrams at LO, the magnitude of the corrections at orders $O(\alpha^3\alpha_s^2)$ and $O(\alpha^4\alpha_s^3)$ is small, i.e. below a per cent for the fiducial cross section and at the level of one per cent for distributions. This will be different for other VBS processes where the QCD-induced contribution is larger than the EW contribution. The calculation of these types of corrections is ongoing.

8

Process	$\sigma_{\text{LO}}^{O(\alpha^6)}$ [fb]	$\sigma_{\text{NLO,EW}}^{O(\alpha^7)}$ [fb]	δ_{EW} [%]	$\delta_{\text{EW}}^{\text{log,int}}$ [%]	$\delta_{\text{EW}}^{\text{log,diff}}$ [%]	$\langle M_{4\ell} \rangle$ [GeV]	Ref.
$pp \to \mu^+ \nu_\mu e^+ \nu_e jj\ (W^+W^+)$	1.5348(2)	1.2895(6)	−16.0	−16.1	−15.0	390	[35]
$pp \to \mu^+ \mu^- e^+ \nu_e jj\ (ZW^+)$	0.25511(1)	0.2142(2)	−16.0	−17.5	−16.4	413	[85]
$pp \to \mu^+ \mu^- e^+ e^- jj\ (ZZ)$	0.097681(2)	0.08214(5)	−15.9	−15.8	−14.8	385	[86]

Table 3.1: EW corrections to fiducial cross sections of different VBS processes at $\sqrt{s}$ = 13 TeV.

3.3 Quality of the VBS approximation

In the past, many calculations for VBS have used the "VBS approximation." In this approximation only the squares of t- and u-channel contributions are taken into account, while interference between these channels as well as s-channel contributions are omitted ($|t| + |u|$ approximation). In some calculations the s-channel contributions are included ($|s| + |t| + |u|$ approximation), while interference is still neglected. The quality of these approximations has been investigated in Ref. [50] for same-sign WW scattering by comparing the results of different calculations using different approximations. While this study confirmed that the accuracy of the VBS approximation is better than about 1% at LO, it revealed larger differences at NLO QCD. In a more inclusive region, $e.g.$, $M_{jj} > 200$ GeV, $\Delta y_{jj} > 2$, the differences at NLO in QCD amount to −6% for the $|t| + |u|$ approximation and +2.6% for the $|s| + |t| + |u|$ approximation, and grow up to ∓20% (same direction) for some distributions. In a typical fiducial region for VBS, $i.e.$, where $M_{jj} > 500$ GeV, $\Delta y_{jj} > 2.5$, the $|t| + |u|$ and $|s| + |t| + |u|$ approximations lead to cross sections that differ from the exact NLO calculation by about 2% and 1%, respectively. These differences are comparable to residual scale uncertainty at NLO. For some differential distributions, these different approximations can lead to differences as large as ±10%. Details are discussed in Ref. [50].

These larger differences at NLO can be attributed to contributions of triple vector-boson production with an additional gluon. While VVV contributions are effectively suppressed by the VBS cuts on the two tagging jets, the additional gluon jet reduces the efficiency of these cuts. This has been confirmed in [86], where 24% NLO QCD corrections have been found for VBS into ZZ for a loose VBS cut of $M_{jj} > 100$ GeV. Similar conclusions have also been reported in Ref. [100] for same-sign WW scattering and the impact of Drell-Yan-like topologies. Thus, one should either take into account triple vector-boson production in the theoretical prediction or use tight VBS cuts.

3.4 Polarized VBS

A primary goal in VBS experiments is to measure the scattering of longitudinal vector bosons, which is very sensitive to the EW symmetry breaking and to physics beyond the SM owing to strong unitarity cancellations within the SM. However, the definition of polarized cross sections for massive vector bosons is not unique, since the vector bosons are unstable, and moreover any definition of their polarization is linked to a certain frame.

In the literature, different definitions of vector-boson polarization have been discussed. A short overview can be found, for instance, in Ref. [53]. A polarization definition based on projections on the LO decay-angle distributions has been put forward in Ref. [51, 52]. This method is tailored to inclusive LO distributions due to the resonant vector-boson diagrams. It is only applicable to one polarized vector boson and fails for tight cuts, sizable background, or large NLO corrections. The calculation of polarized cross sections has been automated for LO calculations in the MADGRAPH5_AMC@NLO Monte Carlo event generator [47], employing decay chains in the narrow-width approximation and including spin correlations via the MADSPIN package [101]. A definition of polarized cross sections based on the pole approximation has been proposed and applied to VBS at LO in [102, 103, 48].

Based on Refs. [102, 103], a proposal was made in Ref. [53] that splits the vector boson productions process from the irreducible background and defines polarized matrix elements for vector boson production. It is applicable to arbitrary processes, multiple resonances, and NLO calculations. It allows for defining polarizations in arbitrary frames and for separating the irreducible background and interference between polarized matrix elements. The method has already been applied to vector boson pair production at NLO QCD [53, 54] and will be used to calculate NLO corrections to polarized VBS in the future.

3.5 Summary

In this short section, we summarized the status of precision predictions for VBS in the SM with a focus on recent computational developments. In this dynamic field more progress can be expected in the near future. This concerns in particular polarized VBS, semileptonic final states, matching to EW parton showers, and precision predictions for VBS in extended models.

Part III

VBS prospects for the HL-LHC

4 Experimental projections for the HL-LHC

The HL-LHC will collide protons at $\sqrt{s}$ =14 TeV, with a projected peak instantaneous luminosity of about $5 \cdot 10^{34}$ cm^{-2}s^{-1}, and which will be increased to about $7.5 \cdot 10^{34}$ cm^{-2}s^{-1} [105].
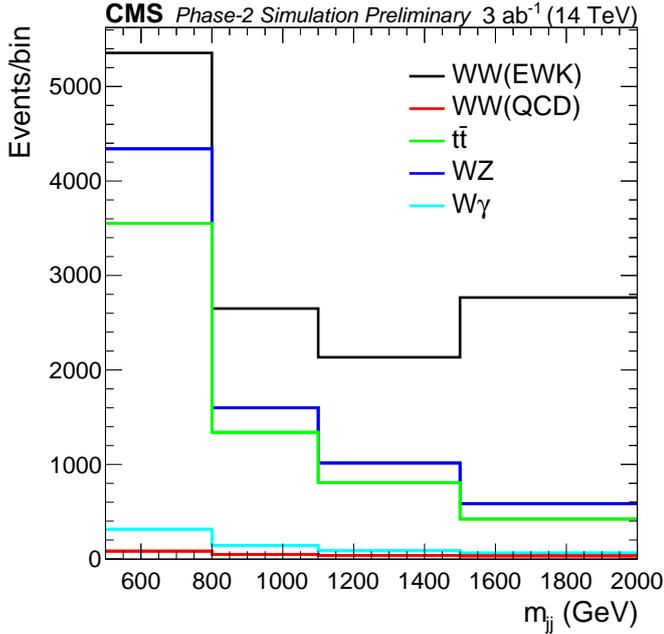
Figure 4.1: Invariant mass of the two leading jets of the $W^\pm W^\pm jj$ process at $\sqrt{s}$=14 TeV and normalized to an integrated luminosity of 3000 fb^{-1}, from Ref. [104].

Figure 4.2: Total cross section uncertainty of the $W^\pm W^\pm jj$ process as a function of the integrated luminosity, considering systematic uncertainties as in the YR18 scenario [106]. From Ref. [104].

These rates are about three-to-four times higher than the peak luminosity of Run 2, and will accumulate to a total integrated luminosity of about 3 ab^{-1}. The ATLAS and CMS detectors will be upgraded to cope with the new HL-LHC operating conditions. These upgrades include extended geometric coverage and finer detector resolution, and will improve sensitivity to VBS processes. See Section 9 for more details on the detector upgrades.

VBS analyses, which at the moment have uncertainties that are statistically dominated, will benefit from the larger amount of data collected and the higher center-of-mass energy. Moreover, detector upgrades, such as the extension of tracker coverage and the addition of timing detectors, will help in the rejection of additional leptons and of pileup jets, reducing background contamination. Finally, an increase of statistics will allow better calibration, hence a reduction of experimental uncertainties is also expected. In the following we summarize the anticipated HL-LHC performance with the CMS (see Section 4.1) and ATLAS (see Section 4.2) detectors.

4.1 Projections with the CMS detector

Here, we summarize the HL-LHC projections at the CMS experiment for three VBS processes, $W^\pm W^\pm jj$ (Section 4.1.1), $WZjj$ (Section 4.1.2), and $ZZjj$ (Section 4.1.3), and compare them with the latest published results at 13 TeV with the full Run 2 data sets ($\mathcal{L} \approx$137 fb^{-1}). The aim is to understand where these analyses stand now and what would be their perspective for the future.

4.1.1 $W^\pm W^\pm jj$

The first VBS process observed with the CMS experiment was the production of two same-sign W bosons $W^\pm W^\pm jj$ [11] in the fully leptonic final state (for further details see Section 1.1). The prospects of measuring VBS production of $W^\pm W^\pm jj$ at the HL-LHC ($\sqrt{s}$ = 14 TeV) has been studied by the CMS Collaboration [104]. Results are obtained in the fully leptonic final state, using full simulation of the upgraded Phase-2 CMS detector and accounting for an average number of 200 proton-proton interactions per bunch crossing.

In the HL-LHC scenario, the $W^\pm W^\pm jj$ would strongly benefit from the increased integrated luminosity, due to its very low cross section $O(1$ fb). Moreover, the upgrade of the CMS detector, such as the extension of the tracker coverage (improvement of lepton identification) and the new forward High Granularity Calorimeter HGCAL (improving identification of jets), will help with rejecting backgrounds more efficiently, allowing a better discrimination of the signal. The main uncertainties affecting the analysis are treated following the Yellow Report 18 (YR18) [106] recipe: theoretical uncertainties are halved with respect to the current values, while experimental uncertainties are scaled by $1/\sqrt{L}$ (where L is the integrated luminosity), until they reach the limit of accuracy estimated with the Phase-2 detector.

The final state contains events with two leptons (e/μ) with the same charge, significant missing transverse energy (from W boson decays), and two high-energy jets with a high invariant mass and large separation in pseudorapidity. More details on the analysis are documented in Ref. [104].

The invariant mass distribution of the two leading jets (Fig. 4.1)
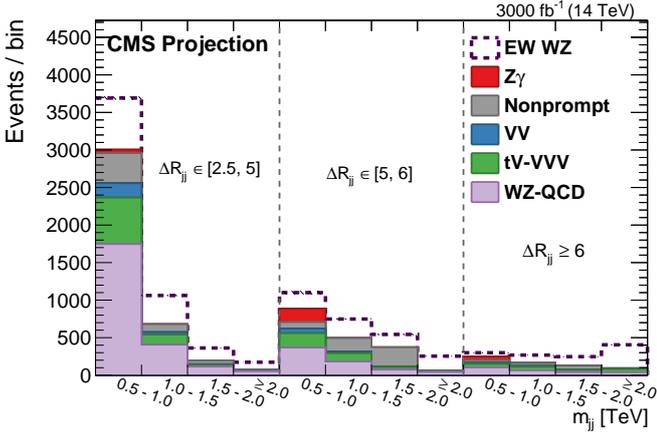
Figure 4.3: Distribution of m_{jj} in bins of ΔR_{jj}, *i.e.* the distance (in the η, ϕ space) between jets. From Ref. [107].

Figure 4.4: Total cross section uncertainty as a function of integrated luminosity for the WZjj production process. From Ref. [107].

is fitted using a binned maximum likelihood approach in which all the three lepton flavor categories (ee, $\mu\mu$, $e\mu$) are treated as independent channels. All the systematic uncertainties are inserted as log-normal distributions in the form of nuisances, and their correlations are taken into account. Despite the requirement of same-sign leptons, top quark pair production is the dominant background of this analysis. The wrong identification of jets containing a b quark is one of the most relevant systematic uncertainties. For the same reason, the wrong identification of jets as leptons, which enhances the so-called "fake" background, also plays an important role.

Figure 4.2 shows the total cross section uncertainty decreasing as a function of the integrated luminosity, and reaching a value of 3% for 3000 fb^{-1}. A recent CMS result in this channel at $\sqrt{s}$=13 TeV with the full Run 2 data set (137 fb^{-1}) reports an uncertainty of 11% on the total cross section [32]. When these results are re-scaled according to the YR18 prescriptions, a good agreement is found with the earlier predictions [104]. This confirms the expectations of reducing the total uncertainty in this channel by almost a factor of 4, namely down to 3% for 3000 fb^{-1}.

Polarization studies' projections are also performed in Ref. [104]. The longitudinal component of same-sign WW scattering is only 6-7% of the total cross section. Thus, even at the HL-LHC isolating the longitudinal component in this analysis will be strongly limited by statistics. The expected significance for an integrated luminosity of 3000 fb^{-1} is expected to reach 2.7 standard deviations, and exceed 3σ when combining CMS and AT-LAS results.

4.1.2 $WZjj$

The first evidence of EW $WZjj$ production in the fully leptonic channel with three leptons at 13 TeV was published by the CMS Collaboration with 2016 data (36 fb^{-1}) in Ref. [14] and by the ATLAS Collaboration in Ref. [13]. The observation with a statistical significance of 6.8 standard deviations was extracted by a simultaneous fit with the $W^\pm W^\pm jj$ channel using the full Run 2 data set [32]. Extrapolations of this analysis to the
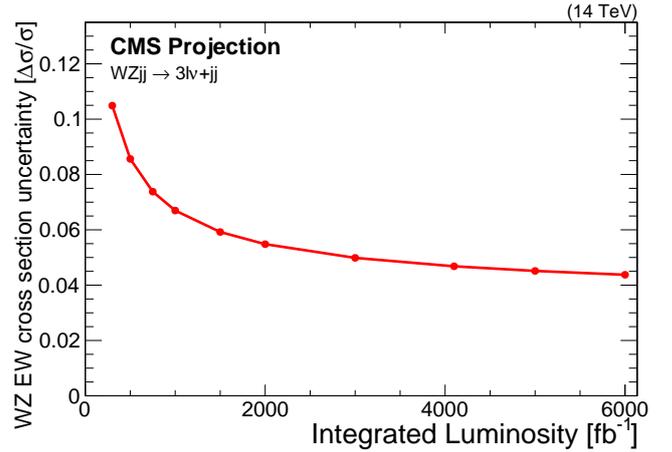
HL-LHC have shown the potential gain thanks to the larger data samples, since the analysis is still statistically limited [107].

Going from 13 TeV to 14 TeV, VBS cross sections increase by 8-20%. In particular, the EW component increases by 16%, while the QCD component (the irreducible background) increases only by 8%. Moreover, the pseudorapidity coverage extension of the tracker detector would lead to an increase of the event yields, depending on the precise final state, by about 5-8%. Projections have been obtained using simulated signal and background samples at 13 TeV with a full reconstruction of the Phase-1 detector used in Run 2, scaled by the corrections due to cross section, acceptance, and luminosity increase. The analysis selects events with three charged leptons, missing transverse energy, and two high-energy and well-separated jets. As to charged leptons, one pair of same-flavor and opposite-sign leptons is expected from the Z boson decay, while the third lepton is from the W boson decay. Events are split into four categories with respect to the flavors of final state leptons: eee, $ee\mu$, $\mu\mu e$, $\mu\mu\mu$. Since the fraction of the EW component in inclusive $WZjj$ increases with the invariant mass (m_{jj}) and the angular separation ΔR (η, ϕ) of the jets, the binned maximum likelihood fit is performed on the 2D distributions of these two variables (Fig. 4.3), simultaneously for the four independent lepton flavor categories. All the systematic uncertainties are taken into account as nuisances in the fit, as well as their correlations. Input values for most of these uncertainties, both experimental and theoretical, are expected to be reduced to 1% at the HL-LHC. Among the theoretical uncertainties, renormalization and factorization scale choices, *i.e.*, QCD scale choices, play the biggest role. For the experimental uncertainties, the jet energy scale and resolution are the largest. More details on the analysis strategy, the fit and nuisances treatment are discussed in Ref. [107]. Finally, results are summarized in Fig. 4.4, which shows the total cross section uncertainty as a function of the integrated luminosity. At 3000 fb^{-1}, the total uncertainty would approach 5%, about a fifth of the current Run 2 precision of $\approx$23% [32].
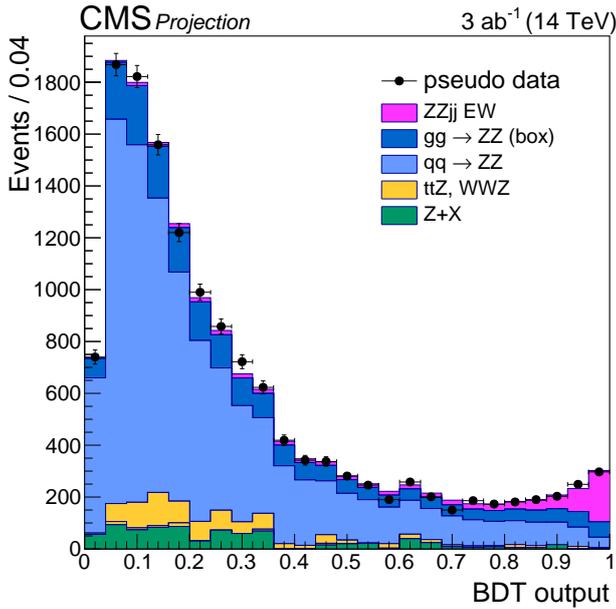
Figure 4.5: BDT discriminator output for a luminosity of 3000 fb^{-1} at $\sqrt{s}$ = 14 TeV, for signal and for the backgrounds (from Ref. [108]). The purple filled histogram represents the EW signal (ZZjj inclusive process), the other histograms represent the different backgrounds.

4.1.3 ZZjj

The VBS production of a pair of Z bosons in association with two jets (ZZjj) was studied in the fully leptonic final state by the CMS Collaboration in Ref. [12] with the 2016 data set, and a claim for evidence has been recently published by the CMS Collaboration with the full Run 2 data set [27]. Related to this, the ATLAS Collaboration has reported an observation of the same channel with the full Run 2 data set in Ref. [28]. This channel has a small cross section but results in a clean final state with a small contamination of reducible background. The fully leptonic final state allows also the complete reconstruction of the particles' kinematics, making ZZjj a suitable candidate for polarization studies.

The prospects for measuring both inclusive and longitudinal polarized cross sections of the ZZjj channel at the HL-LHC with the CMS experiment are described in Ref. [108]. The study starts from the analysis of the 2016 data set (36 fb^{-1}) [12] and focuses on a final state with two lepton pairs (same-flavor and opposite charge sign from the Z boson decay candidate) and two jets. The Run 2 results are extrapolated to HL-LHC by taking into account the larger integrated luminosity, the increase of center-of-mass energy to 14 TeV, and the extension of the tracker acceptance up to η=3. The signal's cross section increase is estimated to be about 15%, while it is of the order of 17% (13%) for the QCD qqZZ (ggZZ) process. Moreover, the signal yield is expected to increase by up to 20% thanks to the larger acceptance. Unfortunately the QCD-induced production of qqZZ is expected to have an increase of 10% higher than the signal, while the ggZZ background is less relevant in
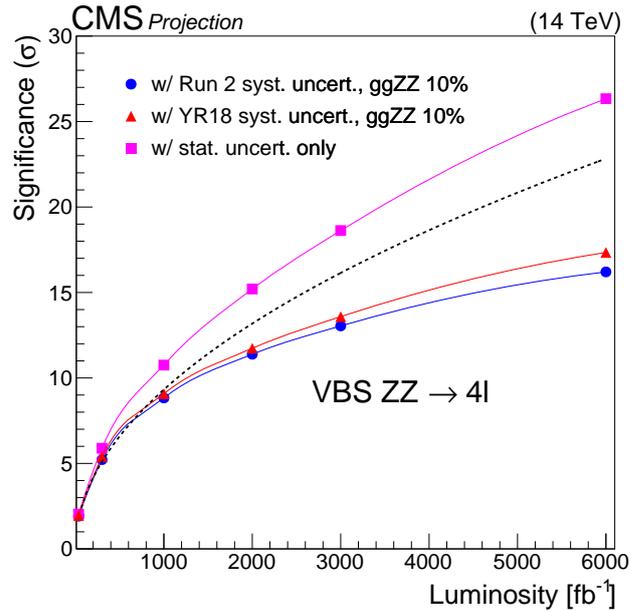
Figure 4.6: Significance as a function of the integrated luminosity in the Run 2 (blue line, circles) and YR18 (red line, triangles) scenarios. The QCD ggZZ background yield uncertainty is set to 10 %. Results considering only the statistical uncertainties are also included (magenta line and squares), as well as those obtained by scaling the statistical uncertainties of the 2016 results by the luminosity ratio (dashed black line). From Ref. [108].

the projected results. A BDT is used to disentangle the EW and QCD components of ZZjj. The BDT distribution in Fig. 4.5 is then fitted with a maximum likelihood approach, in which systematic uncertainties are considered as nuisance parameters and profiled.

Regarding systematic uncertainties, two different scenarios have been considered. In the first scenario ("Run 2"), the systematic uncertainties remain the same as the ones quoted in Ref. [12]. In the second scenario ("YR18") [106], the theoretical uncertainties are halved and the experimental ones are scaled down by a factor $1/\sqrt{L}$. In both scenarios, the theory uncertainty on the loop-induced production of ZZjj has the largest impact; its input value is fixed at 10%. Results that include the two scenarios are shown in Fig. 4.6. A new prediction, obtained by scaling the YR18 projection with the most recent results (a 4σ significance) with the full Run 2 data set in the same final state [27], shows a better performance with respect to the old one. The better performance is due to the fact that, instead of a BDT, a matrix element discriminant is used in the Run 2 analysis [27] to separate the EW and QCD components of the ZZjj process. New projections show that the 5σ threshold can be exceeded in the early stage of HL-LHC.

Analogously, the VBS $Z_L Z_L$ signal component is separated from the VBS and QCD backgrounds by means of a multivariate discriminant. The expected significance for selecting the VBS longitudinal polarized event fraction is 1.4σ with 3000 fb^{-1}
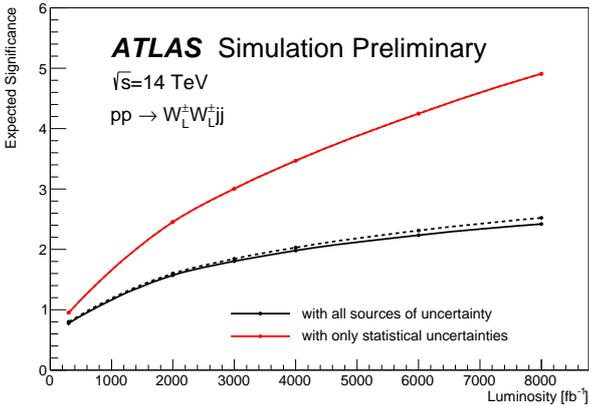
Figure 4.7: Projection of the expected significance of the $W_L^\pm W_L^\pm$ scattering process as function of integrated luminosity, considering all sources of uncertainty (black) or only the statistical uncertainty (red). The dashed line show the expectation for the optimistic scenario [109].

at the CMS experiment. Comparable results are anticipated for the ATLAS experiment.

4.2 Projections with the ATLAS detector

We now summarize the HL-LHC projections at the ATLAS experiment for the $W^\pm W^\pm$ (Section 4.2.1) and WZ scattering channel (Section 4.2.2), as well as the sensitivity to anomalous quartic gauge couplings (Section 4.2.3).

4.2.1 $W^\pm W^\pm jj$

The most recent HL-LHC projections for $W^\pm W^\pm$ scattering with the ATLAS detector [111] focus on the comparison of detector coverage and an investigation into the extraction of the longitudinal component. The selection is based on the 8 TeV ATLAS measurement reported in Ref. [19], while the study of Ref. [109] uses particle-level simulated samples.

For both studies, the signal as well as the same-sign WW and WZ backgrounds are simulated. Particle-level objects are smeared to achieve a realistic estimate of the event yield, accounting for the detector resolution. Other non-dominant backgrounds are estimated from the 8 TeV measurement. A systematic uncertainty on the background estimate is assumed to be 15%. Different detector coverage configurations are studied by varying the range over which particle reconstruction and jet-vertex association are possible. The default scenario does not foresee forward tracking for $|\eta| > 2.7$. Extending the coverage of jet-vertex association to $|\eta| < 3.8$ allows one to lower the p_T threshold for jets; this has the largest impact and increases the signal acceptance by up to 10%. Extending the muon acceptance to $|\eta^\mu| = 3.8$ increases the overall signal acceptance by $\sim 5\%$, while extending the range for electron reconstruction to $|\eta^e| = 3.8$ has only a minor impact. Overall, uncertainties on the signal strength are projected to be in the range of 4.0-4.5%.

Reference [112] presents the extraction of longitudinally polarized $W_L^\pm W_L^\pm$ scattering. The event selection is slightly op-

timized for this purpose by raising the momentum thresholds. This also serves to reject backgrounds from QCD production of WW. Experimental systematic uncertainties for the study are taken from the 13 TeV observation of same-sign WW scattering events [15]. Alternatively, an optimistic scenario reducing the uncertainties on data-driven backgrounds by 33-50% is also considered. The total uncertainty on the same-sign WW scattering cross section is projected to be 6%. A likelihood fit is used to extract longitudinal scattering signal from the distribution of the difference in the azimuth angle between the two jets in two regions of dijet invariant mass: (i) $520 < m_{jj} < 1100$ GeV and (ii) $m_{jj} > 1100$ GeV. The significance is expected to be $1.8\,\sigma$ as shown in Fig. 4.7. The expected precision of the measurement of the longitudinal $W_L^\pm W_L^\pm$ scattering cross section is 47%. Considerable improvements are achievable using multivariate techniques. However, these have not yet been explored.

4.2.2 $WZjj$

The HL-LHC prospects for observing WZ scattering with leptonic decays of the W and Z bosons are investigated in Ref. [110]. All major detector effects are included using parametrization. The selection is based on the selection developed for the observation of WZ scattering with the ATLAS detector at $\sqrt{s} = 13$ TeV [13].

The ATLAS detector coverages studied are described in detail in Ref. [110]. Most notable are the Run 2 benchmark scenario (accepting only central leptons, $|\eta| < 2.5$, and requiring forward jets, $2.5 < |\eta| < 4.5$ with $p_T > 75$ GeV) and a nominal ATLAS Phase-2 scenario with extended acceptances for leptons and jets. A variation of this selection includes using the high granularity timing detector (HGTD) [113], which improves the electron and jet selection efficiencies in the forward region ($2.4 < |\eta| < 3.8$). For all event selections, the signal region is defined using the $m_{jj} > 500$ GeV selection criterion. Alternatively, an optimized selection based on a BDT classifier trained using 25 input variables sensitive to the VBS topology is used. Figure 4.8 compares these selections using the number of selected signal events and the expected signal significance estimated as $S/\sqrt{S + B}$. Extending the jet acceptance is only possible if a jet-vertex association can be applied or if the jet p_T threshold is increased, which lowers the number of signal events. Otherwise a prohibitive amount of background is selected. The maximal gain in signal events compared to the Run 2 setup is 60 % using either the BDT or extending the jet acceptance up to $|\eta| = 4.5$ without increasing momentum thresholds. An alternative BDT-based selection achieves the largest signal significance, however with a 15 % loss of signal events with respect to the Run 2 setup. The investigation projects that the uncertainties will be dominated by systematics related to jets and the WZ background. It is suggested that these could be better constrained using additional data-driven control regions.

The fraction (F_λ) of the individual vector boson polarization state λ can be extracted using template fits of F_L and $(F_- - F_+)$ to the $\cos\theta^*$ distribution. The angle θ^* is defined as the decay angle of the lepton (or anti-lepton for W^+) with respect to the boson's direction in the WZ rest-frame. Figure 4.9 shows the
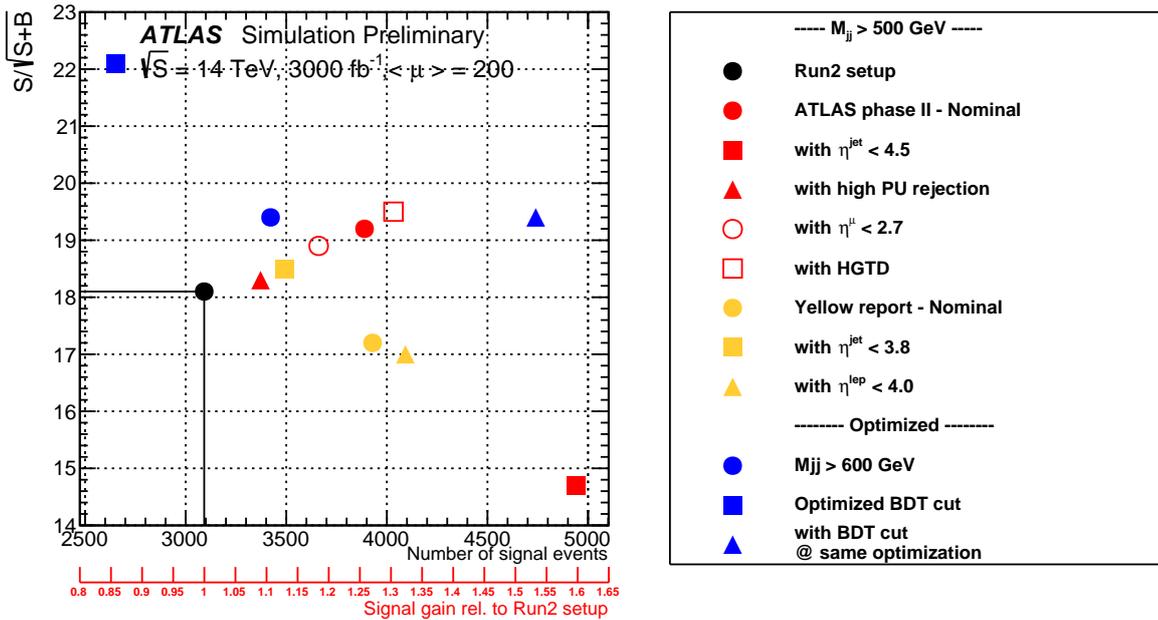
Figure 4.8: Overview over the anticipated sensitivity performance for the *WZ* process for the HL-LHC phase achieved using the event selections based on the detector performance parameters described in the text. Signal sensitivity as a function of the number of events and relative signal gain with respect to the Run 2 settings. Figure from Ref. [110].

normalized distributions of the different *W* polarization states as a function of $\cos\theta^*$ at the reconstruction level. Four different event distributions are fitted depending on the boson that is probed and on the charge of the *W* boson present in the event. For the systematic uncertainty associated to the total background normalization, three possible scenarios are assumed: 20%, 5% and 2.5%. Different selections are tested, namely the nominal selection requiring $m_{jj} > 500, 600, 1100$ GeV, as well as two different BDT cuts. In addition, the effect of quark-gluon tagging on the leading and sub-leading jets to further reduce the backgrounds is studied. Finally, the luminosity is doubled to emulate the combination of the ATLAS and CMS data samples. The expected significance for the polarization signal is 0.5-3.5 σ depending on the selection, with the most sensitive distribution being that of the *Z* boson in W^+Z events.

The signal significance for the $W_L Z_L$ polarization state is estimated in a simultaneous fit of $\cos\theta^*$ and the scalar sum of the leptons' transverse momenta, without considering the background processes. The estimated significance is less than one standard deviation. The use of the full double differential distribution of $\cos\theta^*(W)$ versus $\cos\theta^*(Z)$ or other more sophisticated methods could however improve these results.

4.2.3 Anomalous Quartic Gauge Couplings

Projections for limits on anomalous quartic gauge couplings and dimension-8 EFT operators [45] have been reported in Ref. [114] which uses one-dimensional distributions for both *WZ* and *WW* scattering processes in the limit setting. It is instructive to compare the projected limits with those extracted using the LHC Run 2 data to answer the obvious question as to how realistic
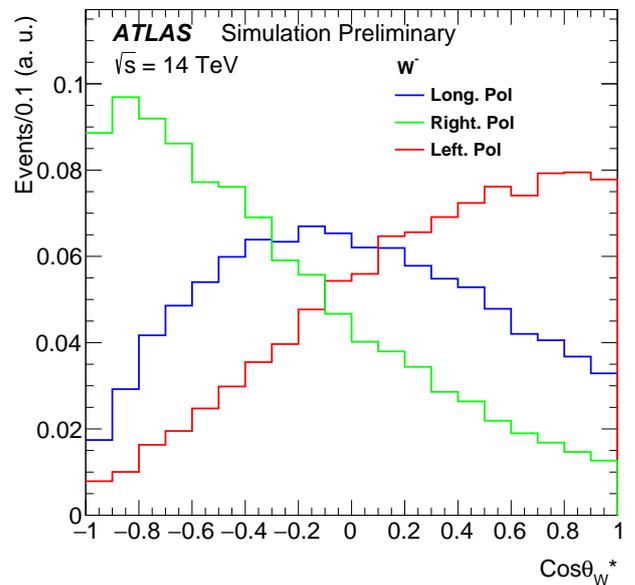
Figure 4.9: Normalized W^- polarization state templates at the reconstruction level and after the final event selection, including requiring $m_{jj} > 600$ GeV. Figure from Ref. [110].

the HL-LHC projections in general are. The projected limits for an integrated luminosity of 300 fb^{-1} in 14 TeV collision data are about a factor 2-3 worse than what was achieved with Run 2 data [32]. This indicates that the projections are rather conservative.

VBS production of EW boson pairs are rare processes that allow precision measurements of the EW sector. VBS processes are typically statistically limited at Run 2 and will benefit from the HL-LHC operation conditions (14 TeV, 3000 fb^{-1}), resulting in better constraints of known processes ($W^{\pm}W^{\pm}jj, WZjj$) and measurements of those that have not been observed yet ($W^+W^-jj, ZZjj$). Moreover, the HL-LHC will allow the ATLAS and CMS experiments study of final states other than the fully leptonic ones, such as semi-leptonic or even fully hadronic final states. These modes guarantee higher statistics. In the HL-LHC scenario, the limiting factor to precision measurements is expected to be the systematic uncertainties: a work toward the reduction of systematic, theoretical and experimental, would be of primary interest for the LHC community.

5 SMEFT in VBS at the HL-LHC

The Standard Model Effective Field Theory (SMEFT) has become a standard tool used in indirect and semi-model-independent searches for BSM physics at the LHC. A lot of effort, both on the theory and experimental sides, goes into finding the optimal methodological guidelines for applying SMEFT in VBS processes in particular. One vital issue is how to correctly set limits on Wilson coefficients without violating the validity of EFT. Another lasting question is whether to focus on dimension-6 or dimension-8 SMEFT operators in data analysis. Some of the most recent progress concerning these two important issues are discussed. This progress involves new developments in setting limits on SMEFT dimension-8 operators based on the LHC Run 2 data collected by the ATLAS and CMS detectors, and new studies of potential effects of SMEFT dimension-6 operators based on current experimental bounds from global fits to data from other processes. As an example of this progress, we focus in this section on the use of the so-called "clipping" technique by CMS during Run 2 and the prospects for probing dimension-6 operators with same-sign WW scattering at the HL-LHC. (For examples of studying SMEFT operators at future colliders, see Section 13.)

5.1 Full clipping technique in the analysis of Run 2 data

Recently, the CMS Collaboration published an analysis of the same-sign WW and WZ scattering processes, based on data collected during the LHC Run 2, where limits on dimension-8 operators were derived for the first time using a partial "clipping" technique [32]. For every value of an individual Wilson coefficient, simulated BSM distributions were "clipped" at the unitarity limit. Beyond this limit, the high mass tails were replaced with SM tails to compute the EFT prediction. The impact of considering only the unitarity condition on the results was shown to be significant, with the actual limits being relaxed typically by a factor of $4-5$ compared to limits calculated without unitarity considerations.

In reality, the scale of new physics can be lower than the unitarity limit. Physically interpretable limits on individual Wilson
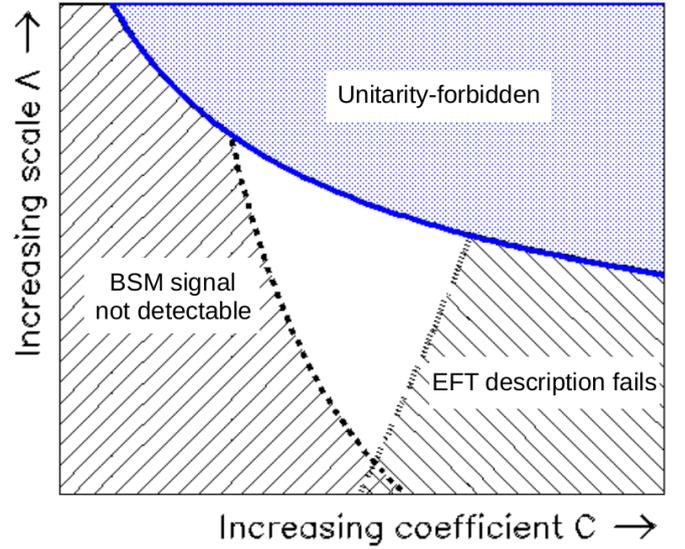
Figure 5.1: For a Wilson coefficient C and EFT cutoff scale Λ, a sketch of the regions in $\Lambda - C$ space that are forbidden by unitarity (large Λ and large C), are inconsistent with the assumptions of EFTs (small Λ and large C), and are inaccessible to experiments (small C and/or large Λ). Adapted from Ref. [115].

coefficients C exist only as a function of the EFT Λ cutoff parameter, the latter ranging between the lowest WW mass accessible in the experiment and the appropriate unitarity bound. Limits then take the form of 2-dimensional exclusion curves, with one axis being the value of C and the other axis being the value of Λ. A sketch of such an exclusion curve is shown in Fig. 5.1. Also shown in this cartoon are the regions in $\Lambda - C$ space that are forbidden by unitarity (large Λ and large C), are inconsistent with the assumptions of EFTs (small Λ and large C), and are inaccessible to experiments (small C and/or large Λ).

Observed (and expected) experimental limits can be compared to theoretical limits that follow solely from the unitarity condition. Naturally, experimental limits are meaningful only if they are stronger than theoretical limits. An encouraging observation is that theoretical exclusion curves, based on the unitarity condition, give a flatter dependence of $C(\Lambda)$ than experimental exclusion curves based on signal significance. From this it can be anticipated that the two curves will cross at some value of Λ and hence experimental limits for most dimension-8 operators can indeed be meaningful as long as Λ is not too high. Given that unitarity limits for the values of Wilson coefficients obtained in Ref. [32] are typically around 1.5 TeV, one can expect this critical value of Λ be roughly around 2 TeV (this takes into account that limits on C with a constant Λ are more permissive than with a running $\Lambda(f)$). In the HL-LHC perspective, this range will still widen.

The analysis also included a study of the most sensitive kinematic variables to each individual operator, assuming the signal process $pp \rightarrow W^{\pm}W^{\pm}jj \rightarrow \ell_i^{\pm}\ell_j^{\pm}jj\nu\bar{\nu}$. As observed in

several earlier studies, the cluster mass variable

$$M_{o1} =$$
$$\sqrt{\left(|\vec{p}_T^{\,\ell_1}| + |\vec{p}_T^{\,\ell_2}| + |\vec{p}_T^{\,\text{miss}}|\right)^2 - \left(\vec{p}_T^{\,\ell_1} + \vec{p}_T^{\,\ell_2} + \vec{p}_T^{\,\text{miss}}\right)^2} \quad (5.1)$$

is the most sensitive variable for most dimension-8 operators. Here, $\vec{p}_T^{\,\ell_k}$ for $k = 1, 2$ are the transverse momentum vectors of the two same-sign charged leptons and $\vec{p}_T^{\,\text{miss}}$ is the transverse momentum imbalance of the event. However, for S operators and sufficiently low Λ it is outperformed by the kinematic ratio

$$R_{pT} = \frac{|\vec{p}_T^{\,\ell_1}||\vec{p}_T^{\,\ell_2}|}{|\vec{p}_T^{\,j_1}||\vec{p}_T^{\,j_2}|}, \quad (5.2)$$

where $\vec{p}_T^{\,j_k}$ are the transverse momentum vectors of the two VBS-tagged jets. For further details, see Ref. [115].

5.2 Dimension-6 operators in the same-sign WW process

The potential impact of SMEFT dimension-6 operators within their current experimental bounds on the same-sign WW VBS scattering process at the LHC was recently studied in Refs. [116, 117, 118, 119, 120]. Outside of SMEFT, recent studies include Refs. [121, 122, 123]. In particular, in the generator-level study of Ref. [118], potential BSM signals from all the individual operators at dimension 6 in the Warsaw basis [124] was checked by studying their impact on the distributions of different kinematic variables. For each operator, the variable with the highest sensitivity was chosen. Signals were normalized to the nominal integrated luminosity for the HL-LHC. The study explicitly included four VBS operators that affect the reaction $W^\pm W^\pm \to W^\pm W^\pm$: O_W, $O_{\phi\Box}$, $O_{\phi D}$ and $O_{\phi W}$, neglecting $O_{\phi WB}$ which vanishes in the cross section formula to leading order in s, and neglecting CP violating operators. In addition, 26 background operators, i.e., those that do not affect the WW scattering reaction -but may affect the full process at the pp level- were explicitly considered.

Current experimental limits on dimension-6 operators other than 4-fermion operators were taken from recent global fits to existing data [125, 126] that include all the most recent LHC Run 2 data. For 4-fermion operators, older bounds [127] were used and found sufficient to claim them negligible. The following background operators were also found to be negligible within the existing limits:

$$O_{u\phi}, O_{d\phi}, O_{uG}, O_{\phi q}^{(1)}, O_{\phi u}, O_{\phi d}, O_{uu},$$
$$O_{dd}, O_{ud}^{(1)}, O_{ud}^{(8)}, O_{qq}^{(1)}, O_{qu}^{(1)}, O_{qu}^{(8)}, O_{qd}^{(1)}, O_{qd}^{(8)}. \quad (5.3)$$

For O_{uG}, limits are deduced assuming minimal flavor violation. The effects of background operators for which experimental limits are not available in literature, namely

$$O_{quqd}^{(1)}, O_{quqd}^{(8)}, O_{uW}, O_{uB}, O_{dG}, O_{dW}, O_{dB}, O_{\phi ud}, O_{qq}^{(3)}, \quad (5.4)$$

were studied up to the strong coupling limit and found either negligible or leading to a distinct event kinematics that are easily distinguishable from that of VBS operators. One background

operator, $O_{\phi q}^{(3)}$, was found to potentially produce an effect up to $\sim 5\sigma$ in significance at the HL-LHC if the present experimental bounds are assumed. It too, however, produces a distinct kinematic signature in which jet p_T is the most affected variable.

The effects of proper VBS dimension-6 operators were studied using their global bounds and applying them to each operator individually. This procedure is justifiable by the fact that correlations between the four operators of interest range between negligible and mild [125]. In the WW scattering process these operators typically affect different helicity combinations and therefore do not significantly interfere. Large possible effects at the HL-LHC, by far exceeding the 5σ threshold, were found for $O_{\phi W}$, $O_{\phi\Box}$, and O_W. The results show that dimension-6 operators cannot be safely ignored in VBS analyses. Indeed, if the Wilson coefficient for O_W is large, the corresponding experimental signature allows the possibility of improving experimental bounds on this operator by using data already collected during Run 2.

6 Neutrino BSM with VBS signatures

Among the several experimental and theoretical motivations for new physics is the case made by *tiny* neutrino masses and their large mixing angles [128, 129]. To reconcile the SM's gauge structure and the renormalizability with oscillation data, and hence nonzero neutrino masses, there must exist new particles that couple to the SM's lepton and Higgs sectors [130]. Such scenarios, which are known collectively as Seesaw models, come in many forms. They range from postulating new gauge symmetries with vastly expanded Higgs sectors to minimal extensions with only a few new fermions or scalars that carry SM gauge charges. Whether neutrino masses are generated in these models at tree-level or at loop-level, the particles responsible for generating neutrino masses can couple to SM states, even appreciably in some scenarios. If these particles are also kinematically accessible, then it may be possible to produce them at collider experiments through a variety of mechanisms, including VBS, thereby establishing a probe of physics beyond the SM [131, 132].

In recent years, LHC searches for particles hypothesized by neutrino mass models have undergone a transformation. More specifically, the adoption of EW VBS production mechanisms, which were unavailable at predecessor colliders like LEP and the Tevatron, has significantly increased the sensitivity to TeV-scale states at the LHC. This includes, for example, the $W\gamma$ fusion channel in searches for heavy Dirac and Majorana neutrinos N by the CMS experiment [133, 134] and WZ fusion in searches for charged Higgs $H^\pm$ by the ATLAS experiment [135]. The providence of these experimental searches stem from equally transformative developments in the theory community, developments that are the result of systematic investigations into the utility of EW VBS in tests of Seesaw models. The creation of dedicated Monte Carlo tools for studying EW VBS in Seesaw models has also played an important role. For recent reviews of such phenomenological developments, see Refs. [136, 137, 138, 131, 132, 139].
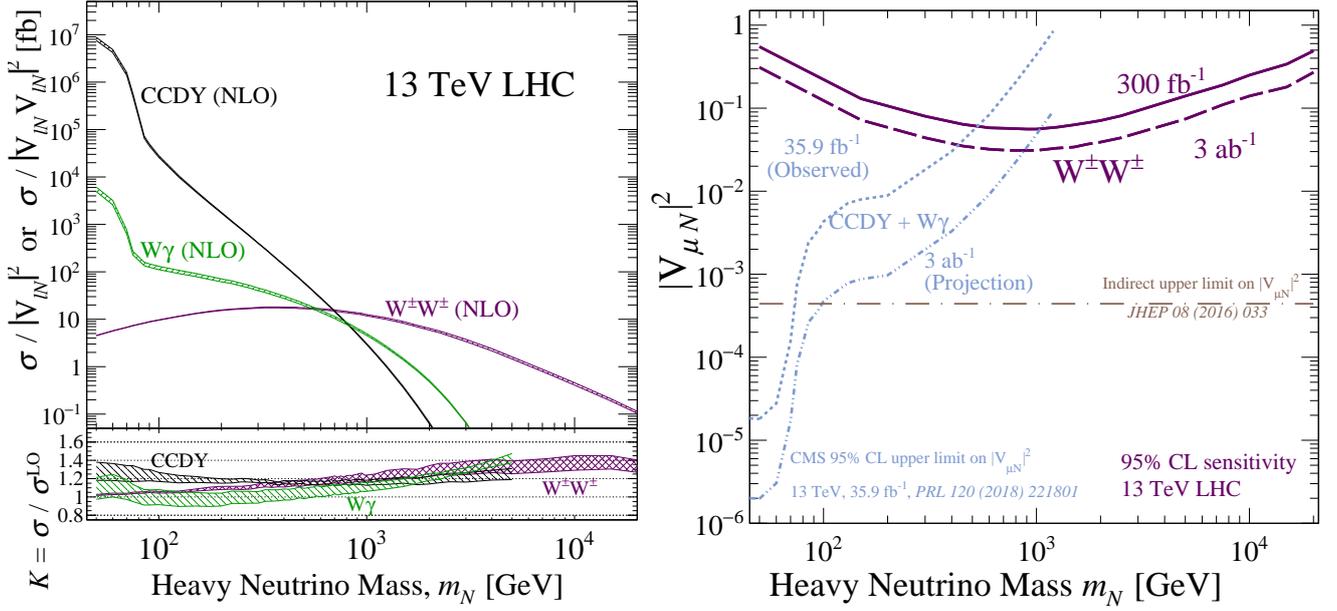
Figure 6.1: Left: Cross section predictions at NLO in QCD at the $\sqrt{s} = 13$ TeV LHC for heavy Majorana neutrinos N production via the charged current Drell-Yan (CCDY), $W\gamma$ fusion, and same-sign $W^\pm W^\pm$ fusion mechanisms, assuming a benchmark active-sterile mixing of $|V_{\ell N}| = 1$. Right: Sensitivity projections for active-sterile mixing of $|V_{\ell N}|^2$ at the LHC for the $W^\pm W^\pm$ channel in comparison to experimental limits [133, 134]. Figures adapted from Ref. [77].

In the following, a brief summary of these theoretical developments is provided. Also given is an outlook for discovering new particles at HL-LHC and future proton colliders with VBS. In Section 6.1, focus is placed on the role of $W\gamma$ and same-sign WW scattering in searches for heavy Dirac and Majorana neutrinos. In Section 6.2, singly and doubly charged Higgs bosons from $\gamma\gamma$ and same-sign WW scattering are considered. Finally, in Section 6.3, sensitivity of same-sign WW scattering to the sole dimension-five operator in the SMEFT is presented.

6.1 Heavy neutrinos from $W\gamma$ and $W^\pm W^\pm$ scattering

In the SM neutrinos are massless [140]. This follows from the absence of right-handed neutrinos ν_R, and hence the lack of Yukawa couplings between the SM Higgs field and left-handed lepton doublets. As fermions without any gauge charges, ν_R are allowed to be their own antiparticles, i.e., be Majorana fermions, and therefore possess right-handed Majorana masses μ_R. Therefore, despite being a natural explanation for nonzero neutrino masses, hypothesizing the existence of at least two ν_R is nuanced [141, 142, 143]. For example: Majorana masses can take values well above and below the EW scale while still reproducing oscillation data. Likewise, the possible dynamical origin of μ_R complicates the low-energy picture because the number of symmetries of the SM with ν_R increases in the absence of masses, e.g., the emergence of a left-right global symmetry. Whether the μ_R are much larger, comparable, or smaller to the EW scale also leads to distinct phenomenologies [141, 142, 143] that are testable, to a degree [132, 139], with VBS.

In searches for Dirac and Majorana neutrinos N with masses above the EW scale, VBS has been indispensable in extending the sensitivity of LHC experiments [133, 134]. In Fig. 6.1 (left),

for example, one sees that the NLO cross section (normalized for an active-sterile mixing $|V_{\ell N}|$ of unity) for the charged-current Drell-Yan (CCDY) process $q\bar{q'} \rightarrow W^{\pm *} \rightarrow \ell^\pm N$ is complemented by the $W^\pm \gamma \rightarrow \ell^\pm N$ and same-sign $W^\pm W^\pm \rightarrow \ell_i^\pm \ell_j^\pm$ scattering processes for N masses around $m_N \sim 1$ TeV [77]. Fully differential computations up to NLO in QCD with parton shower (PS)-matching are available using the HEAVYN Universal FEYNRULES Object (UFO) model libraries for Majorana [144] and Dirac [139] N. Predictions up to NLO+PS with dimension-six operators are also available if using the HEAVYN_vSMEFTDIM6 UFO [79].

The same-sign $W^\pm W^\pm$ process is special for several reasons, including: (a) its relationship to the neutrinoless $\beta\beta$ decay process [145, 146]; (b) its accessibility to $\ell = \mu$ and τ lepton flavors, which are not accessible in nuclear decay experiments; and (c) its sensitivity to violations of s-wave perturbative unitarity [77]. As shown in Fig. 6.1(R), due to the non-resonant nature of $W^\pm W^\pm$ process, LHC experiments are sensitive to N masses around $m_N \sim 10$ TeV for $|V_{\ell N}|^2 \sim 0.1$, when employing basic VBS selection cuts [77].

Also of special interest is the $W\gamma$ fusion channel. The channel, which features contributions from elastic [147], inelastic [148, 144], and deeply inelastic [146] initial-state photons, can be added coherently to the CCDY process whenever searches are inclusive to forward jet activity [148]. For TeV-scale Dirac and Majorana neutrinos, Fig. 6.2 (left) shows, for example, that including the $W\gamma$ channel can improve sensitivity to $|V_{\ell N}|^2$ by at least an order of magnitude for TeV-scale N [149]. Such improvements hold for signal categories with final-state τ leptons [150, 149]. With newer analysis strategies, active-sterile mixing as low as $|V_{\ell N}|^2 \sim 10^{-3}$ can be probed at the HL-LHC [149].
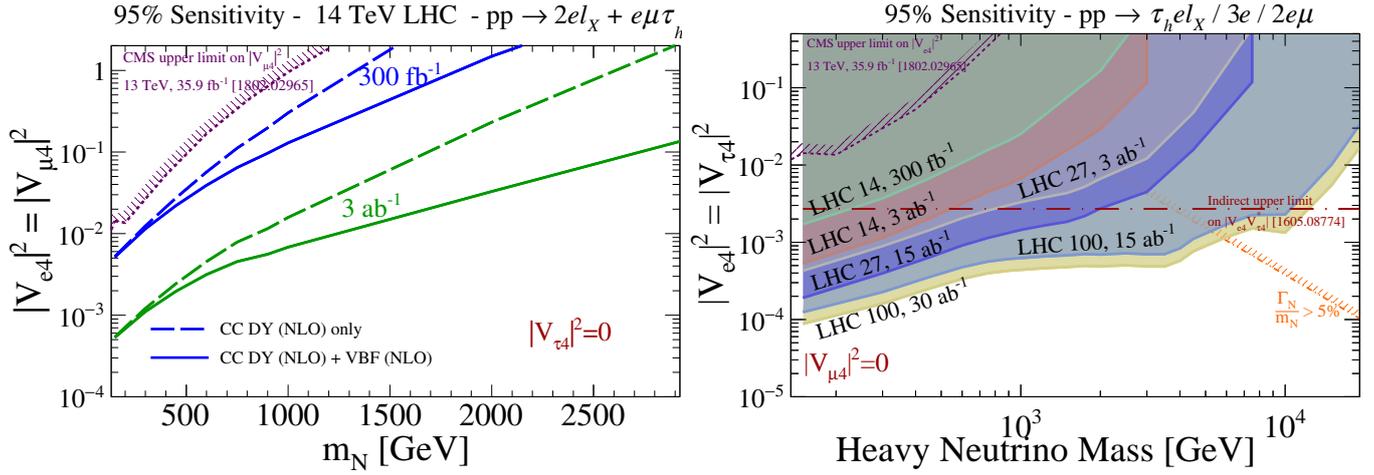
Figure 6.2: Left: Sensitivity projections for active-sterile mixing of $|V_{\ell N}|^2$ at the LHC when using only the Drell-Yan channel (dashed) and when augmented by the $W\gamma$ fusion channel (solid) [139]. Also shown for reference are LHC limits with $\mathcal{L} \approx 36$ fb^{-1} of data [133]. Right: Sensitivity projections for active-sterile mixing of $|V_{\ell N}|^2$ at the LHC and potential successor experiments using the Drell-Yan and $W\gamma$ channels [139].
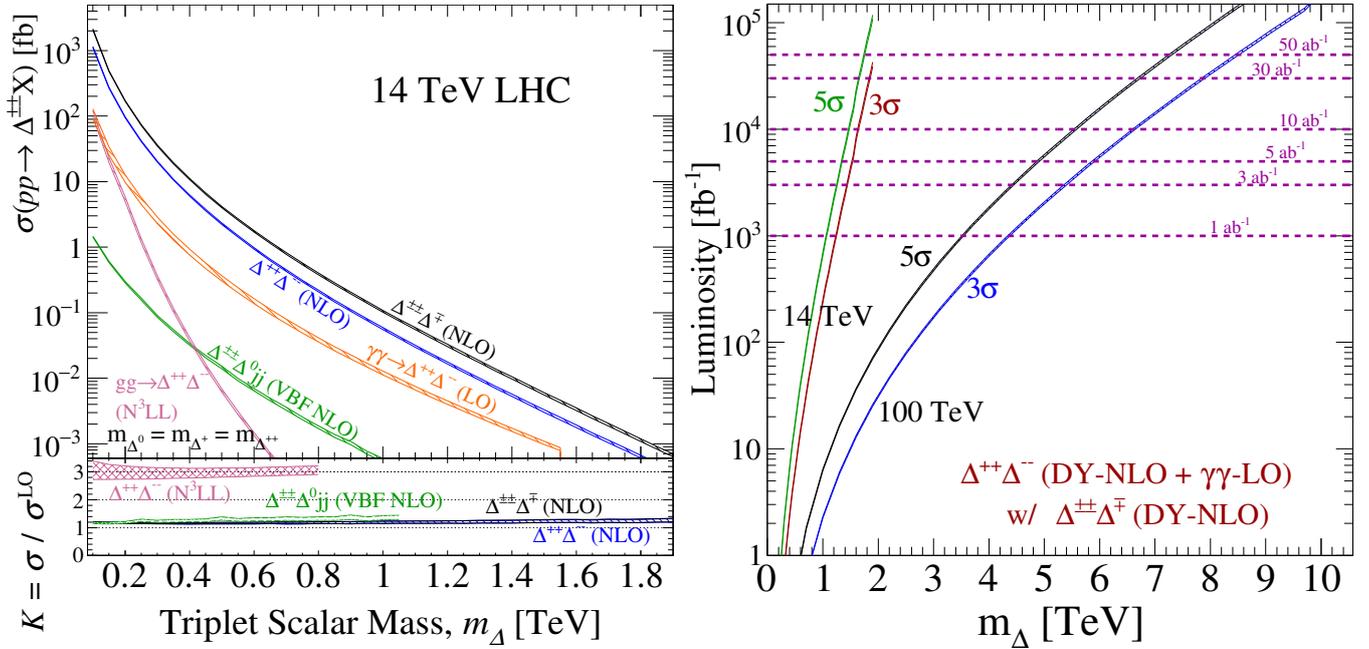
Figure 6.3: Left: High-precision cross sections predictions at the $\sqrt{s} = 14$ TeV LHC for doubly charged Higgs $\Delta^{\pm\pm}$ production via various mechanisms in the Type II Seesaw. Right: Sensitivity projections to $\Delta^{\pm\pm}$ for the LHC and a hypothetical collider at $\sqrt{s} = 100$ TeV [100].

Even smaller values of active-sterile mixing are also available at prospective successors of the LHC as shown in Fig. 6.2 (right). Both VBS channels are also sensitive to dimension-six operators involving heavy neutrinos [79].

6.2 New Higgs bosons from $\gamma\gamma$ and $W^{\pm}W^{\pm}$ scattering

In the Type II Seesaw model [151, 152, 153, 154, 155], light neutrino masses are understood to originate through the spontaneous breaking of lepton number symmetry by a new scalar $\hat{\Delta}$ when it acquires a small vacuum expectation value (vev)

$v_{\Delta} = \sqrt{2}\langle\hat{\Delta}\rangle \ll v_{EW} = \sqrt{2}\langle\Phi\rangle \approx 246$ GeV. Here, $\hat{\Delta}$ denotes a gauge eigenstate, whereas Δ (no hat) denotes a mass eigenstate. Φ is the SM Higgs field and v_{EM} is its vev. The new field is formally a complex triplet under the SM's SU(2)$_L$ gauge group and carries a hypercharge of $Y = +2$. This means that after EW symmetry breaking one generates the following field content in addition to the SM particles: a doubly charged Higgs boson, $\Delta^{\pm\pm}$; a singly charged Higgs boson, $\Delta^{\pm}$; an electrically neutral, CP even(odd) Higgs boson, Δ^0 (ξ^0).

EW symmetry breaking proceeds in the usual way for the

SM sector. The exception are neutrinos: they obtain left-handed Majorana masses that are proportional to v_Δ and their Yukawa coupling to $\hat\Delta$. As a consequence, the decay rates of the charged and neutral Δ to leptons are proportional to light neutrino masses and the measured values of the PMNS matrix. If the Δ are realized in nature, then collider experiments can potentially probe the ν_τ mixing sector, which is poorly constrained by oscillation experiments [156, 157]. For a concise summary of this symmetry breaking pattern and phenomenology, see Ref. [100] and references therein. It is important to stress that this model is an example of generating of a neutrino mass model that does not contain right-handed neutrinos.

At the LHC, the production of singly and double charged Δ can proceed through a variety of mechanisms, including the Drell-Yan ($q\overline{q'}$ annihilation) channels

$$q\overline{q'} \rightarrow \Delta^{+(+)}\Delta^{-(-)}, \Delta^{\pm\pm}\Delta^{\mp}, \Delta^{\pm}\Delta^{0}, \Delta^{\pm}\xi^{0}, \quad (6.1)$$

the gluon-gluon fusion channel

$$gg \rightarrow \Delta^{++}\Delta^{--}, \Delta^{+}\Delta^{-}, \quad (6.2)$$

the photon-photon scattering channel

$$\gamma\gamma \rightarrow \Delta^{++}\Delta^{--}, \Delta^{+}\Delta^{-}, \quad (6.3)$$

as well as the WZ/γ and same-sign WW scattering channels

$$W^{\pm}Z, W^{\pm}\gamma \rightarrow \Delta^{\pm\pm}\Delta^{\mp}, \Delta^{\pm}\Delta^{0}, \Delta^{\pm}\xi^{0}, \Delta^{\pm}, \quad (6.4)$$

$$W^{\pm}W^{\pm} \rightarrow \Delta^{\pm\pm}, \Delta^{\pm\pm}\Delta^{0}. \quad (6.5)$$

Many other channels, particularly via the VBS mechanism, are also possible in the Type II Seesaw. However, a fully comprehensive comparison of all VBS production channels does not yet exist. What does exist is a high-precision comparison of $\Delta^{\pm\pm}$ production mechanisms [100], and is shown for the $\sqrt{s} = 14$ TeV LHC in Fig. 6.3(L). From the figure we see that many channels are now known at NLO in QCD or with higher precision. While the total Drell-Yan cross section has been known at NLO in QCD for some time [158], fully differential predictions at NLO and with parton shower matching have only recently been made available using the TypeIISeesaw UFO [100].

As with the SM Higgs, the VBS channels possess smaller cross sections than the Drell-Yan modes at the LHC. At the same time, the VBS channels possess more handles to distinguish them from background processes. In particular, the $\gamma\gamma$ channel, whose PDF uncertainties are now under definitive control [100], can appear in ultra peripheral proton collisions and give rise to exceptionally clean signatures. An outlook for the LHC and a potential successor at $\sqrt{s} = 100$ TeV are summarized in Fig. 6.3(R). For $\mathcal{L} = 3 - 5$ ab^{-1}, the LHC is sensitive to pair and associated production of $\Delta^{\pm\pm}$ with masses up to $m_\Delta \sim 1.2 - 1.5$ $(1.1 - 1.4)$ TeV at 3 (5) σ as reported in Ref. [100].

6.3 The Weinberg operator in $W^{\pm}W^{\pm}$ scattering

If those particles that are responsible for generating neutrino masses are too heavy to be directly probed at the LHC, then
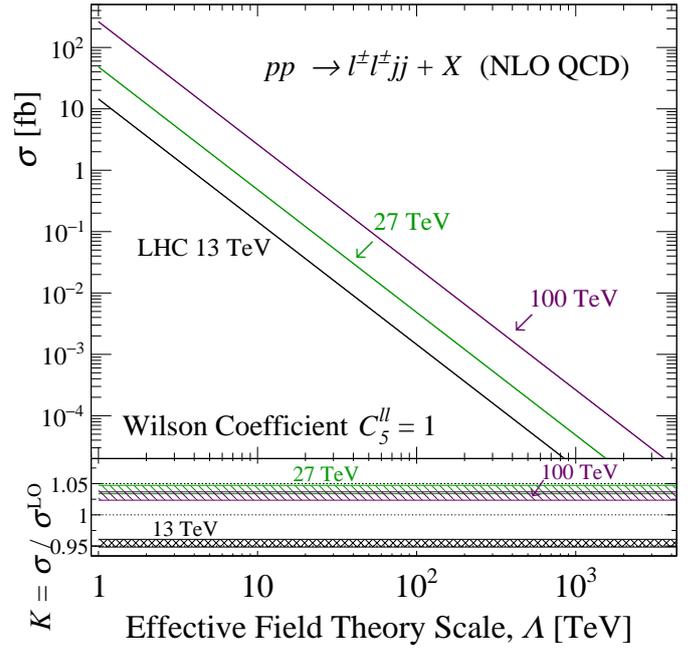
Figure 6.4: Cross section predictions at NLO in QCD for the $W^{\pm}W^{\pm} \rightarrow \ell_i^{\pm}\ell_j^{\pm}$ process when mediated by the Weinberg operator for representative pp collider energies [78].

their impact on SM interactions can still be described through the effective field theory formalism. In particular, the SMEFT framework classifies and arranges the (composite) field operators that remain after decoupling (integrating out) ultra heavy particles into a set of operators that are manifestly invariant under the SM gauge symmetries. For reviews of this framework, see Refs. [124, 159, 160]. While the power counting of SMEFT extends the SM only by operators that start at dimension $d \geq 5$, of notable interest is the solitary operator at dimension $d = 5$, which is given by

$$\mathcal{L}_5 = \frac{C_5^{\ell_i\ell_j}}{\Lambda}[\Phi\cdot\overline{L}_{\ell_j}^c][L_{\ell_j}\cdot\Phi]. \quad (6.6)$$

Here $C_5^{\ell_i\ell_j}$ is the Wilson coefficient for lepton flavors $\ell_i, \ell_j \in \{e, \mu, \tau\}$, Λ is the EFT cutoff scale, Φ is the SM Higgs field, and L_ℓ is the SM left-handed lepton doublet of flavor ℓ.

The so-called Weinberg operator [161] is capable of generating Majorana neutrino masses after EW symmetry breaking, and therefore serves as a way to parameterize a key aspect of neutrino mass models in experiments. However, other operators at $d = 6, 7$ or higher may also been needed to fully parameterize other aspects of the theory at low energies. This holds so long as neutrinos are Majorana fermions and that their masses are not generated instead at a higher dimension, which can be the case for some loop-level neutrino mass models [162, 131].

While the ratio $|C^{ee}/\Lambda|$ is strongly constrained by nuclear neutrino-less $\beta\beta$ decay experiments [163], the Wilson coefficients for other lepton flavors are actually poorly constrained [164, 78]. It is also possible that C^{ee} is immeasurably small due to exact symmetries or accidental cancellations, resulting in the so-

19

called "funnel region" for normal ordering of neutrino masses.

In such circumstances, the Weinberg operator can be probed at the LHC through the same-sign WW scattering channel, which is given for $\ell_i = e, \mu, \tau$, but $\ell_j = \mu, \tau$, by

$$W^{\pm}W^{\pm} \rightarrow \ell_i^{\pm}\ell_j^{\pm}. \tag{6.7}$$

Recent developments allow the Weinberg operator to be efficiently modeled at collider experiments by importing the SMWEIN-BERG UFO into state-of-the-art Monte Carlo event generators [78]. As shown in Fig. 6.4, the $W^{\pm}W^{\pm} \rightarrow \ell_i^{\pm}\ell_j^{\pm}$ cross section at NLO in QCD for the $\sqrt{s}$ = 13 TeV LHC can reach appreciable values, even if $\Lambda/C^{\ell_i\ell_j} \sim \mathcal{O}(10)$ TeV, and more so at higher collider energies. With a relatively simplified analysis, scale and ratio combinations up to

$$|\Lambda/C^{\mu\mu}| \sim 8.3 \; (11) \; \text{TeV} \tag{6.8}$$

can be probed with $\mathcal{L}$ = 300 (3000) fb^{-1} at the LHC [78].

7 Event identification with machine learning

At the HL-LHC, more collisions per bunch crossing and higher granularity data will pose major challenges for triggering and event reconstruction. It will be important to maximize the VBS signal acceptance already at the hardware trigger level in order to ensure sensitivity to the highest-background channels (see Section 9). In addition, the large increase in integrated luminosity could allow for several challenging measurements, like the polarization fractions in VBS events or all-hadronic final states. However, disentangling such signatures from the overwhelming background will require improved signal-enhancing algorithms. Given the complex event topology of VBS events and the presence of very similar background processes occurring at significantly higher rates, it is natural to consider Machine Learning (ML) algorithms as a tool for VBS event reconstruction.

7.1 Triggering of VBS events

With an average number of collisions per bunch crossing (also known as "pileup") increasing from 50 to 200, one of the most crucial aspects for VBS at the HL-LHC will be to maintain or improve the signal acceptance (detector upgrades for HL-LHC are discussed in Section 9). A natural candidate for doing so is better triggering on the forward quark jets. To this end, three ingredients will be important in HL-LHC: better pileup mitigation, better jet resolution, and better quark/gluon jet separation.

7.1.1 Quark versus gluon jet discrimination

In CMS, the new CMS Endcap High-Granularity Calorimeter (HGCAL), which covers a pseudorapidity of $1.5 < |\eta| < 3.0$, offers unprecedented transverse and longitudinal segmentation, allowing for accurate measurements of the shower development and narrowness of VBS jets [165]. With this improved forward jet resolution, it is feasible to cleanly trigger on and reconstruct narrow VBS jets, thereby serving as a basis for dedicated Level

1 (L1) hardware triggers. The energy resolution is also significantly improved, meaning any potential selections placed on the invariant mass of forward jet pairs are more efficient. In addition to the excellent energy resolution provided by HGCAL, the inclusion of tracking up to η = 2.4 and Particle Flow (PF) [166] in the CMS L1 hardware trigger can allow for excellent quark versus gluon discrimination, as variables like charge multiplicity can be computed in real-time. It is therefore feasible, and highly desirable, to design algorithms capable of discriminating between three classes of jets at the hardware triggering level: high-p_T quark-seeded jets, high-p_T gluon-seeded jets, and low-p_T pileup jets. Simple deep neural networks (DNN) for quark (q) and gluon (g) discrimination already exist, as discussed at length in Ref. [167] and as illustrated in Fig. 7.1. Here, simple ML models are compared to a likelihood-based q/g discriminator, the current default in CMS. ML algorithms using the jet constituents as inputs (referred to as "sequential" and "Jet Image") are notably better in telling quark and gluon jets apart than the likelihood-based equivalent and would be suitable candidates for deployment in the L1 trigger.

Due to competing demands, algorithms running in the L1 trigger hardware must be extremely fast and compact. The HLS4ML [168, 169, 170, 171] library has been designed to enable the conversion of ML models into ultra low latency, low-resource FPGA firmware, making it feasible to deploy algorithms like those shown in Fig. 7.1 into the trigger. One should caution, however, that this perspective is optimistic. There are many challenges to be able to employ an ML model with competitive performance and low FPGA resources.

7.1.2 Jet substructure

With the PF algorithm available at L1, it is interesting to ask whether there is any gain in identifying and triggering on hadronically decaying vector bosons. This could be done by targeting energetic vector bosons with p_T just above 200 GeV, whose decay products are merged into single large-radius jets, so-called *boosted jets*. Several DNNs dedicated to the identification of boosted jets already exist, and some have also been optimized to function in the highly demanding environment of the L1 trigger [168]. However, more detailed studies are required to identify any possible gain with respect to the trigger algorithms currently in place that trigger on high-p_T jets. The additional gain in a dedicated substructure path might be insignificant if most events already pass the standard L1 threshold. The combination of new, high-resolution inputs available in the hardware trigger, the HLS4ML workflow, and highly performant networks can lead to significantly higher VBS signal acceptance algorithms in HL-LHC, especially focusing on jet-identification algorithms based on PF candidates.

7.2 Vector boson polarization

With exclusion limits being pushed to higher and higher resonance masses, searches for physics beyond the SM at the LHC are beginning to reach a phase space where hypothetical new particles can no longer be produced directly, though many exceptions to this also exist. In this era, doing precision measurements that target BSM physics is a natural next step. The study
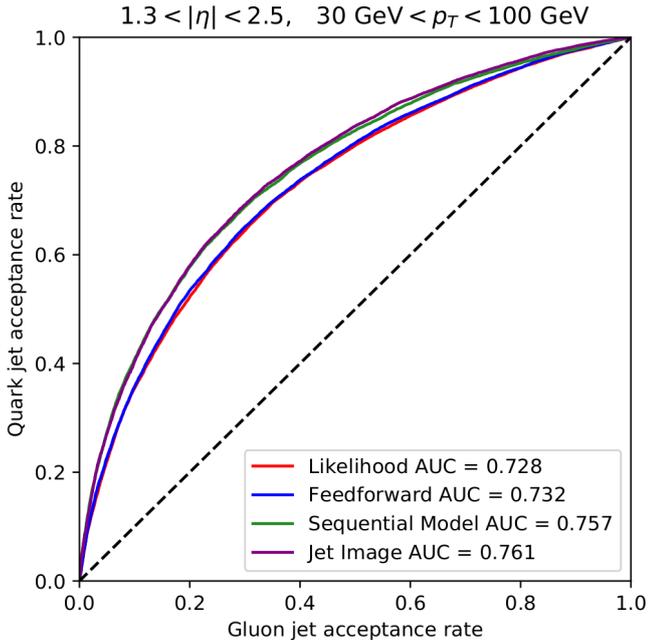
Figure 7.1: ROC curves showing the quark-jet acceptance rate as a function of the gluon-jet acceptance rate for each quark/gluon discriminator in the detector's endcap region of $1.3 < |\eta| < 2.5$ and $30 < p_T < 100$ GeV, from Ref. [167]. The red line corresponds to the benchmark likelihood-based discriminator. The blue, green and purple lines correspond to three neural network models.

of 2→2 scattering of EW bosons is a direct probe of the quartic gauge coupling, a way to probe the Higgs coupling without the Higgs boson [174], and a way to indirectly look for BSM signatures [175, 176, 177].

Of especially high interest is a study of the polarization fraction in VBS events, as these are sensitive to BSM enhancements [176]. At scattering energies that are large compared to weak boson masses, VBS can probe BSM interactions that mainly couple to longitudinally polarized vector bosons. With 90% of SM VBS events being of the $W_T W_T$-type (for $M_{VV} > 250$ GeV), SM $W_T W_T$ becomes an irreducible background when attempting to look for enhancement effects in the longitudinal channel. It is therefore desirable to discriminate transversely polarized vector bosons from longitudinally polarized vector bosons. Reconstructing the vector boson polarization is difficult in leptonic final states due to the missing four-vector of final-state neutrinos. One solution would be to use the all-hadronic final state, where all the final state particles are visible. In addition, the large branching ratio of $W \rightarrow q\bar{q}$ is beneficial when targeting the relatively rare $W_L W_L$ channel. The polarization could then be accessed through both the forward VBS quark-jets, as well as through the quark decay products of the hadronically decaying vector bosons. As the BSM contribution grows with energy, the vector bosons might have a large Lorentz boost resulting in their decay products being contained in a single, large-radius jet. These could be identified as vector-boson jets us-

ing dedicated jet substructure techniques. The final state would therefore consist of two central, large-radius jets with masses compatible with the W mass, and two forward quark jets. Extracting the polarization fraction from this is a two-stage problem: First, the EW VBS process must be distinguished from QCD diboson processes. Secondly, one would need to discriminate longitudinally polarized vector bosons from transversely polarized vector bosons (as well as, possibly, the jet charge). Both of these tasks could be solved highly accurately with DNNs, allowing for two powerful tests of the SM: a cross section measurement in a $W_L W_L$ enriched region looking for deviations from the SM prediction, as well as a full measurement of the VBS helicity fractions.

7.2.1 Jet substructure and polarization

To identify hadronically decaying vector bosons with $p_T > 200$ GeV, jet substructure variables are usually used. These include methods for improving the jet mass resolution by removing soft and wide angle radiation, called grooming [178, 172, 179], and methods for computing the probability of a jet consisting of two or more sub-jets [180]. For reviews of such techniques, including with the use of ML, see Refs. [181, 182, 183].

Spin correlation in the decays of boosted objects is important in real life measurements. For example: when a transversely polarized W boson decays in its rest frame, its decay products are back-to-back and preferentially aligned parallel or anti-parallel to the W's spin axis. When boosting the momentum of W and its decay products (partons in the case of hadronic decays) to the lab frame, the result is an asymmetric p_T distribution among the constituents. For highly boosted W bosons, final-state partons may be overlapping. For longitudinally polarized W bosons, decay products are preferentially aligned orthogonally to the W's spin axis, and leads to a softer asymmetry. This is illustrated in the lab frame in Fig. 7.2 (top) for a longitudinal W (Left) and transverse W (Right). As jet grooming removes softer, wider angle radiation, it will often completely remove the softer of the two quark sub-jets in the hadronic decays of highly boosted W bosons.

Beyond jet grooming, spin-correlation also impacts N-subjettiness τ_N, which measures the numbers of principal axes (or "prongs") in a jet [180]. More specifically, the N-subjettiness ratio $\tau_{MN} = \tau_M/\tau_N$ is a measure of whether a jet is better described as an object with M or N prongs (sub-jets). As τ_{21} is a measure of compatibility for having one vs two axes within a jet, it will not be able to identify the 2-prong structure when overlapping partons are present but incidentally "groomed away." This configuration is illustrated in Fig. 7.2 (top). The quantitative effect of this is shown in Fig. 7.2 (bottom), where we show scatter plots of the soft drop mass variable [184], i.e., the invariant mass after the algorithm has been applied, as a function of τ_{21} for longitudinal W (Left) and transverse W (Right). A large fraction of transversely polarized W's are reconstructed as having a soft-drop mass close to zero and compatibility with a 1-prong hypothesis. This makes jet substructure algorithms less efficient in detecting transversely polarized, hadronically decaying vector bosons [173, 172].
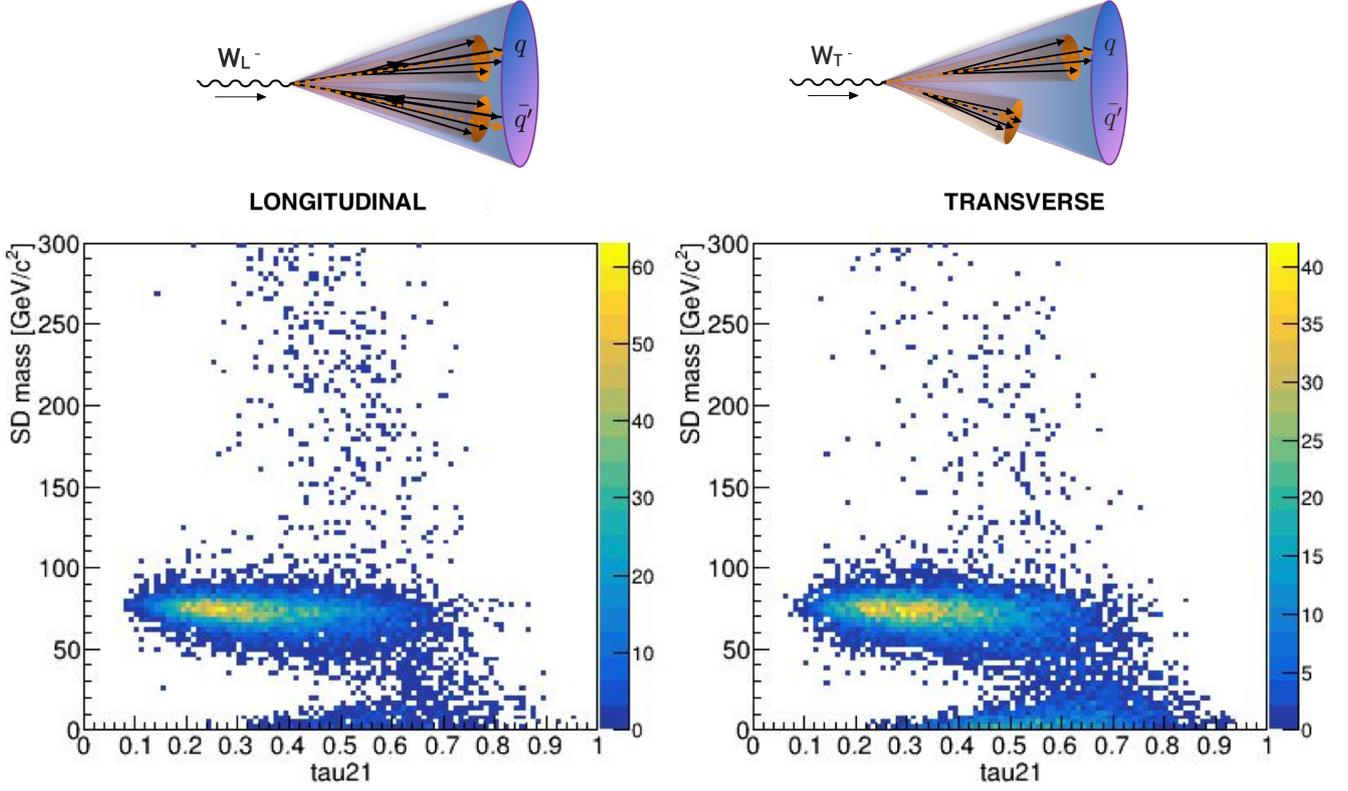
Figure 7.2: Top: Illustration of the decays of high-p_T W_L (Left) and W_T (Right) bosons in the lab frame showing that overlapping decay products are preferentially symmetric (for W_L) or asymmetric (for W_T) due to spin correlation. Lower: Scatter plot of the soft drop (SD) mass variable as a function of the "N-subjettines" variable τ_{21} for W_L (Left) and W_T (Right). Transversely polarized vector bosons (right) more frequently get reconstructed with a soft drop mass of zero and a 1-prong like substructure (i.e. larger τ_{21} values) due to its decay products being emitted anti-parallel to the W momentum and falling out of the jet cone during the grooming process [172, 173].
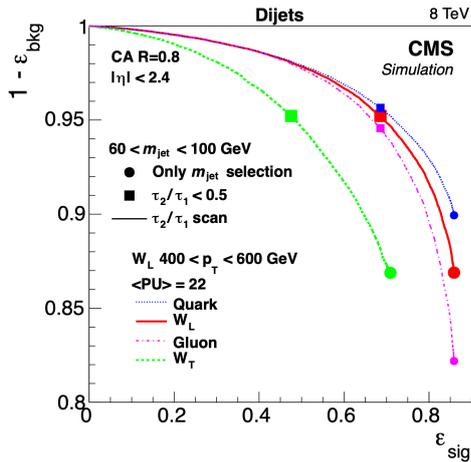
Figure 7.3: Efficiency for correctly identifying longitudinal (red) and transverse (dotted green) vector bosons versus 1-efficiency for tagging quark (dotted blue) or gluon (dotted pink) jets [172].

The resulting identification efficiency for transversely polarized vector bosons is significantly reduced, as shown in Fig. 7.3.

If it is desirable to not only enhance the $W_L W_L$ channel, but to measure all polarization components, for instance in a simultaneous fit to extract the polarization density matrix, it is crucial to not only develop algorithms for discriminating between vector boson polarizations, but also substructure algorithms which are equally efficient for both W_T and W_L. Both of these issues can be addressed using particle-based DNNs, for instance permutation-invariant algorithms like graph neural networks [185, 186]. Advanced graph neural networks for discriminating between transversely and longitudinally polarized vector bosons is currently being studied. In the proof-of-principle study of Ref. [173], it has been demonstrated that relatively simple DNNs can obtain a factor of two enhancement in signal sensitivity for longitudinally polarized vector bosons.

Importantly, and as pointed out above, in order to access polarization in the all-hadronic final state, not only a polarization identification algorithm is needed. A "polarization un-biased" jet substructure algorithm will additionally be required in order to recover inefficiencies observed with current vector boson tagging algorithm for transversely polarized vector bosons.

In addition, such single-object polarization identification algorithms might not reach the required sensitivity, and it could be necessary and beneficial to include the full event informa-

tion. This includes correlations between the two vector boson jets and correlations between the forward VBS jets. An example of this can be found in Ref. [187].

The most challenging part of any such data-driven algorithm will be how to calibrate it using standard candles, developing appropriate systematic uncertainties and corrections, as well as accounting for potential energy-dependence of the algorithm. This is highly dependent on the final selected algorithm and we leave this discussion for future studies. With these algorithms at hand, several interesting measurements can potentially be considered at HL-LHC. For example: extracting the components of the polarization density matrix using the all hadronic final state, performing differential measurements of the polarization fraction versus energy, and looking for BSM enhancements in high-energy $W_L W_L$ events.

7.3 Summary

ML will be a critical part of VBS searches in HL-LHC on multiple fronts. This includes, but is not limited to, algorithms for improving the VBS signal acceptance in the hardware trigger, for reconstructing the complex VBS topology, for discriminating between VBS and background processes, and for discriminating between vector boson polarizations. Exploring the all-hadronic final state might be feasible using advanced DNNs to reconstruct vector boson polarization and charge, and for developing jet substructure taggers with higher efficiency for transversely polarized vector bosons than current algorithms. The development of such ML solutions opens the door for several exciting measurements at HL-LHC, like measurements of the polarization fraction versus energy or a simultaneous fit of the components of the polarization density matrix. Extremely high signal acceptance and low background rates is needed, making highly accurate deep neural networks excellent candidates for the task.

8 Anomaly detection with machine learning

VBS represents a sensitive probe of both EW symmetry breaking and new physics. If the couplings of the Higgs boson to vector bosons deviate from the SM prediction, the cross sections of VBS processes will increase with center-of-mass energy up to the scale of new physics. In addition, many BSM models predict an extended Higgs sector. The contribution from new resonances can also increase the VBS cross section in certain regions of phase space. This section is dedicated to a concrete example of the use of ML for the observation of such effects.

Among the many VBS processes, the same-sign scattering, golden process $W^\pm W^\pm jj \to \ell^\pm \ell^\pm \nu\bar{\nu} jj$ has already been observed at the LHC (see Section 1.1). This is similar to the case of the trilepton channel, $W^\pm Z jj \to \ell^\pm \nu \ell^+ \ell^- jj$ [13, 32]. While the production cross sections of the $Z(\to \ell^+ \ell^-)Z(\to \nu\bar{\nu})jj$ and $Z(\to \ell_i^+ \ell_i^-)Z(\to \ell_k^+ \ell_k^-)jj$ channels [28, 27] are small, they too have been observed due to their small backgrounds. There is also recent evidence for the $Z\gamma jj \to \ell^+ \ell^- \gamma jj$ channel [188], which benefits from its larger production rate. Even though
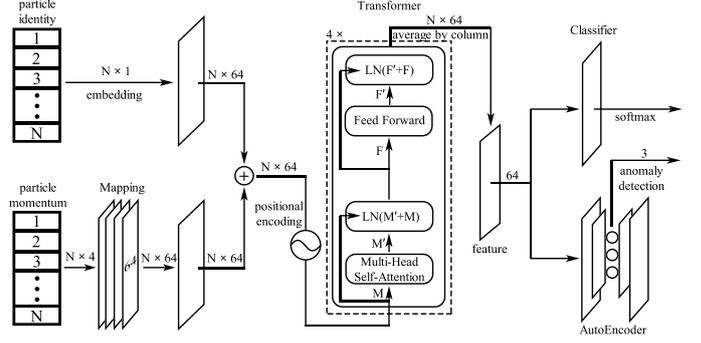
Figure 8.1: Architecture of neural network [189].

the opposite-sign $W^+ W^- jj \to \ell^+ \ell^- \nu\bar{\nu} jj$ process has the largest production rate, it has not been observed yet, due to the huge $t\bar{t}$ background.

Understanding the polarization of the gauge bosons is an important step after the measurements of the VBS processes. There are studies aiming to determine the polarization of gauge bosons in the $W^+ W^-$ channel [190, 102, 47], in the fully leptonic $W^\pm W^\pm$ channel [48], in the fully leptonic WZ/ZZ channels [103], in SM Higgs decay modes [191] and in generic processes with boosted hadronically decaying W boson [192]. Various kinematic observables have been proposed in these works to discriminate the longitudinal and transverse polarizations of gauge bosons. Several recent studies have shown that deep neural network with input of final states momenta can be used for regression of the lepton angle in the gauge boson rest frame [193, 187] and classification of events with different polarizations [194, 195].

Reference [189] in particular focuses on the fully leptonic and semi-leptonic channels of the $W^+ W^-$+jets process. There, the authors propose a neural network based on the Transformer architecture [196] to learn the features of the VBS process, including its polarization. The SMEFT and 2HDM are considered as examples demonstrating that this method is able to test a wide class of BSM physics which contribute to VBS.

8.1 Analysis procedure

The signal and background events in Ref. [189] are generated with the MadGraph5_aMC@NLO [88, 89] framework, in which the Madspin is used for the decays of heavy SM particles. The interference between the EW amplitude at α_{EW}^4 and mixed EW-QCD amplitude at $\alpha_s^2 \alpha_{\text{EW}}^2$ production is ignored. The partonic center-of-mass frame is taken as the reference frame for defining the vector boson polarization in this work, i.e., the rest frame defined by the two initial parton in the $qq' \to W^+ W^- jj$ process. Focus is placed on the dileptonic and semi-leptonic channels of EW $W^+ W^- jj$ production. The dominant backgrounds are from QCD production of $t\bar{t} + X$ process, single top production, mixed EW-QCD production of WW/WZ, and the EW production of WZ pairs. At this stage of event generation, heavy resonances are not decayed and the transverse momenta of final-state QCD partons must be greater than 20 GeV. The corresponding fiducial cross sections (σ^{fid}) at $\sqrt{s} = 13$ TeV are listed in the second column of Table 8.1.
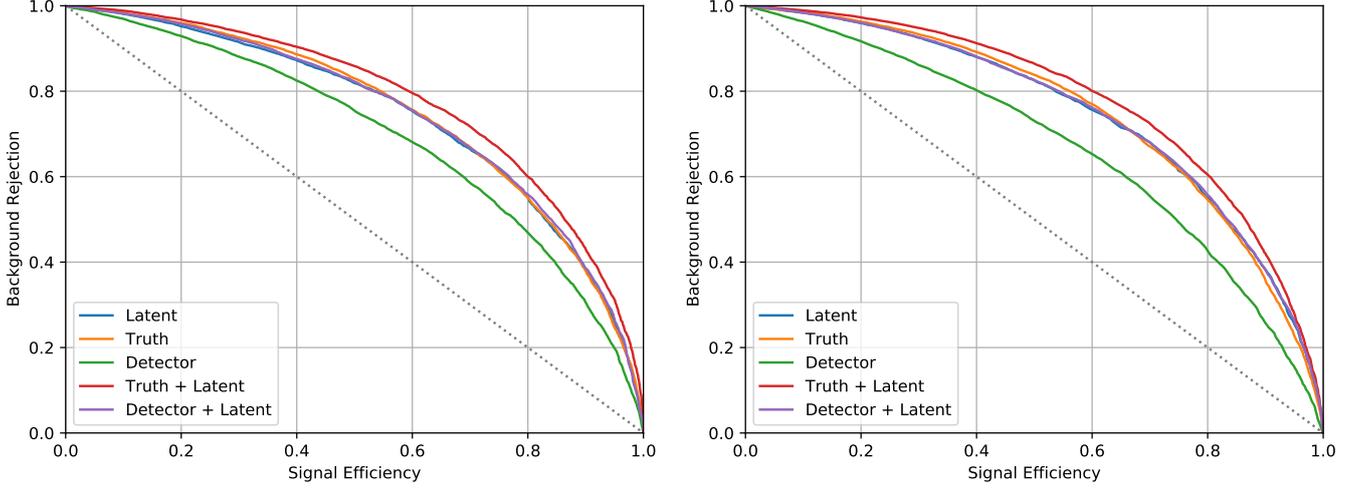
Figure 8.2: Left: Comparison of the discriminating power of methods with different input variables in the dileptonic channel. Right: Same, but for the semi-leptonic channel. Note the variables used for plotting the ROC is different from that in the dileptonic channel. Adapted from Ref. [189]
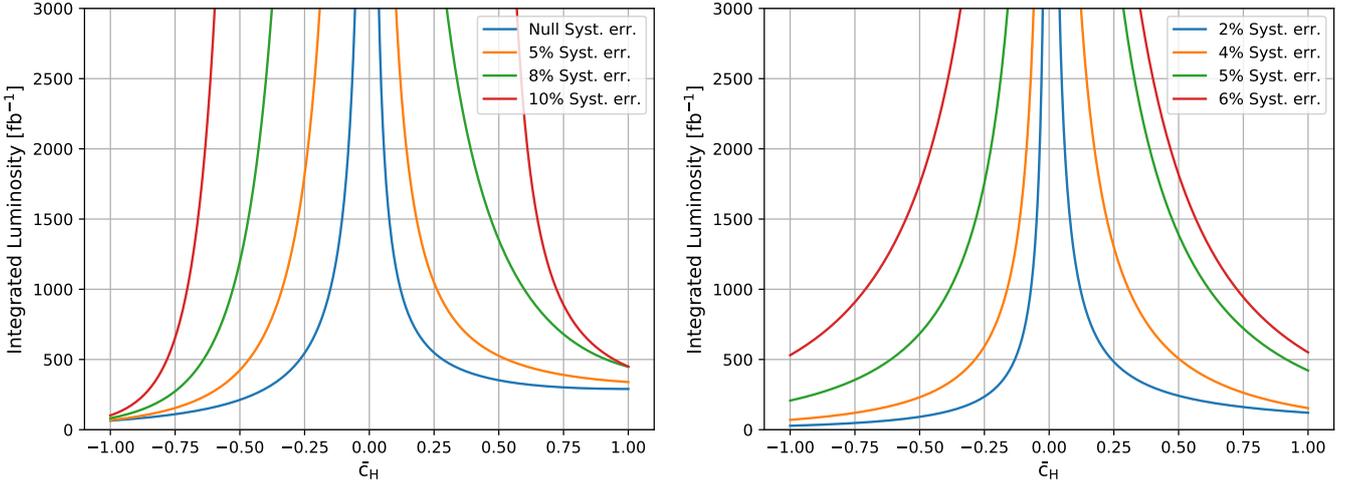
Figure 8.3: Integrated luminosity required to probe the signal (with different $\bar{c}_H$) at 95% C.L. in the dileptonic channel (Left) and semi-leptonic channel (Right). Several different systematic uncertainties are considered. From Ref. [189].

The events are divided into two classes with the following pre-selection [7]:

- **Dilepton:** exactly two opposite sign leptons with $p_T(\ell) >$ 20 GeV, $|\eta(l)| < 2.5$; at least two jets with $p_T(j) >$ 20 GeV, $|\eta(j)| < 4.5$; the two jets with leading p_T should give large invariant mass ($m_{jj} > 500$ GeV) and have large pseudorapidity separation ($|\Delta\eta|_{jj} > 3.6$); no b-tagged jet in the final state.

- **Semi-Lepton:** exactly one charged lepton with $p_T(\ell) >$ 20 GeV, $|\eta(l)| < 2.5$; at least four jets with $p_T(j) >$ 20 GeV, $|\eta(j)| < 4.5$; the pair of jets with the largest invariant mass ($m_{jj} > 500$ GeV) that also satisfies $|\Delta\eta_{jj}| >$ 3.6 is taken as the forward-backward jet pair; (4) among the remaining jets, the jet pair with invariant mass closest

to the W boson mass is regarded as the jet pair from W decay.

The cross sections for signal and backgrounds after the dilepton and semi-lepton selections are provided in the third and fourth columns of the Table 8.1, respectively.

The pre-selected events are fed into the network for learning the features. The input for the network of dileptonic channel consists of the momenta of two leptons, the forward and backward jets, the sum of all detected particles, and the sum of jets that are not assigned as forward-backward jets. The input for the network of semi-leptonic channel consists of the momenta of the lepton, the forward and backward jets, the two jets from W decay, the sum of all detected particles, and the sum of remaining jets.

	σ^{fid} [pb]	$\sigma^{\ell\ell}$ [fb]	$\sigma^{\ell j}$ [fb]
tt_ℓ	210.3	139.8	3007.6
$tW_\ell/t_\ell W$	15.9	11.6	224.6
$W_\ell W jj^{\text{QCD}}$	4.68	14.7	340.5
$W_\ell Z jj^{\text{QCD}}$	2.20	4.49	165.7
$W_\ell Z jj^{\text{EW}}$	0.487	3.68	22.2
$W_\ell W jj^{\text{EW}}$	0.738	4.36	37.3

Table 8.1: Production cross sections of signal and background processes before (σ^{fid}) and after pre-selections cuts for the dilepton ($\sigma^{\ell\ell}$) and semi-lepton ($\sigma^{\ell j}$) categories, for proton-proton collisions at $\sqrt{s}$ = 13 TeV. In the column σ^{fid}, fiducial cuts are applied. Adapted from Ref. [189].

$\bar{c}_H$	-1.0	-0.5	0	0.5	1.0
$\sigma^0_{m_{jj}>500}$ [fb]	440.6	421.8	419.7	426.7	436.2
σ_{ll} [fb]	4.82	4.44	4.36	4.48	4.62
σ_{lj} [fb]	40.2	37.7	37.3	37.9	39.3
$\sigma^{LL}_{m_{jj}>500}$ [fb]	46.29	29.68	25.84	28.79	34.01
σ^{LL}_{ll} [fb]	0.754	0.397	0.314	0.356	0.462
σ^{LL}_{lj} [fb]	5.28	3.04	2.40	2.79	3.50

Table 8.2: $\sigma^0_{m_{jj}>500}$ and $\sigma^{LL}_{m_{jj}>500}$ are the production cross sections (requiring the invariant mass of forward backward jets to be greater than 500 GeV at parton level) for the total and longitudinal polarized EW $W^+W^- jj$ productions. $\sigma^{(LL)}_{ll/lj}$ correspond to the cross sections of the dileptonic channel (ll) and the semi-leptonic channel (lj) after preselection cuts. From Ref. [189].

8.2 The network

In this section, we discuss that the network in Ref. [189] is capable of discriminating different polarization modes of the EW $W^\pm W^\mp jj$ production with the low-level inputs. We go on to discuss the application of this network to SMEFT and the 2HDM as potential LHC searches.

8.2.1 The polarization of the $W^\pm W^\mp jj$

The neural network proposed in Ref. [196] and illustrated in Fig. 8.1, can be used to effectively extract the internal connections of features. Reference [189] trained the network with labeled events with EW production of $W_L^+ W_L^- jj$, $W_L^+ W_T^- jj$, $W_T^+ W_L^- jj$, and $W_T^+ W_T^- jj$, respectively. Here W_L (W_T) represents longitudinally (transversely) polarized W boson. To assess the discriminating power of the network, the authors performed a comparative study on methods with different input variables. A three dimensional "latent" space was found to recover the original features of the leptonic and semileptonic channels with a loss of $O(10^{-4})$. In machine learning jargon, "latent" variables are the quantities that the training network uses to learn (or parameterize/fit) the training data. For a fixed training data set and learning cycles (epochs), the ability for the training network to reproduce the training data is measured by "loss." Besides the three latent features, two classes of variables are defined: experimentally accessible variables and truth-level variables that can only be obtained in Monte Carlo simulations.

The Gradient Boosting Decision Tree (GBDT) method is adopted to calculate the receiver operating characteristic (ROC) curves with inputs of the variables in a class either with or without including the latent variables. The ROC curves for the dileptonic channel are shown in Fig. 8.2(left), where one considers the events of the $W_L^+ W_L^- jj$ as the signal and events of other polarization modes as background. One can find that using latent features alone (blue line) already outperforms the GBDT with all detector-level variables (green line). For detector variables in the dileptonic channel, a signal efficiency of about 0.3 (0.8) results in a background rejection rate of about

0.9 (0.5); for the semi-leptonic channel, the rejection rates are slightly lower.

The GBDT that combines the latent variables with the detector-level variables (purple line) does not have better discriminating power than the method with solely latent variables (blue line). The GBDT with truth-level variables (orange line) has slightly improved discriminating power than the method with latent variables (blue line). It is also interesting to observe that the discriminating power can be improved further by combining truth-level variables and latent variables (red line). While employing truth-level observables is not applicable in real-life experiments, such an exercise can help estimate and quantify the performance and uncertainties of networks. Similar ROC curves for the methods with different inputs for the semileptonic channel are presented in Fig. 8.2(right). Conclusions similar to the dileptonic channel are drawn.

8.2.2 Application to EFT and 2HDM

The SMEFT contains a complete set of independent, gauge-invariant operators made up by the SM fields. Ref. [189] considered the following operator [197, 198]

$$O_H = \frac{\bar{c}_H}{2v^2}\partial^\mu[\Phi^\dagger\Phi]\partial_\mu[\Phi^\dagger\Phi] \Rightarrow \frac{\bar{c}_H}{2}\partial^\mu h\partial_\mu h \qquad (8.1)$$

since it is less constrained by the EW precision data. The Φ field is Higgs doublet and h denotes the Higgs boson field with the vacuum expectation value $v \approx 246.2$ GeV. The O_H operator contributes to the Higgs boson kinetic term, and an appropriate field redefinition is required to bring back the kinetic term to its canonical form:

$$h \rightarrow h\,[1 - \frac{1}{2}c_H]. \qquad (8.2)$$

This leads to the following changes to the Higgs couplings

$$\mathcal{L}_H \supset \frac{gm_W}{c_W^2}[1 - \frac{1}{2}\bar{c}_H]Z_\mu Z^\mu h + gm_W[1 - \frac{1}{2}\bar{c}_H]W_\mu^\dagger W^\mu h$$
$$+ [\frac{y_f}{\sqrt{2}}[1 - \frac{1}{2}\bar{c}_H]\bar{f}P_R fh + \text{H.c.}] \qquad (8.3)$$

$(m_{h_2}, \sin(\beta-\alpha))$	(300,0.7)	(300,0.9)	(700, 0.7)	(700,0.9)
$\sigma^0_{m_{jj}>500}$ [fb]	636.2	492.5	461.9	428.5
σ_{ll} [fb]	8.362	5.853	5.527	4.842
σ_{lj} [fb]	64.07	46.52	43.70	39.33
$\sigma^{LL}_{m_{jj}>500}$ [fb]	170.75	79.81	71.58	42.65
σ^{LL}_{ll} [fb]	2.91	1.27	1.30	0.676
σ^{LL}_{lj} [fb]	20.78	9.35	9.50	5.06

Table 8.3: Similar as Table 8.2, but for the 2HDM model. The corresponding parameters are given in the first row. From Ref. [189].

The updated global fit to the EFT coefficients constrains $\bar{c}_H \lesssim 0.4$ (marginalizing over all other operators) [126]. Future lepton colliders, such as the ILC, will constrain the $\bar{c}_H$ to the 1% level [199].

Here, its effects on the EW W^+W^-jj production at the LHC are summarized. The production cross section of the EW W^+W^-jj process (with different choices of $\bar{c}_H$) before and after the pre-selection are given in Table 8.2. The $\bar{c}_H = 0$ case corresponds to the SM. One can find the fraction of the longitudinal W production increases with $|\bar{c}_H|$ as cancellations among VBS amplitudes become less exact. Pre-selection cuts can raise the fraction of the longitudinal $W_L^+W_L^-jj$, especially for the dileptonic channel. After the pre-selection, the production rate of the semi-leptonic channel is an order of magnitude large than that of the dileptonic channel.

To measure the consistency of the SM and EFT with non-zero $\bar{c}_H$, a binned log-likelihood test in the latent space is performed. That is to say, the three latent variables determined from each training event (which collectively populate a three-dimensional space) are compared to the three latent variables determined from each signal event (which collectively populate a second three-dimensional space). Each collection of points makes up a shape and the two shapes are compared using a binned log-likelihood test.

The null hypothesis is the SM backgrounds plus SM EW W^+W^-jj and the test hypothesis is the SM backgrounds plus EFT EW W^+W^-jj with a non-zero $\bar{c}_H$. The required integrated luminosity to achieve 95% C.L. probing for different $\bar{c}_H$ are presented in Fig. 8.3. It can be seen that the semi-leptonic channel outperforms the dileptonic channel if the systematic uncertainty can be controlled below $\sim 5\%$. Due to higher backgrounds in the semi-leptonic channel, the sensitivity drops quickly when the systematic uncertainty is larger than 5%. With systematic uncertainty around 5%, the method will be able to constrain the $\bar{c}_H$ to [-0.2,0.1] at the HL-LHC.

The 2HDM [75, 200] is one of the simplest extension to the Higgs sector of the SM. The Type II variant was considered in Ref. [189]. There, the authors show that their method is sensitive to changes of the polarization and kinematic properties of the EW W^+W^-jj production in the 2HDM. Comparing the latent features of the W^+W^-jj process in the 2HDM with those from measurement, constraints on the parameters of the 2HDM can be obtained.

There are six parameters in the Type II 2HDM: the mass of scalars (m_{H_1}, m_{H_2}, m_A and $m_{H^\pm}$), the mixing angle between two CP-even scalars α, and the ratio between two vevs $\tan\beta$. The parameter m_{H_1} has been measured to be close to 125 GeV. The m_A and $m_{H^\pm}$ are not relevant in W^+W^-jj production. Their mass is set to 3 TeV to forbid the decays of H_2 into those states. In Table 8.3, we summarize the production cross sections of the EW W^+W^-jj process for a few points in the 2HDM for illustration.

Due to the fact that the cancellation between the amplitudes with and without Higgs exchange are delayed to the scale of m_{H_2} and the heavy scalar dominantly decays into longitudinally polarized vector boson, the fraction of $W_L^+W_L^-jj$ is considerably larger than that of the SM. For relatively light H_2 and small $\sin(\beta - \alpha)$, which means the contribution of H_2 is significant, the fraction of $W_L^+W_L^-jj$ can reach $\sim 30\%$ before applying pre-selection cuts, while the number is 6% in the SM. Pre-selection can increase the fraction even further. This feature renders the above network very sensitive to the signals in the 2HDM.

The required integrated luminosity for achieving 95% C.L. sensitivity to a particular point in the m_{H_2}-$\sin(\beta - \alpha)$ plane is shown in Fig. 8.4, for the dileptonic and semi-leptonic channels, respectively. The method of Ref. [189] proposes to probe both the resonant feature and the modification to Higgs couplings simultaneously. This is unlike traditional searches for heavy Higgs resonances [201, 202], which quickly lose sensitivity at large m_{H_2} due to the suppressed production rate. The parameter space with H_2 as heavy as 1.5 TeV can be probed with relatively low integrated luminosity provided the $\sin(\beta - \alpha)$ is not too close to one. The production cross sections of both channels before applying pre-selection cuts are indicated by the color grades in the figure. One can find the sensitivity of the method is roughly determined by the cross section, even though a slightly better sensitivity can be achieved in the small $\sin(\beta - \alpha)$ region, e.g., by comparing to the point ($m_{H_2} = 300$ GeV, $\sin(\beta - \alpha) = 0.9$). Lower integrated luminosity is required to probe the point ($m_{H_2} = 550$ GeV, $\sin(\beta - \alpha) = 0.7$), even though their production cross sections are similar. The improvement on the sensitivity is attributed to the fact that points with smaller $\sin(\beta - \alpha) = 0.7$ contains larger fractions of longitudinally polarized W bosons.

8.3 Summary

We report that Ref. [189] has constructed a neural network consisting of a classification network and an autoencoder. With the input of low level information (4-momenta and the identities of particles in this case), the network is capable of reducing the dimensionality of the feature space for W^+W^-jj production, without losing much discriminating power. This means discriminating the EW production of W^+W^-jj from other processes, as well as discriminating different polarization modes of the EW W^+W^-jj. Reference [189] finds the feature space of both dileptonic and semi-leptonic channels can be compacted into three dimensions. Performing the binned log-likelihood test on the distributions of latent features, one can draw the conclusion whether the data is consistent with the SM prediction. One finds that those latent features are sensitive to various new physics that can possibly contribute to the VBS.
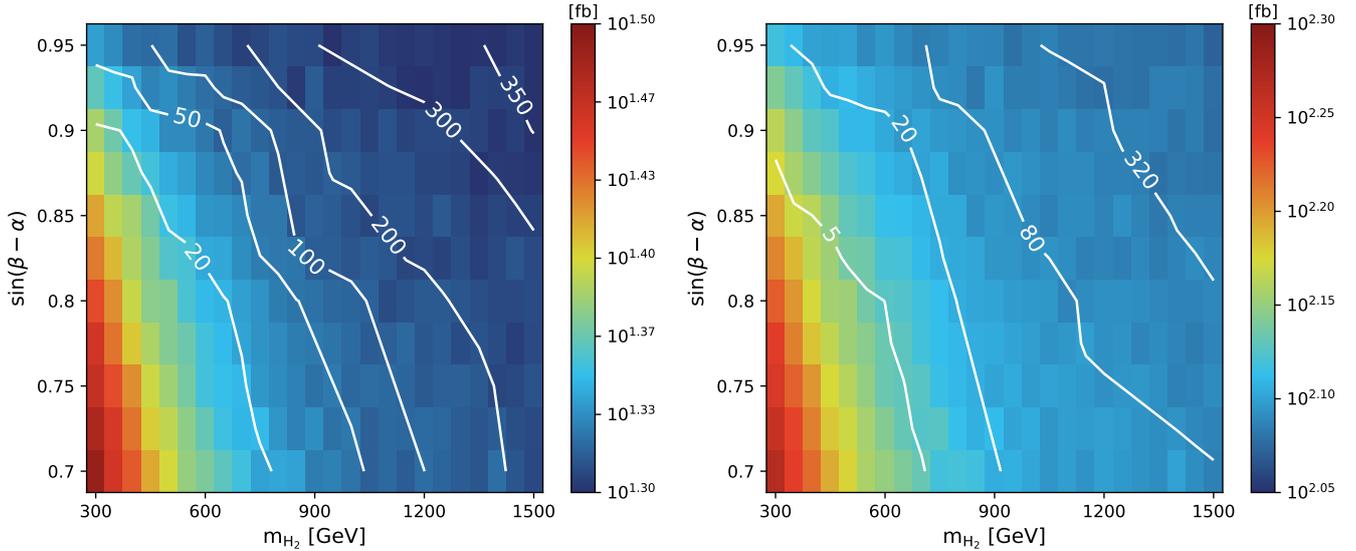
Figure 8.4: Contours corresponding to the required integrated luminosity to probe the signal (with different $\sin(\beta - \alpha)$ and m_{H_2}) at 95% C.L. Color grades correspond to the fiducial cross sections (requiring $m_{jj} > 500$ GeV at the parton level) times the branching rates. The systematic uncertainties are set to 5% for both the dileptonic channel (Left) and semi-leptonic channel (Right). Adapted from Ref. [189].
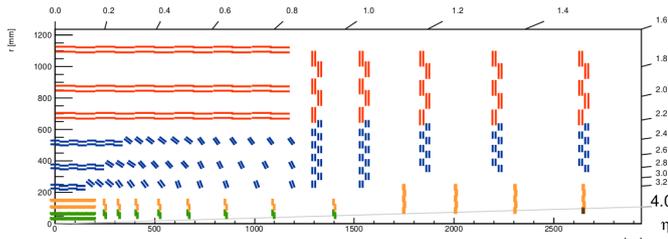
Figure 9.1: Layout of one quarter longitudinal section of the CMS Tracker for the HL-LHC. The upgraded tracking detector will extend the coverage for charged particles up to $|\eta| = 4$. In green (yellow) the silicon pixel detectors of the Inner Tracker with two (four) readout chips per module. In blue (red) the PS (2S) silicon detector modules of the Outer Tracker [203].

9   Detector & performance upgrades for the HL-LHC

After Run 3, the LHC itself will be upgraded in order to deliver a much larger data set for physics to the LHC detector experiments. The HL-LHC upgrade [206] will see the LHC operating at 5.0-7.5 times the nominal instantaneous luminosity, reaching values up to $5 \times 10^{34} \mathrm{cm}^{-2}\mathrm{s}^{-1}$ ($7.5 \times 10^{34} \mathrm{cm}^{-2}\mathrm{s}^{-1}$ in the ultimate luminosity scenario). A total delivered integrated luminosity of 3000 fb^{-1} (4000 fb^{-1}) is expected by the end of the HL-LHC operation.

The luminosity increase is experimentally challenging for both the accelerator and the detectors. With an increase in instantaneous luminosity with respect to Run 3, the ATLAS and CMS detectors need to be upgraded in order to cope with the increased radiation levels and event multiplicity. While the cur-

rent average number of pileup collisions, i.e., the number of collisions per bunch crossing, is 30-40, in the HL-LHC phase an average pileup of 140-200 collisions per bunch crossing is expected. Such pileup levels would be unsustainable for the current Phase-1 detectors and go beyond their reconstruction capabilities. Therefore, the ATLAS and CMS detectors are planned to be upgraded after Run 3 for the Phase-2 upgrade. The detector upgrades will help maintain or improve particle identification and event reconstruction in the high-pileup environment, including up to large pseudorapidities. Such upgrades will certainly benefit the reconstruction of VBS processes, which as discussed above is characterized by objects with large p_T and/or large rapidities.

In what follows, we summarize the planned detector upgrades and anticipated detector performance for the HL-LHC program. As an example, the case of the Phase-2 upgrades of the CMS detector is discussed [203] . A comparable upgrade program and outlook for detector and physics performance are anticipated for ATLAS [207].

9.1   Current CMS tracker in HL-LHC environment

The current Phase-1 tracker is designed to sustain an instantaneous luminosity of $1 \times 10^{34}\mathrm{cm}^{-2}\mathrm{s}^{-1}$. Simulations show that the tracker is expected to start degrading at 500 fb^{-1} [203], with spatial resolution decreasing due to decreased charged sharing between neighboring pixels. The HL-LHC radiation levels would cause the increase of the depletion voltage as well as the leakage current, compromising the functioning of many tracking modules.

9.2   Phase-2 tracker upgrade

The Phase-2 tracker is designed to withstand >3000 fb^{-1} and increased radiation levels. In order to cope with the in-
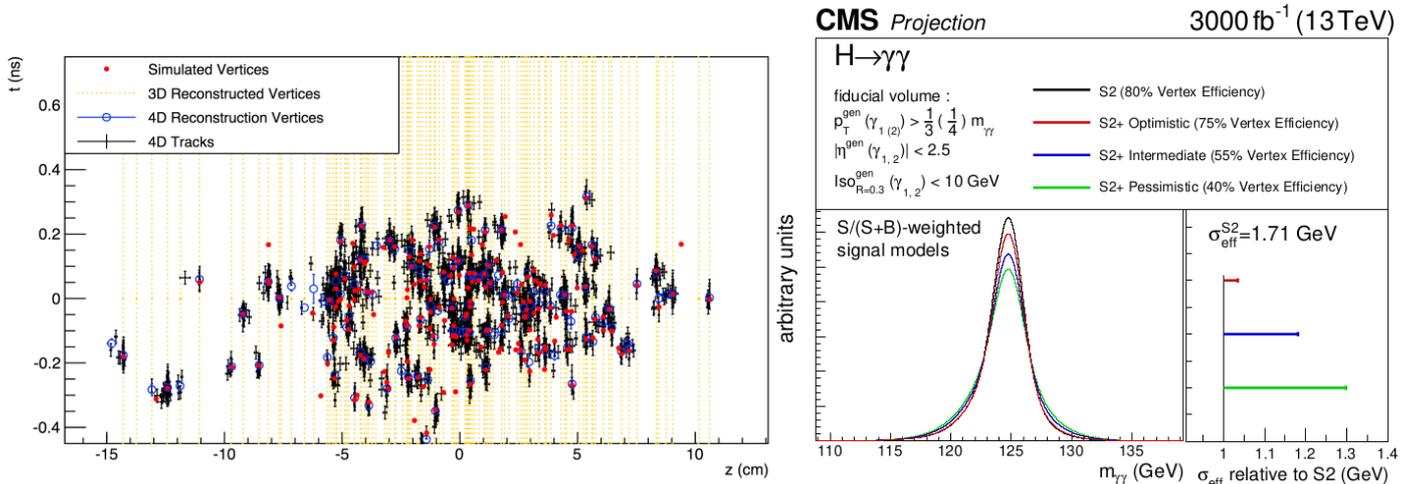
Figure 9.2: Left: Proton-proton interaction vertices: time versus longitudinal coordinate. Simulated and reconstructed vertices in a 200 pileup event assuming a MIP timing detector covering the barrel and the endcaps. Right: H $\longrightarrow \gamma\gamma$ mass resolution under different vertex reconstruction efficiency scenarios. Plots from Refs. [204, 205].

creased L1 trigger rate of 750 kHz, the tracking information needs to be provided to the L1 trigger. The new Tracker is composed of the Inner and Outer trackers.

The Outer Tracker (OT) design is driven by the new trigger demands. The modules are composed of two single-sided, closely-spaced silicon strip sensors read out by a common set of front-end ASICs that correlate the signals in the two sensors providing a local transverse momentum (p_T) measurement. "Hit" pairs are selected to be compatible with particles above the chosen p_T threshold (2 GeV). The OT modules are placed in a tilted geometry in order to keep the tracking efficiency high also for large η tracks.

The Inner Tracker (IT) is composed of pixel sensors with a narrower pitch than Phase-1 tracker, with a pixel size of 25 $\times$ 100 μm^2 or 50 $\times$ 50 μm^2, and are expected to exhibit the required radiation tolerance and two-track separation capability. The new electronics is highly segmented with 1$\times$2 and 2$\times$2 readout chips. The addition of tracking modules in the forward region extends the tracking coverage up to $|\eta| = 4$, as shown in Fig. 9.1 [208].

9.3 Phase-2 tracker performance

Simulations of the Phase-2 tracker [209] show that a high tracking efficiency is maintained over the full η coverage for 10 GeV muons and $t\bar{t}$ events (p_T >0.9 GeV), with efficiencies ranging around 95-100% in the first case, and 85-95% in the latter. The level of mis-identification ("fake") rates is expected to be smaller than 4% for $t\bar{t}$ events, even in the ultimate pileup conditions (200 simultaneous collisions). The estimated p_T and impact parameter (d_0) resolutions are also expected to improve with respect to the Phase-1 tracker, and b-tagging can be extended up to $|\eta|$=3.5. The new tracker will feature a substantial reduction in material budget in terms of radiation lengths, thus reducing the inactive material within the tracking volume.

9.4 MTD: A new precise timing detector

A precise timing detector will bring a completely new capability to CMS: the ability to measure precisely the production time of minimum ionizing particles (MIP) to disentangle the approximately 200 nearly simultaneous pileup interactions that will occur in each bunch crossing. The MIP Timing Detector (MTD) is a new detector, placed outside of the tracker and inside the calorimeter, planned for the CMS experiment during the HL-LHC era. The MTD will aim at providing a time resolution of about 30-50 ps over the period of operation at the HL-LHC. It will also provide new capabilities for charged hadron identification and to the search for long-lived particles.

The timing upgrade of the CMS detector will mitigate the high pileup HL-LHC environment and improve the performance to a level comparable to the Phase-1 CMS detector, exploiting the additional information provided by the precision timing of both tracks and energy deposits in the calorimeters. The event display in Fig. 9.2 (left) shows the power of space-time 4-dimension event reconstruction in 200 pileup collisions. The time information is essential to distinguish vertices spread along the beam axis. Figure 9.2 (right) shows the Higgs boson diphoton mass peak for different vertex reconstruction efficiencies. An efficiency of 80% was achieved in Phase-1, while only 40% is expected for Phase-2 if no timing information is provided; the other two cases include different degrees of precision timing. Based on different technologies, the MTD is divided into a barrel (LYSO scintillator coupled to silicon photomultipliers, $|\eta| < 1.5$) and two endcap sections (silicon detectors, Low Gain Avalanche Diodes (LGADs)) covering up to $|\eta| = 3.0$. Details can be found in Refs. [204, 205].

9.5 The calorimeters: ECAL and HCAL

The electromagnetic and hadronic calorimeters (ECAL and HCAL, respectively) responses need to be calibrated throughout data taking. In fact, the scintillators are degraded by radiation and their response progressively decreases. Figure 9.3
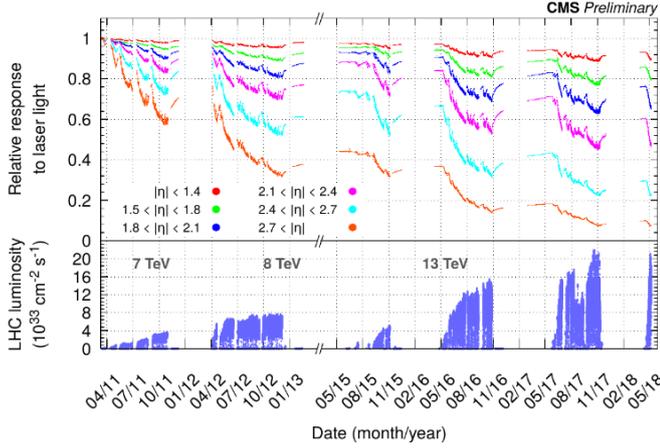
Figure 9.3: Upper panel: relative ECAL response as a function of time at different η regions as monitored by laser calibrations since 2011. Lower panel: corresponding LHC luminosity. From Ref. [212].

Figure 9.4: Schematic drawing of the CMS HGCAL design [165].

shows the ECAL crystal response to laser light during Run 1 and Run 2. The crystals in the forward region of the detector are the most affected by radiation, with the response reduced to less than 20% its nominal value at the end of Run 2. The studies suggest that the barrel ECAL and HCAL can survive up to a luminosity of 3000 fb^{-1}, while the endcaps need to be replaced before the HL-LHC. Details can be found in Ref. [210].

9.6 Phase-2 ECAL upgrade

The current crystal geometry of ECAL is maintained throughout Phase-2, while the front-end and readout electronics are replaced to cope with trigger requirements. Single-crystal information is made available to L1 triggers, instead of the previous standard of 5×5 crystal towers. Faster readout electronics allow discrimination between an electromagnetic (EM) shower signal and anomalous spikes in Avalanche Photodiodes (APDs), this latter originated by the dark current. A discrimination on the different signal shape is employed to retain EM shower signals only.

Projections show that the transparency loss of crystals at 3000 fb^{-1} will be limited to 50% of the end of Phase-1 value [210], therefore the current lead tungstate (PbWO$_4$) crystals may be kept until the end of the HL-LHC phase. The increased radiation level causes the increase of dark current in the APDs. However, the dark current can be kept under control by further cooling down the detector to 9°C.

The new electronics will allow CMS ECAL detector to reach a precise time resolution (~30 ps) of the signal in the APDs, which is essential to distinguish the interaction vertices in an extreme pileup scenario. Beam tests with electrons show that a resolution below 2% is achievable, down to 1% for a cluster energy larger than 50 GeV [211].

9.7 High-Granularity Calorimeter (HGCAL)

The existing forward calorimeters will be replaced by a new High-Granularity Calorimeter (HGCAL) [165], providing a unique fine grain in view of a multi-dimensional shower reconstruction up to a pseudorapidity $|\eta| = 3.0$.
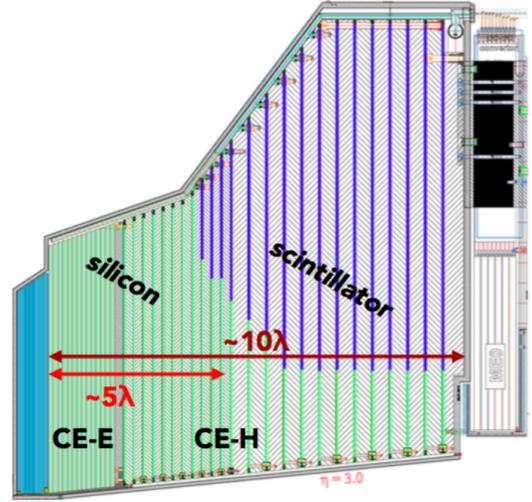
The HGCAL consists of a sampling calorimeter with silicon and scintillators as active material, including both electromagnetic (EE) and hadronic (FH+BH) sections. A schematic view is shown in Fig. 9.4. The active elements are 320 μm-thick silicon sensors. The detector is transversely segmented into hexagon cells of about 1 cm^2 surface, for a total of over 6 million channels. Plastic scintillator tiles are used in the outermost regions of FH and BH, alternated with stainless steel absorbers. The thickness of the EE part amounts to about 25X_0 and about 1λ. The thickness of the hadronic part corresponds to about 3.5λ and 5.7λ for the FH and BH, respectively, for a total of about 9λ for the 24 layers. The whole system needs to be kept at -30°C in order to function.

9.8 HGCAL performance

The expected performance of HGCAL were first evaluated with a standalone GEANT4 simulation. Figure 9.5 shows the electron energy resolution as a function of the electron energy for various active thickness of the silicon sensors. The stochastic term ranges from 20 to 24% but the constant term is targeted to be low (1%) [213]. The time resolution of HGCAL is expected to be 30 ps for clusters with p_T >5 GeV. The timing performance combined with the high granularity of this detector allow to use it as an imaging calorimeter.

9.9 Muon detector upgrade

The muon detector electronics will be replaced to cope with increased radiation and meet trigger/readout latency requirements. Performance in the forward region will be enhanced by adding a resistive plate chamber and gas electron multiplier (GEM) chambers in the forward region to improve efficiency, fake rejection, and resolution in the region 1.6 < η < 2.4. A new GEM chamber (ME0) will finally extend the coverage up
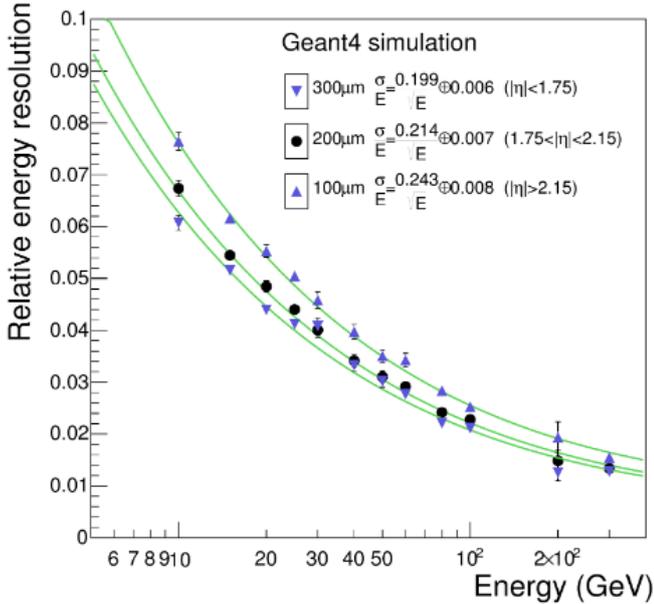
Figure 9.5: Energy resolution as a function of energy from a standalone simulation of incident electrons on HGCAL, for different thickness of silicon sensors [203].

to $|\eta|$=2.8, adding a muon trigger signal in the very forward region [214].

9.10 Summary

In the HL-LHC era, a new tracking detector will increase the overall acceptance of CMS up to $|\eta|$=4 and, for the first time, tracking information will be provided to the L1 trigger. CMS will include a new electromagnetic and hadronic endcap calorimeter with high granularity. The Phase-1 ECAL crystals are maintained during the HL-LHC phase while the front-end electronics are replaced, allowing for precise timing of signals. The muon detector coverage is extended to match the extended tracker. More broadly, simulations and beam tests suggest that both ATLAS and CMS will at least maintain the current performance in the high-pileup environment, or even improve in certain aspects, *e.g.*, object reconstruction, particle identification, and background rejection.

Part IV
VBS at future colliders

As the HL-LHC program will conclude in the late 2030s or early 2040s, the community has turned to discussing opportunities for a successor to the LHC [16, 17]. Presently, several colliders are being discussed. This includes: circular and linear e^+e^- colliders with center-of-mass energies at or below a couple TeV, $\mu^+\mu^-$ colliders with energies at a few TeV, more energetic proton colliders with energies reaching up to 100s of TeV, as well as others.

The international particle physics community has developed a plan [16, 17] and the top priority is the construction of an e^+e^- collider to study the Higgs and other less-known parameters of the SM. For these facilities, the required technology is mature. Other collider scenarios are possible, and are certainly great leaps forward in terms of knowledge and the energy frontier, but are farther away due to technological obstacles. Interestingly, at the electron, muon, and proton machines presently under discussion, the VBS process manifests differently. In all cases, VBS remains a powerful tool to exploring the EW sector and beyond.

Part IV continues by first discussing VBS at electron colliders (Section 10), and then EW parton distribution functions (Section 11) and EW parton showers (Section 12), both of which are intimately related to VBS at ultra high-energy colliders. It continues with VBS studies of SMEFT (Section 13) and BSM scenarios (Section 14) at multi-TeV muon colliders, and finally, VBS at a 100 TeV proton collider (Section 15) is discussed. We note that discussions here are only representative of a rich body of literature.

10 VBS at e^+e^- colliders

As described above, the 2020 Update for the European Strategy of Particle Physics has designated an e^-e^+ Higgs factory as one of the highest priorities of the high energy physics community, particularly as a staging platform to an even higher energy hadron collider [16, 17]. There are four proposals for such a next-generation machine: two circular variants, the CEPC [215] and the FCC-ee [216], and two linear variants, the ILC [217, 218] and CLIC [219, 220]. While the circular options can cover measurements at the Z pole as well as the W^+W^-, ZH, and $t\bar{t}$ thresholds with ultra-high integrated luminosity, only the linear machines can be extended into energy regions which are relevant for VBF and scattering measurements. Therefore, we focus here on the last two options. A fifth proposal, a many-TeV $\mu^+\mu^-$ collider, is discussed in Sections 11, 13, and 14, .

Roughly speaking, VBS becomes interesting at lepton collider energies of $\sqrt{s}$ = 500 GeV and beyond. The benefit of VBS studies at an electron-positron collider is the well-defined, quasi-partonic initial-state emission of EW bosons, where the dominating theoretical uncertainties are under better control. There are well-defined, well-separated and clean events that allow for a triggerless operation, full coverage of final states, and high-precision measurements. Spin, isospin, and CP quantum numbers of SM particles can be resolved with high precision due to excellent particle identification using particle-flow techniques. Due to the low hadronic environment, electron-positron colliders naturally have discriminating power for light quark flavors in jets, *i.e.*, for charm and potentially even for strange quarks.

The ILC project is in a mature state, entering the so-called "prelab" phase in 2022 [221], prepared itself by the international development team, whose main deliverable is the engineering design report (EDR) of the machine. The machine is based on superconducting radiofrequency (RF) cavities with a

design gradient of 31.5 MV/m, hosted in a 20.5 km long tunnel in the Kitakami region of the Iwate prefecture in northern Japan. The tunnel is extendable to 30 km and beyond, such that the machine can be upgraded based on the superconducting RF technology within the given infrastructure to 1 TeV or even a little higher. The energy range is tunable, which allows measurements at different energy stages. Such features are interesting, for example, for constraining or measuring EFT parameters at different energies. On the other hand, CLIC is based on normal conducting RF cavities using a drive beam concept which allows to reach 100 MV/m. There are three different energy stages foreseen, 380 GeV, 1.5 TeV, and 3 TeV.

Another important asset of linear e^+e^- colliders is the possibility of polarized beams. These help enhance event yields for specific signal processes. The ILC and CLIC both foresee 80% electron polarization. While CLIC considers unpolarized positron beams, the ILC baseline design uses rotating targets and undulators to generate 30% positron polarization. This rate is expected to deteriorate to 20% at the 1 TeV stage. The staged running foresees large data samples for ILC and CLIC at the highest energies: $\mathcal{L} = 1.5$ (5) ab^{-1} for $\sqrt{s} = 1.5$ (3) TeV for CLIC, and $\mathcal{L} = 4$ (8) ab^{-1} for $\sqrt{s} = 500$ (1000) GeV for the ILC.

In comparison to proton colliders, the main topology of VBS processes remains unchanged at e^+e^- colliders. At high energies, the VBS signature is characterized by high-p_T activity that is accompanied by two forward partons. These forward partons are either neutrinos when VBS involves $W^\pm$ scattering, or charged leptons when involving Z/γ scattering. In order to accept forward charged leptons or to veto them, a very good, low-angle coverage by the ILC and CLIC detectors is crucial. This is achieved by using the luminosity and beam calorimeters (LumiCal and BeamCal), which have coverage down to 38-110 mrad (LumiCal) and 15-38 mrad (BeamCal), respectively. Hence, they allow one to go down to rapidities as low as $|\eta| \approx 4.9$ in the forward direction [222]. Another asset of electron-positron colliders is the possibility to perform VBS measurements with fully hadronic final states of the EW vector bosons $W^\pm, Z$. This is achieved using the particle flow algorithm as it was shown for the CLIC detector [223]. This allows a hadronic W/Z discrimination with an efficiency of 88%, as the particle flow algorithm almost completely removes the photon-induced hadron background for energy ranges between 100 and 1200 GeV. The efficiency is slightly reduced to 71-79% when considering the photon-induced background in the high-energy regime of CLIC.

10.1 Anatomy of W^+W^- scattering at e^+e^- colliders

While at hadron colliders the EW diboson production with additional QCD radiation constitutes the largest background contamination for VBS processes, at e^+e^- colliders the dominant background is from EW radiation and other resonant EW production processes. Figure 10.1 shows examples of Feynman diagrams for $W^+W^- \rightarrow W^+W^-$ scattering and its backgrounds at e^+e^- colliders: In the top row there are the signal diagrams for $W^+W^- \rightarrow W^+W^-$ containing triple and quartic gauge vertices and Higgs exchange. The middle row shows the reducible
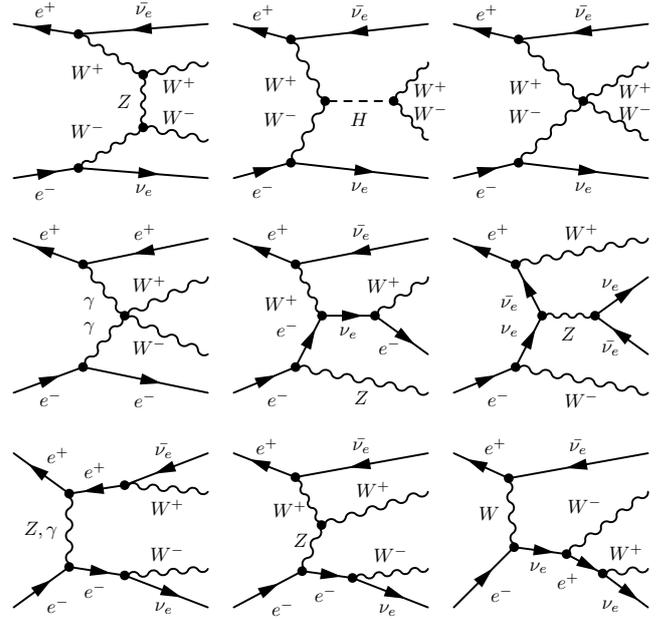
Figure 10.1: Topologies for W^+W^- scattering processes at e^+e^- colliders: signal diagrams (top row), reducible background diagrams (middle row), and irreducible diagrams (bottom row), respectively.

background from photon fusion as well as from triple boson production and multi-peripheral diagrams. The bottom row finally shows the irreducible background diagrams, mostly from EW radiation. Here, the term "reducible" backgrounds refers to backgrounds with characteristic final states, topologies, or kinematics that can facilitate their removal with selection cuts and other analysis-level requirements. "Irreducible" backgrounds are those that survive such selection cuts and requirements on final-state particles. Note that diagrams with initial- and final-state EW radiation can be enhanced by large EW logarithms; however, this regimes just begins in the multi-TeV range. Similar classes and types of diagrams to those in Fig. 10.1 are present for other VBS processes in high-energy lepton collisions.

There is quite some literature on the study of VBS at electron (-positron) colliders, which started with the first interests in linear colliders in the late 1980s [225, 226, 227]. There were also quite some publications triggered by the TESLA preparations [228, 229, 230, 231]. Among those were the ones first pointing out the interplay and gauge dependence between VBS and triple boson diagrams. At this time the EW corrections to (on-shell) VBS had been calculated [232, 233]. Later on, the leading logarithmic corrections for the off-shell process were calculated [98]. Also off-shell effects for Higgs processes in VBS have been studied [234]. Many studies were devoted to the question whether a strongly coupled EW sector could be discovered in VBS at an e^+e^- collider [235, 236, 237, 238, 239]. Within these, some studies were also made for same-sign e^-e^- colliders in order to access same-sign WW scattering.

In the following, we will describe the technical details how

Process ($e^+e^- \to X$)	$\sigma_{1.4\,\text{TeV}}$	$\sigma_{3\,\text{TeV}}$	Mis-ID Factor
Signal and background for $VV \to W^+W^-$			
$W^+W^-\nu\bar{\nu}$	0.119	0.790	1
$W^+W^-e^+e^-$	< 1 ab	< 1 ab	1
$W^\pm Z e^\mp \nu$	0.269	1.200	0.136
ZZe^+e^-	< 1 ab	< 1 ab	0.019
$W^+W^-(Z \to \nu\bar{\nu})$	0.039	0.610	1
Signal and background for $VV \to ZZ$			
$ZZ\nu\bar{\nu}$	0.084	0.790	1
ZZe^+e^-	< 1 ab	< 1 ab	1
$W^\pm Z e^\mp \nu$	0.288	1.590	0.136
$W^+W^-e^+e^-$	< 1 ab	< 1 ab	0.019
$ZZ(Z \to \nu\bar{\nu})$	< 1 ab	< 1 ab	1

Table 10.1: SM cross sections in fb ($\pm 1\%$ error) of signal and background processes for $VV \to W^+W^-$ (upper) and $VV \to ZZ$ (lower) scattering, with selection cuts for the fully hadronic final state in e^+e^- collisions at $\sqrt{s} = 1.4$ TeV and 3 TeV. Both particle beams are unpolarized. Detection efficiencies and branching ratios are not included. All cross sections have to be multiplied by the factors in the fourth column to take the misidentification of vector bosons into account. For further details, see Ref. [224].

to extract the VBS signal at a lepton collider from the EW background and the subtleties in how to look for deviations from the SM. The first, rather complete assessment of all backgrounds to VBS and triple boson production has been made in [239], for 1 TeV, assuming 40% positron polarization. The main processes are $e^+e^- \to \nu\bar{\nu}q\bar{q}q\bar{q}$, which contains the signal subprocesses $W^+W^- \to W^+W^-, ZZ$ as well as the triple-boson production $V \to VVV$. The process $e^+e^- \to \nu e q\bar{q}q\bar{q}$ consists of the signal subprocess $WZ \to WZ$, and the process $e^+e^- \to e^+e^- q\bar{q}q\bar{q}$ contains the subprocess $ZZ \to W^+W^-, ZZ$. Cross sections range between a few fb up to 130 fb for the $\nu e jjjj$ final state. The last three processes are also populated by radiative Bhabha events. Six-(and eight-) fermion final states are contaminated by top pair production and ttH, which peaks at around 800 GeV center-of-mass energy. The largest individual background is from four-jet processes by diboson production (and additional QCD radiation) which reaches up to almost 4 pb. Further backgrounds come from single-W production, i.e., $e^+e^- \to e\nu q\bar{q}$, and radiative Z production, $e^+e^- \to e^+e^- Z$. Another substantial background comes from di- and multi-jets which amounts to 1.6 pb.

These older studies have been revisited in Ref. [224]. Table 10.1, using the simulation framework of [240, 241], shows the total cross sections for two different high-energy stages of CLIC at $\sqrt{s} = 1.4$ and 3 TeV for on-shell vector boson production. In this table SM cross sections in fb ($\pm 1\%$ error) of signal and background processes for $VV \to W^+W^-$ (upper) and $VV \to ZZ$ (lower) scattering, with selection cuts for the fully hadronic final states. Selection cuts include: requiring that reconstructed W/Z bosons are central through polar angle and p_T cuts; requiring that the (WW)- or (ZZ)-system carry a large
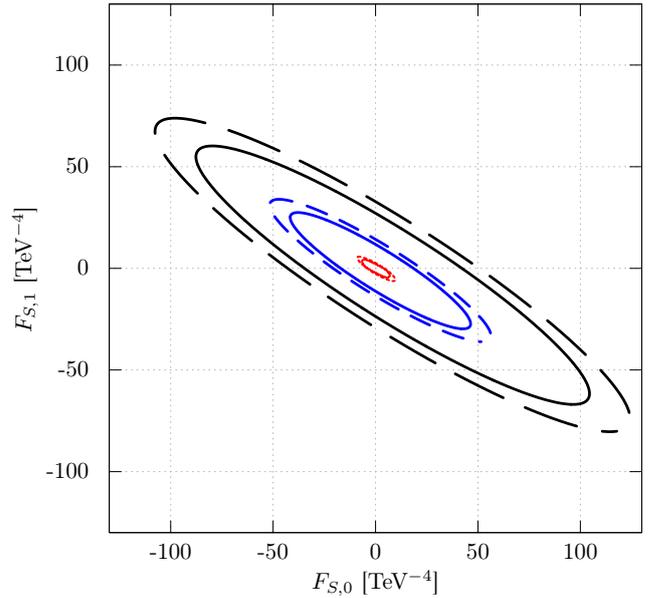
Figure 10.2: The 90 % exclusion sensitivities for polarized (solid) and unpolarized (dashed) particle beams at energies of $\sqrt{s} = 1$ (black), 1.4 (blue), 3 TeV (red) combined, assuming integrated luminosities of 5 ab^{-1} at $\sqrt{s} = 1$ TeV, 1.5 ab^{-1} at $\sqrt{s} = 1.4$ TeV, and 2 ab^{-1} at $\sqrt{s} = 4$ TeV. Adapted from Ref. [224].

invariant mass and large transverse momentum; and requiring final-state leptons be central or carry a large invariant mass. For more specifics, see Ref. [224]. The last column of Table 10.1 is the correction factor due to the mis-identification efficiency for hadronic decays of vector bosons. It takes into account a probability for mis-identification between W and Z bosons, and has to be taken into account experimentally. It is apparent that the signal cross sections rise significantly from 1.4 to 3 TeV. The contamination from WZ scattering is particularly noteworthy. Also note that the background from triboson production is irreducible as VBS and triboson production are in the same class of EW gauge-invariant processes.

One possibility to enhance the VBS component is by a selection cut on the fiducial phase space. The following cuts can be used to reduce the different backgrounds, which are adapted in their numerical values to the different energy stages of ILC and CLIC: (1) Backgrounds from $Z \to \nu\bar{\nu}$, W^+W^- diboson production, and the QCD 4-jet continuum can be significantly reduced by an invariant mass cut on the neutrino/invisible system, $M_{inv}(\nu\bar{\nu})$; (2) Backgrounds from t-channel, multi-peripheral subprocesses in the production can be reduced by cuts on the transverse momentum of single EW bosons, $p_{\perp,W/Z}$, and simultaneously on the (beam) angle of the EW boson, $\cos\theta(W/Z)$; (3) Photon-induced backgrounds from the effective photon approximation (EPA)/ISR-like setups can be suppressed by transverse momentum cuts on the diboson systems, $p_\perp(WW, ZZ)$, respectively; furthermore, very effective suppression is reached
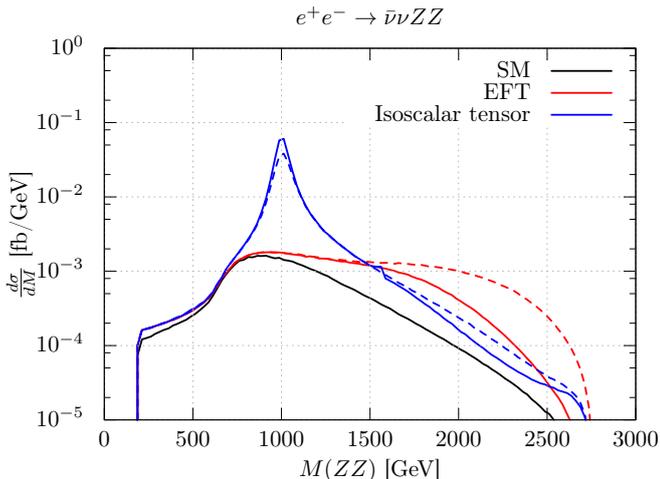
Figure 10.3: Differential cross sections depending on the invariant mass of the ZZ system in $e^+e^- \to ZZ\nu\bar{\nu}$ at $\sqrt{s} = 3$ TeV. The solid lines show the signal process $\bar{\nu}\nu ZZ$ with SM values $F_{S,0} = F_{S,1} = 0$. The red lines show matched EFT results with $F_{S,0} = 150.8$ TeV $^{-4}$ and $F_{S,1} = -50.3$ TeV $^{-4}$. The blue lines show an isoscalar tensor resonance f with $m_f = 1$ TeV, $F_f = 17.4$ TeV $^{-1}$, and $\Gamma_f = 100$ GeV. (Dashed lines: naive EFT results, solid lines: unitarized results). Adapted from Ref. [224].

by vetoing visible forward electrons $\theta(e) > 15$ mrad; (4) Finally, massive EW radiation can be eliminated selecting certain (high-energy) windows of the diboson-system invariant masses, $M_{inv}(WW, ZZ)$, respectively. For details, see Ref. [224].

10.2 Constraining New Physics in VBS at e^+e^- colliders

VBS is one of the tools to look for deviations from the SM in the EW sector. In a modern framework after the Higgs discovery, deviations are described in terms of higher-dimensional operators. To derive constraints on these operators or finding a significant deviation of experimental data from the SM by non-zero Wilson coefficients is the main task of these measurements.

There are several stages of describing new physics beyond the SM, as it was discussed in detail for VBS in [25]: (1) in terms of an effective field theory expansion, (2) by a simplified model with generic new resonances, and (3) specific BSM models. In [224] the sensitivity of ILC-1.0, CLIC-1.5 and CLIC-3.0 have been derived for dimension-eight operators in the SMEFT framework, shown in Fig. 10.2. These results take into account a signal model that always stays within the unitarity bounds of the amplitudes [242, 243]. There have been also studies on simplified models comprising resonances that couple dominantly to the EW diboson systems, such that their production via Drell-Yan processes are too faint [224] (resonances coupling to transverse modes had been introduced in [244], for LHC). This framework can be mapped in a leading-order power expansion to the standard SMEFT operators. An example is shown for an isoscalar spin-2 resonance in Fig. 10.3. For more details, see Ref. [224].

In summary, these studies show that the clean environment of an electron-positron collider at highest energies is a fantastic opportunity for searches for new physics in the EW sector. In general, the reach is much enhanced by being able to go to the highest-available energies – there are proposals for plasma-wakefield driven accelerators that could reach tens of TeV – while polarization of at least the electron beam is desirable in order to reduce backgrounds to provide discriminating analysis power for the effects of new physics. This applies both to polarization measurements as well as to the resolution of CP quantum numbers.

11 EW parton distribution functions

The discovery of the Higgs boson at the LHC [245, 246] symbolizes a great triumph of the SM, and understanding the properties of the Higgs remains the community's top priority. The next targets on the particle physics road map [16, 17] require reaching a new energy frontier. This can be achieved by building new colliders with partonic center-of-mass energies that are well beyond $O(1)$ TeV.

There are several pathways to reach such energies. For example: recently, breakthroughs in the cooling technology for a muon beam provides a potential pathway to construct a $\mu^+\mu^-$ collider with a collision energy up to $\sqrt{s} \sim O(10)$ TeV [247]. A future 100 TeV proton-proton collider, such as the FCC-hh promoted by CERN [248] or the SppC promoted by IHEP [249], and which can readily reach $O(10)$ TeV partonic collisions, is another appealing option to push the energy frontier up to an unprecedented level.

Regardless of the specific collider, at collision energies well above the EW scale $\mu_{EW} \approx M_Z$, all SM particles are essentially massless and the SM gauge symmetry $SU(2) \otimes U(1)_Y$ is approximately restored [250]. In analogy to quark/gluon splitting in hadron collisions, the collinear splitting mechanism involving the EW bosons becomes a dominant phenomenon in this kinematic regime. For initial-state radiation, the EW parton distribution function (PDF) formalism should be adopted as a proper description, which resums potentially large collinear logarithms [251, 252, 253, 254]. Similarly, final-state EW radiation and associated logarithms should be resummed by fragmentation functions [255], or equivalently by the Sudakov form factor implemented in the parton showering [250] (see also Section 12 for related details). From this perspective, one can think of VBS as being initiated by a pair of initial-state EW bosons instead of a pair of initial-state leptons or quarks (and intermediate EW bosons).

In this section, we present results of recent work [253, 254] on EW PDFs and their corresponding application to high-energy lepton colliders. In Section 11.1, we lay out the EW PDF formalism up to double-log accuracy, and present some numerical results. Application to representative SM processes at a multi-TeV muon collider is discussed in Section 11.2. We summarize and conclude in Section 11.3. This formalism is equally applicable for an e^+e^- collider, with an enhancement by a factor of
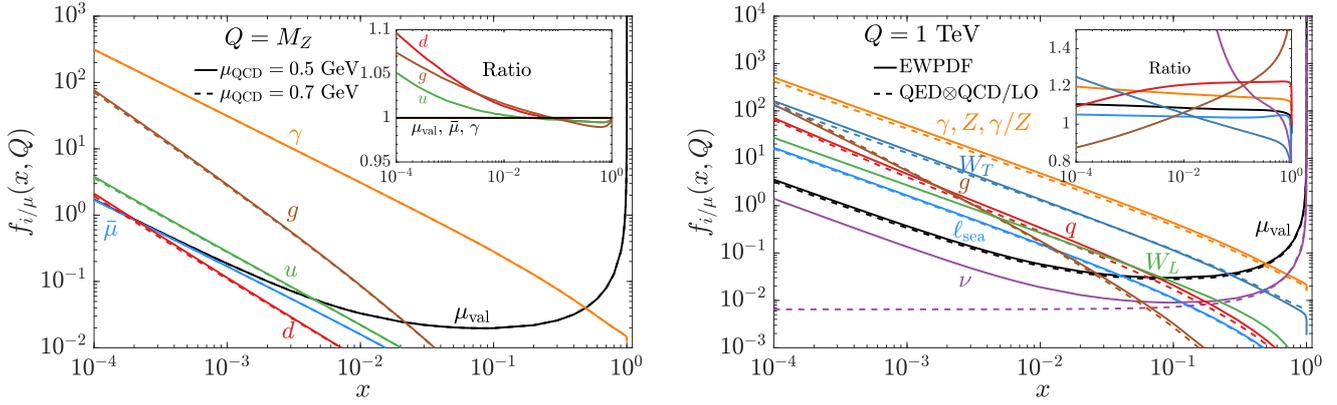
Figure 11.1: PDFs of a muon at $Q = M_Z$ (Left) and 1 TeV (Right). Left: The solid (dashed) lines correspond to the PDFs with matching scale $\mu_{\text{QCD}} = 0.5$ (0.7) GeV. Right: The solid lines indicate the complete EW PDFs, while the dashed lines are the pure QED⊗QCD evolution for $\gamma, \ell_{\text{sea}}, q, g$ and the LO splittings for ν, W, respectively. Inset: the ratios of the solid to dashed lines with the same colors.

$\log\left(m_\mu^2/m_e^2\right)$. It is also straightforward to extend this formalism to high-energy hadron colliders, which is left for a future work.

11.1 The electroweak parton distribution functions

Parton distribution functions $f_i(x, Q)$ evolve according to the well-known DGLAP equations [256, 257, 258, 259]

$$\frac{\mathrm{d}f_i}{\mathrm{d}\log Q^2} = \sum_I \frac{\alpha_I}{2\pi} \sum_j P_{i,j}^I \otimes f_j, \qquad (11.1)$$

where I runs over the SM gauge and Yukawa interactions, and the indices i, j run over all particle species. (In principle, the evolution for particles of different chiralities are different. However, this notation is suppressed here for clarity.) In the above expression, Q is the evolution scale, $\alpha_I(\mu_r = Q)$ is the renormalized coupling of gauge interaction I, and $P_{i,j}^I$ is the $j \to i$ splitting function under I. The operator $\otimes$ denotes the usual convolution over momentum fractions x. The full SM spectrum is characterized by two scales, $\Lambda_{\text{QCD}} \sim 200$ MeV and $\Lambda_{\text{EW}} \sim 250$ GeV. To validate the QCD perturbativity, we adopt a matching scale μ_{QCD} to separate the pure QED region at low energy from the QED⊗QCD region at an intermediate scale. Below μ_{QCD}, only photon and light charged fermions are active through the electromagnetic interactions. Above μ_{QCD}, the QCD interaction enters, and the gluon becomes an active parton content as well. In this approach, the non-perturbative effect is parameterized with this threshold variable μ_{QCD}, which in principle should be determined through data or lattice simulation. In practice, we take $\mu_{\text{QCD}} = 0.5$ GeV, inspired by the critical scale in Ref. [260]. Its variation quantifies the corresponding QCD threshold uncertainty.

Below the EW scale $Q^2 \ll \mu_{\text{EW}}^2$, the effects of the massive EW gauge bosons are suppressed by $g^2 Q^2/M_Z^2$ and the corresponding partons are inactive. Above the EW scale, all the EW states are activated and evolve according to the unbroken SM gauge group. It is more convenient to work in the gauge basis

with the EW partons $B, W^{\pm,3}$. At the EW scale μ_{EW}, a matching condition bridges the PDFs in the QED⊗QCD to EW regions with a general relation

$$\begin{pmatrix} f_B \\ f_{W^3} \\ f_{BW^3} \end{pmatrix} = \begin{pmatrix} c_W^2 & s_W^2 & -c_W s_W \\ s_W^2 & c_W^2 & c_W s_W \\ 2c_W s_W & -2c_W s_W & c_W^2 - s_W^2 \end{pmatrix} \begin{pmatrix} f_\gamma \\ f_Z \\ f_{\gamma Z} \end{pmatrix}, \qquad (11.2)$$

where $s_W = \sin\theta_W$ is the sine of the weak mixing angle and

$$f_\gamma(x, M_Z) \neq 0, \ f_Z(x, M_Z) = 0, \ f_{\gamma Z}(x, M_Z) = 0. \qquad (11.3)$$

The mixed PDF $f_{\gamma Z}$ (or f_{BW^3}) represents the coherently mixed state, resulted from the interference between the γ, Z (or B, W^3) [250, 251, 261].

As the QCD/EW partonic formalism is set up, the PDFs of a leptonic beam are fully calculable in a perturbative framework. For a momentum fraction x and factorization scale μ_f, the initial conditions start from the lepton mass m_ℓ at the leading order as

$$f_{\ell/\ell}(x, \mu_f = m_\ell) = \delta(1 - x), \qquad (11.4)$$

while all other partons are zero at the initialization scale $Q_0^2 = m_\ell^2$. We solve the DGLAP equations and obtain PDFs for a high-energy muon beam, with two typical scales $Q = M_Z$ and 1 TeV shown in Fig. 11.1. The PDFs at some other scales and the corresponding parton luminosities for muon colliders at various energies can be found in Refs. [253, 254]. Many important features for the light-flavor PDFs are discussed in Ref. [254] and the EW PDFs in Refs. [253]. Here, we want to emphasize the threshold uncertainty estimated by varying the matching scale as $\mu_{\text{QCD}} = 0.7$ GeV [260]. The overall size is a few percent for quark and gluon PDFs. Compared to up-type PDFs, the relative variation of the down-type PDFs is larger, because the corresponding absolute PDFs are smaller resulted from the smaller electromagnetic charges. For an electron beam, the μ_{QCD} uncertainty is expected to be larger due to the larger logarithm $\log\left(\mu_{\text{QCD}}^2/m_\ell^2\right)$ [254]. The impact on the lepton and photon PDFs is negligible, as the QCD interactions only enter as a higher-order effect.

34
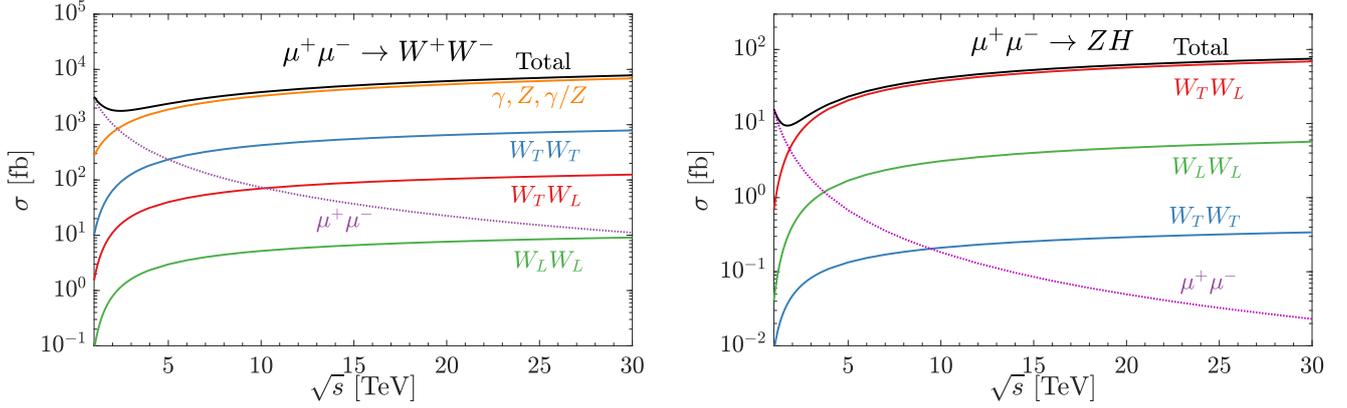
Figure 11.2: The semi-inclusive cross sections of the W^+W^- (Left) and ZH (Right) production and the corresponding decomposition channels at high-energy muon colliders with collision energy from 1 to 30 TeV.

In Fig. 11.1(right), the complete EW PDFs at $Q = 1$ TeV are shown as solid curves. The sea-flavor fermions can be expressed in terms of valence-flavor (val) fermions and are given by the summations

$$f_{\ell_{\text{sea}}} = f_{\bar{\ell}_{\text{val}}} + \sum_{i \neq \ell_{\text{val}}}^{N_\ell} (f_{\ell_i} + f_{\bar{\ell}_i}), \tag{11.5}$$

$$f_\nu = \sum_i^{N_\ell} (f_{\nu_i} + f_{\bar{\nu}_i}), \tag{11.6}$$

$$f_q = \sum_i^{N_u} (f_{u_i} + f_{\bar{u}_i}) + \sum_i^{N_d} (f_{d_i} + f_{\bar{d}_i}). \tag{11.7}$$

Here $N_u = 3$ as the top quark becomes active as well above μ_{EW}. For the neutral current components, we convert the PDFs back to the mass basis and sum over γ, Z and the mixing γZ. Besides the EW PDFs, we also show the ones obtained through the pure QED⊗QCD evolution for ℓ_{sea}, q, g and $\gamma, Z, \gamma Z$ and the leading order splittings for neutrino and W_T PDFs. The difference between the solid and dashed curves quantifies the (higher-order) EW corrections. At $Q = 1$ TeV, the overall size of EW corrections is about $10\% \sim 20\%$, depending on the specific components. If we look at a specific flavor, such as the down-type quarks, the EW corrections can be much larger, due to the relatively large SU(2)$_\text{L}$ gauge coupling compared with the corresponding electromagnetic one. The EW corrections to the neutral current PDFs are as large as 20%, mostly due to the new components, Z and γZ. The LO splittings for W_T and ν come from $\mu \to W\nu$, which correspond to the Effective W/Z Approximation [262, 263, 3]. At a small x, the resummed neutrino PDF f_ν deviates from the LO $1/(1-x)$ behavior due to the higher-order returns in the splitting $W \to \ell\nu$. For the f_{W_T} PDF, the higher-order corrections are positive at small x and negative at large x. In Fig. 11.1, we also demonstrate the W_L PDF, which does not evolve with scale Q at the leading order, as a remnant of the EW symmetry breaking.

11.2 The standard candle cross sections at a $\mu^+\mu^-$ collider

In this section, we consider W^+W^- and ZH production at a multi-TeV $\mu^+\mu^-$ collider as standard candles to illuminate the effects of EW PDFs. This is done by comparing the cross sections for $\mu^+\mu^-$ annihilation and VV scattering to the analogous final state. The impact on the other SM processes such as $t\bar{t}, HH$, and $t\bar{t}H$ production at high invariant mass can be found in Refs. [253] and di-jet production at low invariant mass in Ref. [254]. In Fig. 11.2, we show the semi-inclusive cross sections and the corresponding decomposition versus the collider center-of-mass energy $\sqrt{s}$ from 1 to 30 TeV. Tight cutoffs $|\cos\theta| < 0.99$ and $\sqrt{\hat{s}} > 500$ GeV, where $\sqrt{\hat{s}}$ is the invariant mass of the diboson system, have been imposed for the W/Z initiated processes in the center-of-mass frame to assure the validity of EW PDF formalism. Compared with the annihilation processes, VBF takes over at higher energies around $\sqrt{s} \approx 2$ TeV for both W^+W^- and ZH production. At $\sqrt{s} = 30$ TeV, the VBF cross sections are 3 orders of magnitude larger than direct annihilation.

When examining the decomposition, we see the W^+W^- production is mainly contributed from the $\gamma\gamma$ and $W_T W_T$. This is a general feature for EW gauge boson productions, due to the self-coupling of the non-Abelian gauge group SU(2)$_\text{L}$. The neutral current channels $\gamma\gamma, ZZ, \gamma Z$ dominate over the $W_T W_T$ one due to the relatively large PDFs, which is explicitly shown in Fig. 11.1 at $Q = 1$ TeV. W_T gives a larger contribution than W_L due to the large logarithm enhancement in the W_T PDF, while W_L does not evolve with scales. In comparison, we see ZH production mainly comes from the $W_T W_L$ component, which contributes over 90% of the total cross section. It can be understood in terms of the Goldstone equivalence theorem [250, 264]. The Higgs is largely mediated by the longitudinal gauge W_L, due to the large scalar self-coupling. Compared with the $W_T W_T$ component, the $W_L W_L$ one is about one order of magnitude larger, as a result of the large interaction to the longitudinal Z boson.

As we know, the kinematic distribution of the direct annihilation behaves very differently from the fusion processes. The key features are the invariant mass and rapidity of the final-
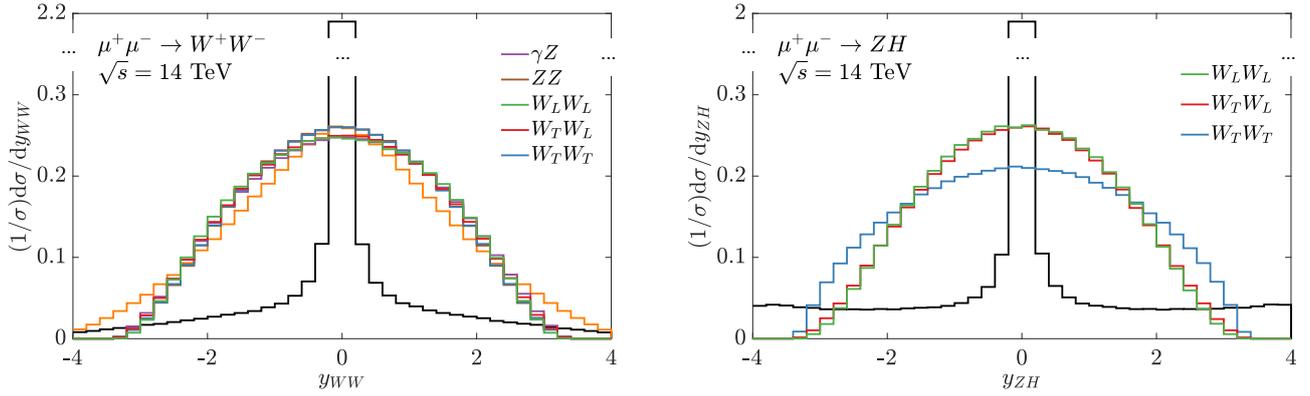
Figure 11.3: Normalized di-boson rapidity distributions for W^+W^- (Left) and ZH (Right) production at a muon collider at $\sqrt{s} = 14$ TeV. Annihilation ($\mu\mu$, black) and diboson fusion (colored) processes are compared.

state particle system. In an annihilation process, the final-state particle system carries the full collider energy, while the invariant mass of a fusion system starts from low energy around the threshold and drops very fast. The corresponding distributions are already explicitly shown in Ref. [253] for $t\bar{t}$ production and in Ref. [254] for di-jet production. The general features remain the same for W^+W^- and ZH production. The normalized rapidity distributions of the di-boson systems of W^+W^- and ZH production from various components are shown in Fig. 11.3 for a possible $\mu^+\mu^-$ collider at $\sqrt{s} = 14$ TeV. As expected, the annihilation ($\mu\mu$, black histogram in the plot) sharply peaks around $y_{ij} \sim 0$, with long tails at larger rapidities due to initial state radiation (ISR). In contrast, the fusion processes show a much larger spread in rapidity. Comparing different fusions to W^+W^- production, we see the $\gamma\gamma$-initiated processes (orange histogram) show larger tails while the EW gauge boson-initiated ones exhibit smaller rapidity values. For the ZH production (Fig. 11.3, right), the transversal W_TW_T spreads out more than the longitudinal components.

Finally, the normalized pseudo-rapidity (η) distributions of the final-state bosons in the W^+W^- and ZH production are shown in Fig. 11.4. We note that both bosons are included in the η distributions. For the W^+W^- production, we see a large rate of the W bosons are produced in the forward region, especially for the annihilation and $\gamma\gamma$ fusion processes. In direct annihilation, the W^+W^- can be produced through t-channel neutrino exchange, which gives the collinear $1/(1 - \cos^2\theta)$ behavior of the final W bosons[1]. A similar t-channel exists for the $\gamma\gamma$ fusion process through the W boson exchange. This collinear feature is largely regulated in the EW gauge boson-initiated processes by the mass effect. In the ZH production, we see the s-channel $(1 - \cos^2\theta)$ behavior for the annihilation process. In the fusion ones, the W_T-initiated process gives much more central final states while the W_L-initiated one is relatively forward.

---

[1]The singularity is regulated by the W boson mass.

11.3 Summary

In high-energy collisions at future colliders, splitting phenomena involving weak bosons begin to dominate because of the logarithmic enhancement in t, u-channel exchanges of weak bosons. The EW PDF formalism should be adopted, which factorizes the scattering processes into the hard partonic cross sections and the collinear PDFs. The PDFs evolve according to the SM DGLAP equations, which effectively resums potentially large logarithms. The EW PDFs for high-energy leptonic beams are completed in the recent works Refs. [253, 254]. In this report, some follow-up and supplementary results are presented.

In Section 11.1, we present the EW PDFs at the EW matching scale $Q = M_Z$ and one higher scale $Q = 1$ TeV, and explore the QCD threshold uncertainty by varying the matching scale within $\mu_{\text{QCD}} = 0.5 \sim 0.7$ GeV [260]. The impacts on the quark and gluon PDFs of a muon beam at $Q = M_Z$ are less than 10%, while no impact on the lepton and photon PDFs are observed. This uncertainty becomes smaller when energy evolves to higher scales. Above the EW scale at $Q = 1$ TeV, we explicitly demonstrate the EW corrections to light-flavor PDFs are about 10% $\sim$ 20%. The higher-order correction to the Effective W/Z Approximation is positive (negative) at small (large) momentum fraction x. The corrections to the neutral current PDFs are mainly due to the new contribution from the Z and γZ components.

In Section 11.2, we take W^+W^- and ZH production at a high-energy muon collider as standard candles to illuminate the effects of EW PDFs. We see the VBFs take over the annihilation processes around the center-of-mass collision energy $\sqrt{s} \approx 2$ TeV. The EW PDF formalism gives the advantage to examine the decomposition from various sub-channels. We find that the transverse gauge bosons initiated processes dominate the W^+W^- production, while the ZH mainly comes from W_LW_T due to the Goldstone equivalence theorem [250, 264]. Some important kinematic distributions are explicitly presented.

In this report, we mainly explored the EW PDFs for a high-energy muon beam and the corresponding effects at muon col-
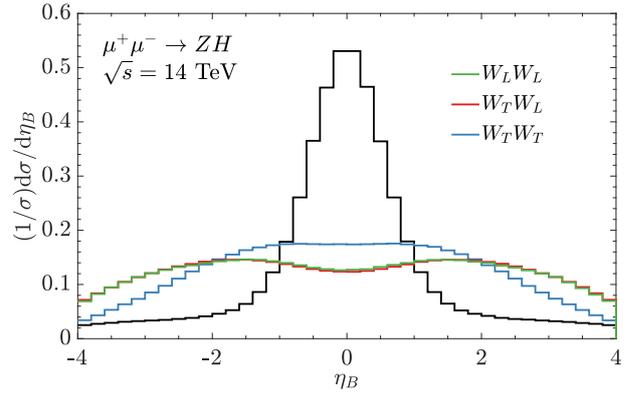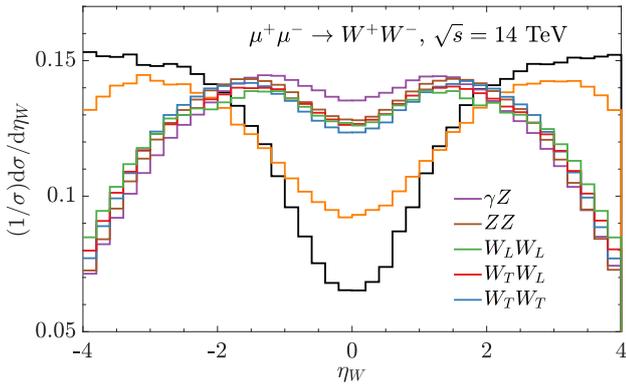
Figure 11.4: In W^+W^- (Left) and ZH (Right) production for a muon collider at $\sqrt{s} = 14$ TeV, the normalized pseudo-rapidity distributions of each boson (η_W on the left, and η_B on the right). Annihilation ($\mu\mu$, black histograms) and diboson fusion (colored histograms) processes are compared.

liders. It can be easily extended to an electron collider, which is examined in the recent work Ref. [254]. The EW PDF formalism is equally applicable to the proton beam, with quarks and gluons as the radiation source, which is expected to make an impact on the future 100 TeV proton-proton colliders [248, 249].

12 EW parton showers

Monte Carlo event generators have become an indispensable component of the particle physics toolkit. In most cases, they are the only valid option for the translation of theoretical models to predictions for data measured at collider experiments. At the LHC Run 2, analyses are already frequently limited by theoretical uncertainties, originating from either incomplete modeling of the underlying physics or from insufficient statistics due to the inefficiency of current codes. With the upcoming luminosity upgrade of the LHC and future colliders in mind, the improvement of the current state of the art in terms of both accuracy and efficiency is thus critically important.

Fortunately, recent years have seen a number of developments on both fronts. In the area of computational efficiency, major issues are being tackled. An example is the improvement in the treatment of negative event weights, which often occur in the context of matching fixed-order calculations to parton showers and lead to lower statistical power of an event sample. They may be tackled by improvement of the matching procedure [265, 266], re-sampling techniques [267, 268], or they may be used as training data for generative machine learning models which can then be used to sample unweighted events [269, 270]. Those same generative models offer an exciting new avenue for the sampling of multi-leg, fixed-order calculations [271, 272, 273, 269], which are currently a major computational bottleneck for analyses that require matrix element merging up to high multiplicities. Complementary perspectives include avoiding negative event weights altogether [91].

In the area of theoretical accuracy, some of the remaining challenges are of a technical nature. For instance, NNLO cal-
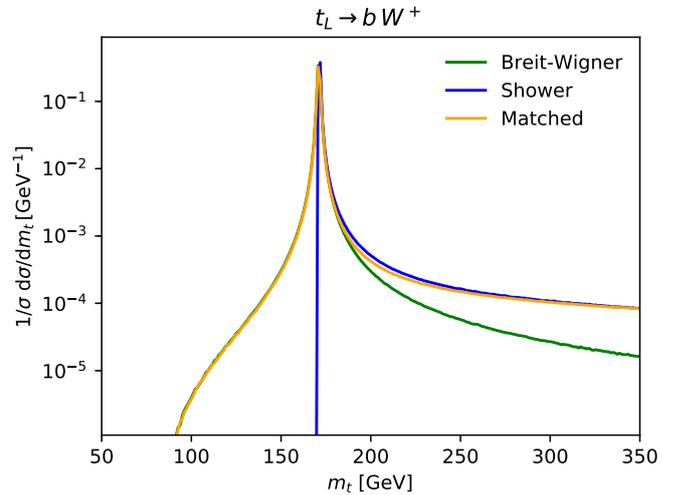
Figure 12.1: Mass spectra of the decay of a 1 TeV left-handed top quark. The matched spectrum (orange) is the numerical combination of the Breit-Wigner distribution (green) for small virtualities, and the shower distribution (blue) for large virtualities.

culations are becoming increasingly available, but their matching to parton showers and the merging of higher-multiplicity LO or NLO samples is a very complex task, see for example Refs. [274, 275]. Even if it is solved in a general sense, the resulting event generators may prove to be computationally prohibitive. On the other hand, the challenges in the field of parton shower development are of a more theoretical nature, and much progress has been made there in recent years. The requirements for formal NLL accuracy were set out in Refs. [276, 277, 278], and progress on the inclusion of the higher-order branching kernels is being made [279, 280]. Much work has also been done on the inclusion of sub-leading color effects [281, 282, 283, 284, 285], although they are not yet part of standard event generator codes.
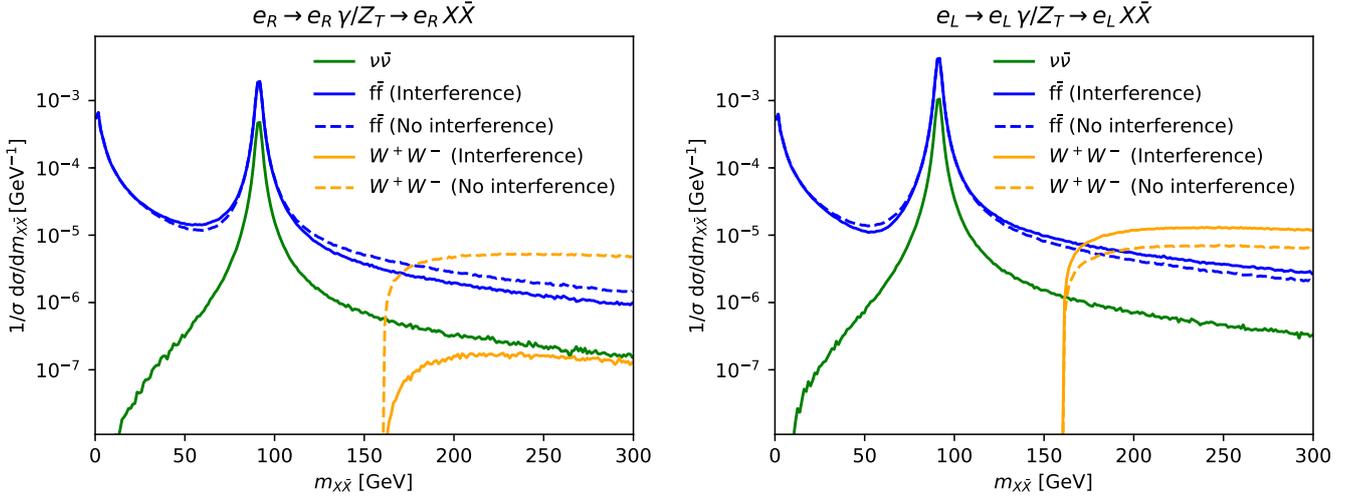
Figure 12.2: Invariant mass spectra resulting from including neutral boson interference in the showering of a 10 TeV left-handed electron (Left) and a right-handed electron (Right).

Finally, progress towards including EW effects in parton showers is currently being made [286, 287, 250, 288]. In the EW sector, the large logarithms resummed by the parton shower are regulated by the EW scale, but at sufficiently large energies still lead to sizable contributions. Negative virtual EW corrections have been computed and resummed for many processes and observables (see for instance Ref. [289] and references therein), and their incorporation into a parton shower offers a process-independent way of including such corrections systematically.

Similarly, at large enough energies, EW vector bosons, top quarks, and even Higgs bosons start to appear as parts of jets and contribute to fragmentation functions [290, 255, 291] and parton density functions [263, 262, 251, 252, 253, 254]. It is the connection to these last two points that make EW parton showers particularly relevant to VBS at higher energies. As described in Section 11, it becomes meaningful to discuss the W/Z content of high-energy leptons and protons. This means that the VBS process can be modeled, with some uncertainty, as the scattering of two initial-state EW bosons that propagate along the beam axis and carry no transverse momentum. In real life, initial-state W/Z bosons carry some p_T since they are generated perturbatively, i.e., through $f_i \rightarrow f_j V$ splitting where f_i and f_j are leptons or quarks. This absence of p_T is a source of uncertainty but is precisely described by backwards evolution / fragmentation in EW parton showers [292]. (This is analogous to matching $gg \rightarrow t\bar{t}$ to $qg \rightarrow t\bar{t}q$ and $qq \rightarrow t\bar{t}qq'$ via backwards evolution in QCD.) Therefore, using EW boson PDFs to describe VBS at high energies requires an EW parton shower to correctly describe particle kinematics. Eventially, all of these effects must be included in the general-purpose event generators. A particular case study is the implementation of EW corrections into the Vincia parton shower [293], which highlights some of the unique features that appear in the EW sector at high energies.

12.1 Vincia: Electroweak showers in simulation

Parton showers are a critical component of Monte Carlo event generators, serving as the link between high-scale, fixed-order calculations and low-scale, non-perturbative physics. They offer a process-independent and fully differentiable resummation framework, incorporating the large logarithms associated with soft and collinear branchings of the partons produced in the hard scattering [294]. The Vincia shower is one of many showers currently available, which all make slightly different choices in their modeling of the same physics. Vincia is based on the antenna subtraction formalism [295, 296], of which implementation details may be found in Ref. [293]. One of Vincia's unique features is that it allows for the evolution of states of definite helicity [297, 298]. Due to the chiral nature of the EW sector, this type of propagation of spin information is crucial for the correct modeling of EW corrections. In the following, a qualitative outline is given on the modeling a number of features that are unique to the EW sector. Technicalities of the implementation are detailed in Refs. [288].

12.2 Branching kernels

Branching kernels are one of the core components of a parton shower. They contain the dynamics of the soft and collinear branchings it generates. The calculation of EW branching kernels, which are antenna functions in case of Vincia, mostly proceeds analogously to their QCD counterpart. The EW sector contains a rich physical landscape, leading to a vast number of collinear $1 \rightarrow 2$ branchings involving both spin-1 and spin-0 states. These include triple vector boson branchings, like $W^{\pm *} \rightarrow W^{\pm} Z$; branchings that involve a Higgs, like $Z^* \rightarrow Zh$; and resonance-type branchings, like $t \rightarrow bW^+$ or $Z^* \rightarrow t\bar{t}$. Particular care needs to be taken in the calculation of branching rates that involve longitudinal polarizations, where the scalar component can lead to spurious, unitarity-violating terms. These may be removed by performing the calculation in a suitable
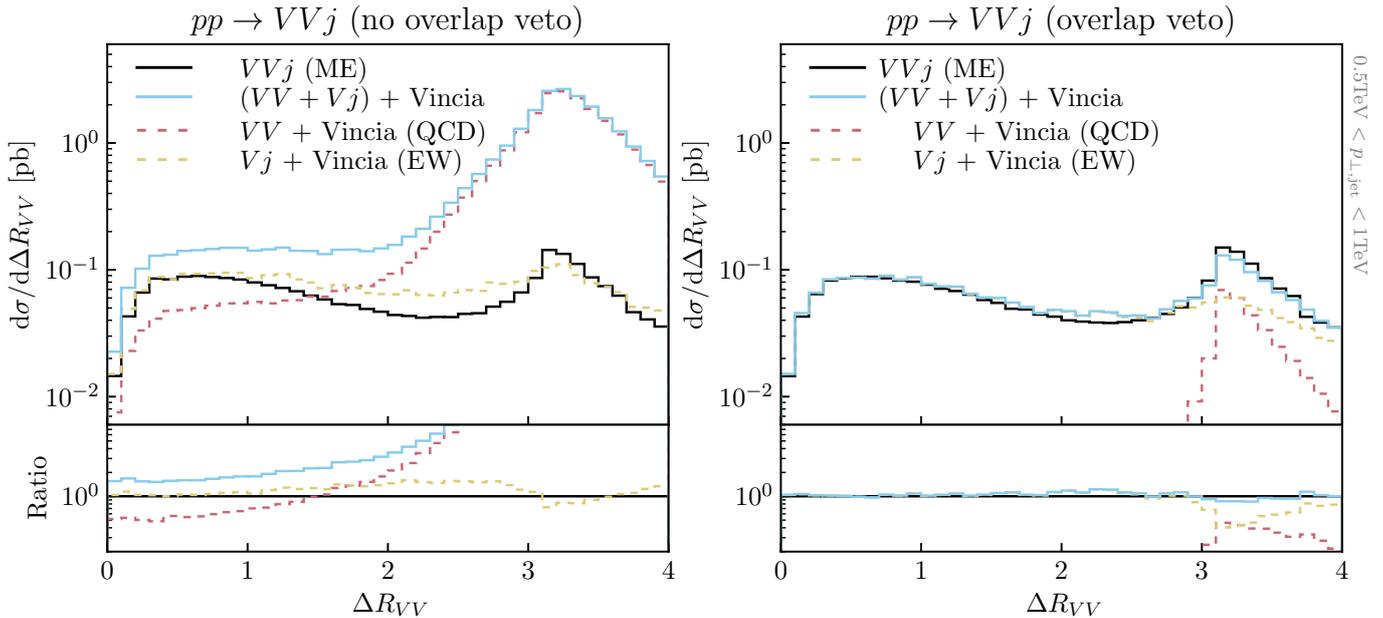
Figure 12.3: Upper: As a function of angular separation between the vector bosons ΔR_{VV}, the LO matrix element (ME) for $pp \to VVj$ (solid black) and the VINCIA prediction (solid blue), which consists of the sum of $pp \to VV$ + Vincia QCD (dashed red) and $pp \to Vj$ + Vincia EW (dashed yellow), evaluated at 14 TeV when the overlap veto is disabled (left) or enabled (right). Lower: Ratio with respect to LO ME. All simulations require jet p_T in the range $p_T \in (0.5\ \text{TeV},\ 1\ \text{TeV})$.

gauge and using Goldstone-gauge boson equivalence [250, 299, 300], or by using the spinor-helicity formalism and isolating the terms directly [288]. The results, computed for all possible spin states, reveal many features that are a direct consequence of EW symmetry breaking. For example, one observes the usual mass-suppression in the branching $Q_L \to Q_R Z_T$ in correspondence with the QCD branching $Q_L \to Q_R g$, but additional terms proportional to m_z^2 also appear. On the other hand, the branching $Q_L \to Q_R Z_L$ is not mass-suppressed, but it instead behaves like a scalar branching in correspondence with Goldstone boson equivalence.

12.3 Resonance matching

The EW shower includes branchings like $Z \to f\bar{f}$, which would normally be associated with a resonance decay. When these branchings occur at virtualities $Q^2 \gg Q_{EW}^2$, the resonance mass is a small correction and the EW shower offers an accurate description of the underlying physics. However, closer to the EW scale, it is well-known that the branching spectrum should follow a mass-dependent Breit-Wigner distribution. Interestingly, the Breit-Wigner distribution involves a different kind of resummation through the Dyson summation of the width. It is theoretically unclear how these two resummations should be matched, so the Vincia implementation makes use of a numerical matching procedure that complements PYTHIA [301]'s usual treatment of resonances. That is, any resonances produced by the EW shower are assigned a mass according to a Breit-Wigner distribution. The resonance-type branchings of EW shower are then suppressed close to the EW scale, and the resonance is decayed when the shower passes the off-shellness scale of the

resonance. An example of a top quark resonance decay spectrum is shown in Fig. 12.1.

12.4 Neutral boson interference

The EW sector contains multiple neutral bosons that may interfere with each other. For instance, the EW shower paradigm models the process $e_{L/R} \to e_{L/R} Z_T/\gamma \to e_{L/R} W^+ W^-$ as an incoherent sum of two separate contributions corresponding with intermediate Z_T or γ. However, in this process the interference between the neutral boson can lead to $\mathcal{O}(1)$ effects. To see this, one may consider that the $Z_T/\gamma \to W^+ W^-$ coupling is purely of SU(2) nature. An e_R has small SU(2) content, so the coherent $W^+ W^-$-contribution should be suppressed, while the e_L has large SU(2) content, leading to an enhancement. For reasons of computational efficiency, the Vincia implementation incorporates this effect at leading order only by applying an event weight that corrects the incoherent sum of branching kernels to a coherent one. The result of the application of this event weight is shown in Fig. 12.2. Note that the neutrino rate is not modified because it does not couple to the intermediate photon. The $W^+ W^-$ rates are affected due to the SU(2) nature of the $\gamma/Z\ W^+ W^-$ coupling.

12.5 Double counting of hard processes

When QCD and EW branchings are both enabled, a technical double counting problem may appear. To see this, consider for example the process $pp \to VVj$. For any point in phase space, this final state may be reached either by starting from $pp \to VV$ and adding an initial-state QCD emission. The same

configuration can also be obtain by starting from $pp \rightarrow Vj$ and adding an EW emission. Including both types of emissions leads to a double counting issue that needs to be addressed explicitly.

To that end, VINCIA generalizes a procedure used in Ref. [286], wherein a veto based on a k_T-like measure is applied to ensure that every phase space point is populated by the path that describes the physics the most accurately. A validation of this procedure is shown in Fig. 12.3, where VINCIA is compared to the LO matrix element of $pp \rightarrow VVj$ as a function of the angular separation between the vector bosons ΔR_{VV} and with the requirement $0.5 \text{ TeV} < p_{\perp,\text{jet}} < 1 \text{ TeV}$. The VINCIA prediction consists of the sum of $pp \rightarrow VV$ with a QCD emission and $pp \rightarrow Vj$ with an EW emission. For small angular separations, the vector bosons are collinear and the EW shower should perform best, while at large angular separation the vector bosons are back-to-back and the QCD shower should be preferred. In absence of the overlap veto, the VINCIA prediction clearly overshoots the direct matrix element significantly, while closely matching it when it is enabled.

12.6 Summary

The incorporation of EW corrections in parton showers is one of the many promising recent developments in the development and improvement of Monte Carlo event generators. The EW sector offers a rich physics landscape that leads to a large number of inspiring challenges. In this section, features of EW corrections in parton showers, and particularly in Vincia, have been highlighted. While the most significant contributions are included in this implementation, many outstanding problems such as soft coherence, spin-interference effects and Bloch-Nordsieck violation, have yet to be solved. VINCIA's EW shower has been part of PYTHIA since its 8.304 release.

13 SMEFT with VBS at $\mu^+\mu^-$ colliders

As discussed above, the community has started to discuss the possibility of a multi-TeV muon collider [247, 302, 303, 304, 305]. As their mass is about 200 times heavier than the electron mass, they emit much less synchroton radiation, suggesting that muons could be ideal candidates to explore the high-energy frontier. At the same time, being fundamental particles, they do not entail the challenges of proton colliders in terms of QCD background, and could potentially allow for a rather clean environment. The main challenges however all stem from the fact that muons are not stable particles, and their decay complicates both beam production and detector designs [306, 307, 247]. Despite the serious R&D challenges, there has been a recent increase of interest with many studies assessing the physics potential of these machines [302, 303, 304, 305, 308, 309, 310, 311, 312, 313, 314, 315, 316, 317, 253, 318, 319, 292, 320].

In particular it has been observed that at sufficiently high energies, one expects VBS to become the dominant production mode with respect to s-channel production. This seems to hold not only for SM processes, but also for not too heavy

BSM scenarios [302]. Leaving aside the discovery potential, a muon collider seems to be also an ideal machine to probe new physics indirectly, taking advantage of the high energy scatterings of EW bosons to scout tails of distributions and exploit enhanced energy behavior. In this perspective, the SMEFT offers a flexible, semi- model- independent framework to parameterize new physics and it is worth exploring the prospects of indirectly finding BSM at muon colliders through VBS. Such a program would build on and complement the on-going program at the LHC (for additional details on the LHC program, see also Sections 1.3, 5, and 6.3).

13.1 EW bosons luminosities

Since it can be shown that above ~ 5 TeV a muon collider becomes effectively an EW boson collider [302, 292], it is worth having a comparison of the potential for EW VBS between muon and proton colliders. In order to make this comparison, we employ the language of parton luminosity and make use of the Effective W/Z Approximation [263, 262], or sometimes also called the Effective Vector Boson Approximation. This allows us to describe the emission of EW bosons on the same footing as QCD partons in protons, i.e., describe the W/Z content of a lepton or proton beam. Under this approximation, splitting functions can be used to describe the likelihood of collinear $f \rightarrow Vf'$ splitting, where f is any lepton or quark and V is an EW gauge boson.

In particular, for W/Z bosons of helicity λ and longitudinal energy fraction $\xi = E_V/E_f$, the leading order PDFs for a transversely polarized ($f_{V_T/f}$) and longitudinally polarized ($f_{V_0/f}$) V are given by the expressions

$$f_{V_T/f}(\xi, \mu_f) = \frac{C}{16\pi^2}$$
$$\times \frac{(g_V^f \mp g_A^f)^2 + (g_V^f \pm g_A^f)^2(1-\xi)^2}{\xi} \log\left(\frac{\mu_f^2}{M_V^2}\right), \quad (13.1)$$

$$f_{V_0/f}(\xi, \mu_f) = \frac{C}{4\pi^2}(g_V^{f\,2} + g_A^{f\,2})\left(\frac{1-\xi}{\xi}\right). \quad (13.2)$$

Here, μ_f is the collinear factorization scale, M_V is the mass of $V = W/Z$, and C, g_V^f, and g_A^f represent the appropriate weak gauge couplings of f. Explicitly, these are given by

$$\text{for } V = W: \quad C = \frac{g^2}{8}, \quad g_V^f = -g_A^f = 1, \quad (13.3)$$

$$\text{for } V = Z: \quad C = \frac{g^2}{\cos^2 \theta_W}, \quad g_V^a = \frac{1}{2}\left(T_L^3\right)^f - Q^f \sin^2 \theta_W,$$
$$g_A^f = -\frac{1}{2}\left(T_L^3\right)^f, \quad (13.4)$$

where Q^f is the electric charge of f, $(T_L^3)^f$ is its weak isospin charge, $g \approx 0.65$ is the weak coupling constant, and θ_W is the usual weak mixing angle. Note that the PDFs here are not resummed, unlike those discussed in Section 11.

Given these PDFs, we can define the parton luminosity (Φ) for helicity-polarized W^+W^- pairs carrying polarizations (λ_1, λ_2),
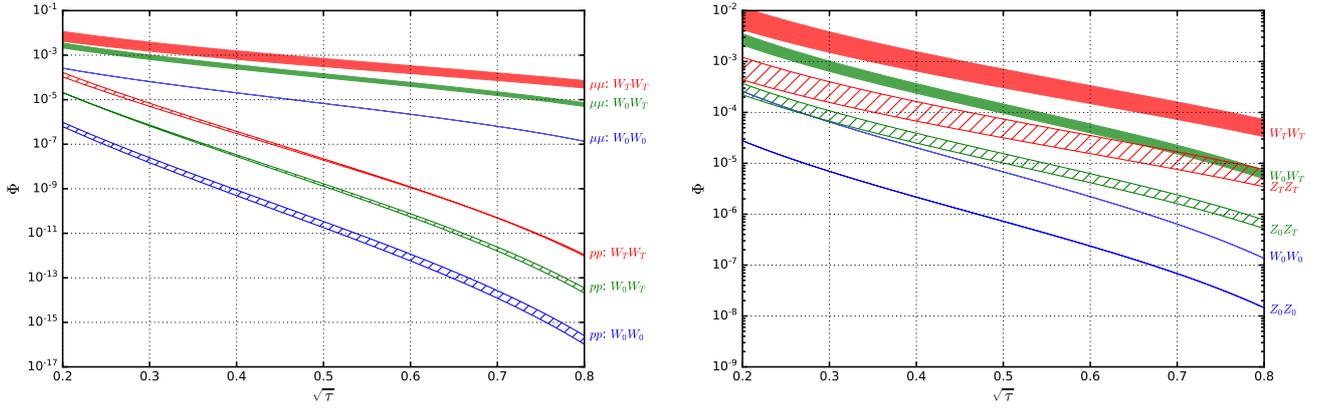
Figure 13.1: Parton luminosities Φ as a function of the scattering energy fraction $\sqrt{\tau} = M_{VV'}/\sqrt{s}$ (see text). Comparison between the WW parton luminosities at muon and proton colliders (Left), and the difference between Z and W bosons luminosities at a muon collider (Right). The parton luminosities have been decomposed among the various helicity combinations. Bands are given by variations of the factorization scales. Adapted from Ref. [302].

and a squared invariant mass of $M_{WW}^2 = (p_{W^+} + p_{W^-})^2 \equiv \tau s$ in a muon collider of energy $\sqrt{s}$ as

$$\Phi_{W_{\lambda_1}^+ W_{\lambda_2}^-}(\tau, \mu_f) = \int_\tau^1 \frac{d\xi}{\xi} f_{W_{\lambda_1}/\mu}\left(\xi, \mu_f\right) f_{W_{\lambda_2}/\mu}\left(\frac{\tau}{\xi}, \mu_f\right). \quad (13.5)$$

For a proton collider, the analogous expression is given by additional convolutions of W/Z PDFs in quarks with quark PDFs in protons. Analytically, this given by

$$\Phi_{V_\lambda V_{\lambda'}'}(\tau, \mu_f) = \frac{1}{1 + \delta_{V_\lambda V_{\lambda'}'}} \int_\tau^1 \frac{d\xi}{\xi} \int_{\tau/\xi}^1 \frac{dz_1}{z_1} \int_{\tau/(\xi z_1)}^1 \frac{dz_2}{z_2} \sum_{q,q'}$$

$$f_{V_\lambda/q}(z_2) f_{V_{\lambda'}'/q'}(z_1) \left[f_{q/p}(\xi) f_{q'/p}\left(\frac{\tau}{\xi z_1 z_2}\right) + f_{q/p}\left(\frac{\tau}{\xi z_1 z_2}\right) f_{q'/p}(\xi) \right].$$
$$(13.6)$$

Here, $f_{q/p}$ are the usual PDFs for quarks in a proton.

As it can be seen in Fig. 13.1, where we plot the luminosities as function of the hard scattering energy fraction $\tau = M_{WW}^2/s$, at a muon collider we would benefit from much higher parton luminosities. This is particularly striking at high energy, where the proton luminosities are significantly more suppressed. On the right of the figure, we also show a comparison between W and Z luminosities at a muon collider, observing an expected order of magnitude difference in favor of the WW components.

13.2 VBS prospects

The aforementioned analysis seems to indicate that a high-energy muon collider is the perfect stage to fully exploit VBS and explore the EW sector. As a matter of fact, VBS provide unique sensitivity at high energies and is a fundamental part of a successful program of EW precision measurements. At the LHC there are significant challenges since signal-to-background ratios are not favorable. In particular, it is diboson production which dominates, but this class of processes
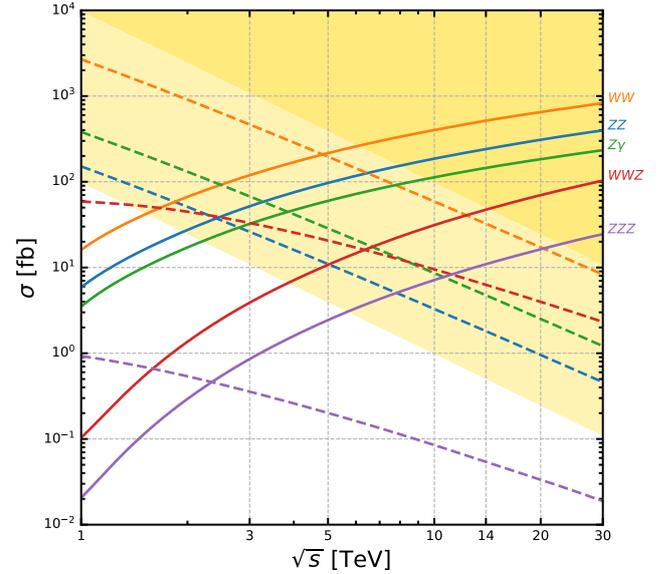
Figure 13.2: Multi-boson production cross sections at a muon collider as a function of colliding energy. Solid lines show VBS production while dashed lines show s-channel ones. The former benefits from a logarithmic growth with respect to the latter that decreases with energy. The light-shaded region corresponds to at least 10k expected events, while the darker shaded region to 1M. Adapted from Ref. [302].

probe very different kinematic regimes and interactions. At a muon collider the situation is reversed: diboson production is significantly smaller, and becomes negligible at high energy (see Fig. 13.2). In terms of SMEFT operators at dimension six, the most relevant ones that affect VBS physics are listed in Ta-

Operator	Coefficient	Definition
$O_{\varphi B}$	$c_{\varphi B}$	$\left(\varphi^\dagger \varphi\right) B^{\mu\nu} B_{\mu\nu}$
$O_{\varphi W}$	$c_{\varphi W}$	$\left(\varphi^\dagger \varphi\right) W_I^{\mu\nu} W_{\mu\nu}^I$
$O_{\varphi WB}$	$c_{\varphi WB}$	$(\varphi^\dagger \tau_I \varphi) B^{\mu\nu} W_{\mu\nu}^I$
$O_{\varphi D}$	$c_{\varphi D}$	$(\varphi^\dagger D^\mu \varphi)^\dagger (\varphi^\dagger D_\mu \varphi)$
O_W	c_{WWW}	$\epsilon_{IJK} W_{\mu\nu}^I W^{J,\nu\rho} W_\rho^{K,\mu}$

Table 13.1: Dimension-six SMEFT operators most relevant to
VBS physics.

ble 13.1.

The listed operators modify in particular the self- interaction of the EW bosons and the coupling to the Higgs as well. They do so with different Lorentz structures with respect to the SM ones. It is important to remember that the SMEFT should be treated globally, since it is unrealistic that only certain operators are generated by the full UV theory. However, currently no global analysis including VBS exist but simplified analysis can already bring useful information to the table. Recently in Ref. [120] a first step to include VBS processes in a global fit has been taken. In particular, they perform a joint analysis with diboson data at the LHC and observe that VBS can improve the sensitivity to several dimension-six operators, while opening up new windows on operators like $O_{\varphi B}$ and $O_{\varphi W}$, which are left basically unconstrained by diboson data. We can give a first estimate of the potential to constrain these operators at a high-energy muon collider, by assuming that a cross section measurement compatible to the SM is obtained. The total cross section in the SMEFT at linear level is given by

$$\sigma = \sigma_{SM} + \sum_i \frac{C_i}{\Lambda^2} \sigma_i, \qquad (13.7)$$

where i runs through the different operators affecting the process. One can project limits at 95% CL on the Wilson coefficients C_i by a simple signal-to-background estimate

$$\mathcal{S} = \frac{S}{\sqrt{B}} = \frac{|\mathcal{L} \cdot (\sigma - \sigma_{SM})|}{\sqrt{\mathcal{L} \cdot \sigma_{SM}}} \leq 2. \qquad (13.8)$$

Here, $\mathcal{S}$ is the statistical significance of the simplified Gaussian estimator, and S (B) is the number of signal (background) events for an integrated luminosity $\mathcal{L}$. (See Ref. [247] for details on the projected luminosities at a muon collider.) In Fig. 13.3 we show the projections for benchmark collider energies 3 and 14 TeV, combining three different processes.

The importance of combining multiple processes and measurements cannot be possibly understated. A single data point presents flat directions in the Wilson coefficients parameter space and the combination of them is crucial to break the degeneracies and gain sensitivity. As expected, we see a striking improvement when we consider a multi-TeV machine as compared to a few-TeV one. In particular, this is the result of both a higher cross section (more statistics) and the energy enhanced operator effects, that concur in increasing dramatically the sensitivity.

13.3 Summary

Muon colliders are among the most promising machines to probe the EW sector by exploring both the precision and high-energy frontiers. In this section we discussed how muon colliders are effectively EW boson colliders, allowing us to fully exploit the sensitivity to new physics that the scattering of vector bosons can probe. In particular, we showed projections on the bounds that can be imposed on two operators that are still left unconstrained by diboson data at the LHC. This analysis is however very simplistic, including only inclusive cross sections. Since no observable optimization was performed, nor differential distributions used, this is arguably a conservative projection.

14 BSM with VBS at $\mu^+\mu^-$ colliders

The starting point of this section is the observation [302, 292] that at sufficiently high energies the EW VBS/VBF become the dominant production mechanisms at a multi-TeV lepton collider. We anticipate this holding for all SM final states relevant to studying the EW sector and/or the direct search of (not too heavy) new physics.

The main interest of this section is the BSM capabilities of a multi-TeV muon collider but we present first some results of relevant production processes via VBF, namely

$$\mu^+\mu^- \to X \nu_\mu \bar{\nu}_\mu \qquad (14.1)$$

and their counterpart from muon annihilation (through the *s*-channel). Some cross sections of SM processes are shown in Table 14.1. As already stated, the VBF processes shown here and also their partner with muons in the final state ($\mu^+\mu^- \to X\mu^+\mu^-$) exhibit a logarithmic growth in the cross section with increasing collider energy, and eventually overcome the *s*-channel production processes [302].

14.1 New Physics Potential at a multi-TeV μ Collider

In this section, we present a survey of BSM models and the potential sensitivity of a $\mu^+\mu^-$ collider. We note that BSM searches at future lepton colliders have been studied previously in the literature [321]. However the energy range considered was $\sqrt{s} \leq 3$ TeV. Conversely, we extend the energy up to $\sqrt{s} = 30$ TeV to better exploit the cross section growth with energy due to VBF. Explicitly, we consider the *s*-channel annihilation and VBF processes

$$\mu^+\mu^- \to X \quad \text{and} \quad \mu^+\mu^- \to X\ell\ell'. \qquad (14.2)$$

Here, $\ell \in \{\mu^\pm, \overset{(-)}{\nu}_\mu\}$ and X is some BSM final state, which may include SM particles. We focus on the complementary nature of the two processes because while *s*-channel annihilation grants accesses to the highest available partonic center-of-mass energies, it comes at the cost of a cross section suppression that scales as $\sigma \sim 1/s$ when far above production threshold. On the other hand, in VBF, the emission of transversely polarized, *t*-channel bosons gives rise to logarithmic factors that grow with
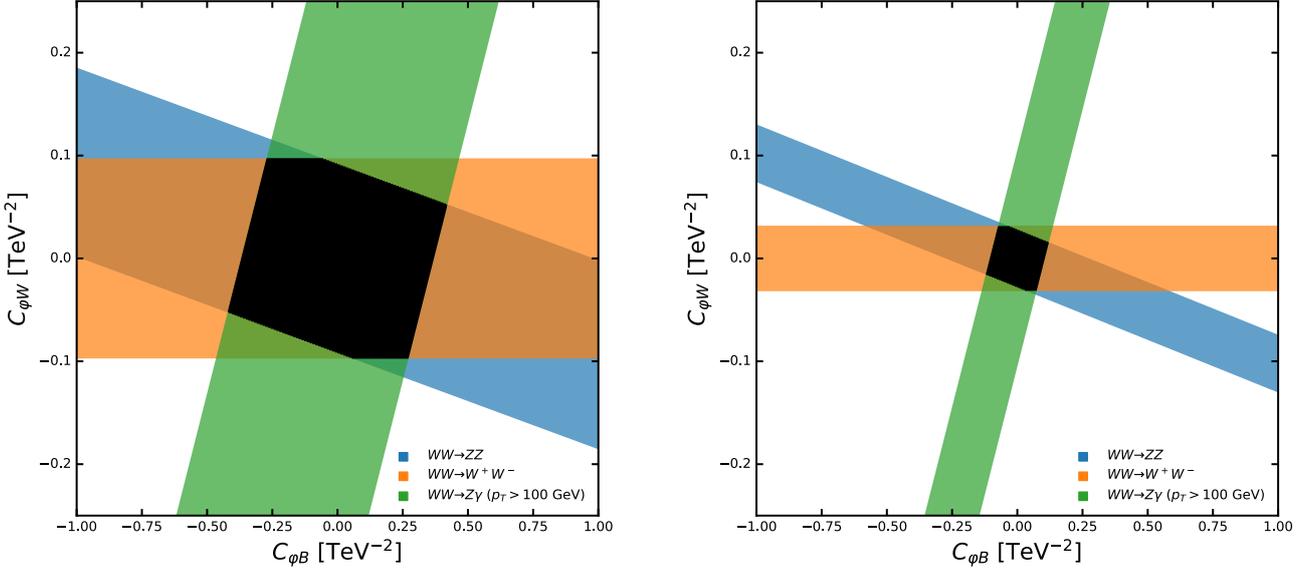
Figure 13.3: Projections for the limits imposed on the Wilson coefficients C of the operators $O_{\varphi B}$ and $O_{\varphi W}$ at a future muon collider at 3 TeV (Left) and 14 TeV (Right). Adapted from Ref. [302].
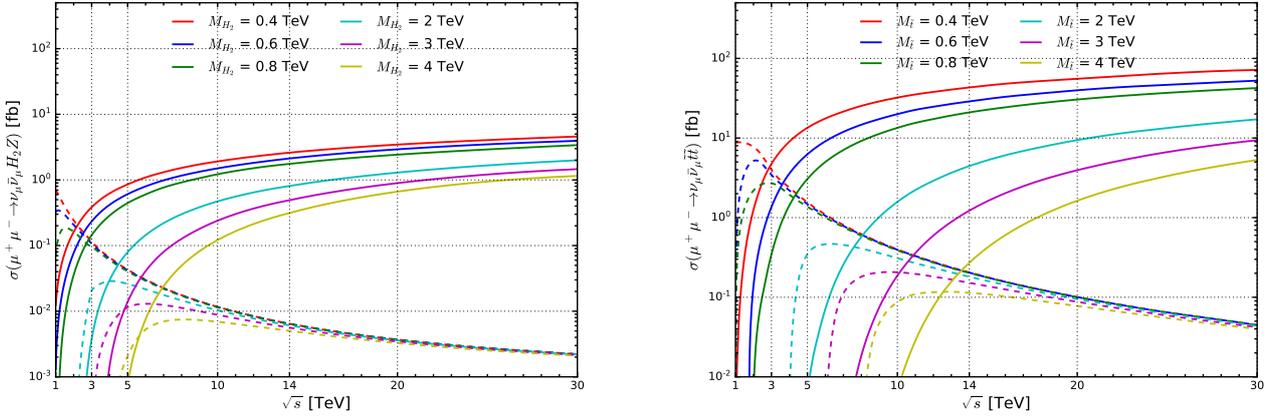
Figure 14.1: Cross section [fb] via VBF (solid lines) and s-channel annihilation (dashed lines) for $H_2 Z$ associated production in the 2HDM (left) and $\bar{\tilde{t}}\tilde{t}$ pair production in the MSSM (right), from Ref. [302].

σ [fb]	$\sqrt{s} = 1$ TeV		$\sqrt{s} = 3$ TeV		$\sqrt{s} = 14$ TeV		$\sqrt{s} = 30$ TeV	
	VBF	s-ch.	VBF	s-ch.	VBF	s-ch.	VBF	s-ch
$t\bar{t}$	$4.3{\cdot}10^{-1}$	$1.7{\cdot}10^{2}$	$5.1{\cdot}10^{0}$	$1.9{\cdot}10^{1}$	$2.1{\cdot}10^{1}$	$8.8{\cdot}10^{-1}$	$3.1{\cdot}10^{1}$	$1.9{\cdot}10^{-1}$
H	$2.1{\cdot}10^{2}$	-	$5.0{\cdot}10^{2}$	-	$9.4{\cdot}10^{2}$	-	$1.2{\cdot}10^{3}$	-
HH	$7.4{\cdot}10^{-2}$	-	$8.2{\cdot}10^{-1}$	-	$4.4{\cdot}10^{0}$	-	$7.4{\cdot}10^{0}$	-
WW	$1.6{\cdot}10^{1}$	$2.7{\cdot}10^{3}$	$1.2{\cdot}10^{2}$	$4.7{\cdot}10^{2}$	$5.3{\cdot}10^{2}$	$3.2{\cdot}10^{1}$	$8.5{\cdot}10^{2}$	$8.3{\cdot}10^{0}$
ZZ	$6.4{\cdot}10^{0}$	$1.5{\cdot}10^{2}$	$5.6{\cdot}10^{1}$	$2.6{\cdot}10^{1}$	$2.6{\cdot}10^{2}$	$1.8{\cdot}10^{0}$	$4.2{\cdot}10^{2}$	$4.6{\cdot}10^{-1}$

Table 14.1: $W^{+}W^{-}$ fusion and analogous s-channel annihilation cross sections σ [fb] for various VBF and s-channel processes in the SM as a function of collider energy $\sqrt{s}$ [TeV].

the available collider energy (see, *e.g.*, Section 13.1 for additional details). Thus, VBF probes a continuum of mass scales while avoiding a strict $1/s$-suppression, but at the cost of EW coupling suppression.

As shown here and throughout previous sections, VBF production cross sections (σ^{VBF}) grow with increasing $\sqrt{s}$, a phenomenon that follows from the propensity for forward emission of transverse gauge bosons at increasing collider energies. While the precise dependence of σ^{VBF} on collider energies of course depends on the precise BSM signature, for example on the particles involved, their underlying dynamics, and their kinematics, it nevertheless contrasts with s-channel, annihilation processes. These processes feature cross sections ($\sigma^{s-ch.}$) that instead decrease with collider energy as $\sigma^{s-ch.} \sim 1/s$, when well above kinematic thresholds. Hence, just as in the SM, we find a commonality in all VBF process here: assuming fixed model inputs, then for sufficiently high collider energies, VBF cross sections exceed those of analogous, s-channel production modes.

Moreover we can roughly estimate the collider energy $\sqrt{s}$ at which σ^{VBF} surpasses $\sigma^{s-ch.}$ for a given final-state mass M_X. Essentially, one must solve for when [302]

$$\frac{\sigma^{\text{VBF}}}{\sigma^{s-ch.}} \sim \mathcal{S} \left(\frac{g_W^2}{4\pi} \right)^2 \left(\frac{s}{M_X^2} \right) \log^2 \frac{s}{M_V^2} \log \frac{s}{M_X^2} > 1. \quad (14.3)$$

Here, s is the total collider energy and the multiplicity factor $\mathcal{S}$ accounts for the number of transverse polarization configurations contributing to the scattering process. This behavior is observed in the associated production of $H_2 Z$ in a 2HDM depicted in Fig. 14.1.

Finally, Ref. [302] investigated the sensitivity of EW VBS to a variety of BSM scenarios at multi-TeV muon colliders. In order to give an overview picture of this reach, we present in Fig. 14.2 the requisite integrated luminosity $\mathcal{L}$ [fb^{-1}] for a 5σ discovery as a function of new particle mass in $\sqrt{s} = 14$ TeV (solid) and 30 TeV (dashed) muon collisions. There, the authors considered specifically the doubly charged Higgs H^{++} (red) from the Georgi-Machacek model, $\bar{t}\bar{t}$ (blue), $\tilde{\chi}^+\tilde{\chi}^-$ (purple), and $\tilde{\chi}^0\tilde{\chi}^0$ (yellow) pairs from the MSSM. As dedicated signal and background analyses are beyond the scope of this document, a zero background hypothesis and full signal acceptance was assumed. Likewise, Ref. [302] used as a simple measure of statistical significance ($\mathcal{S}$) the formula, $\mathcal{S} = \sqrt{\mathcal{L} \times \sigma}$. While this estimate is optimistic, it nevertheless gives a global picture of the ultimate physics capabilities of the collider.

14.2 Complex Triplet Extension of the Standard Model

In this Section we discuss the extension of the SM with a complex triplet with $Y = 0$, which we label the complex Triplet extension of the SM (cTSM). The gauge and fermion sectors are identical to the SM ones, whereas the scalars of the model before EW symmetry breaking are

$$\Phi = \begin{pmatrix} \phi^+ \\ \Phi_0 \end{pmatrix}, \qquad T = \frac{1}{\sqrt{2}} \begin{pmatrix} t_0 & \sqrt{2}\,t_1^+ \\ \sqrt{2}\,t_2^- & -t_0 \end{pmatrix}, \quad (14.4)$$
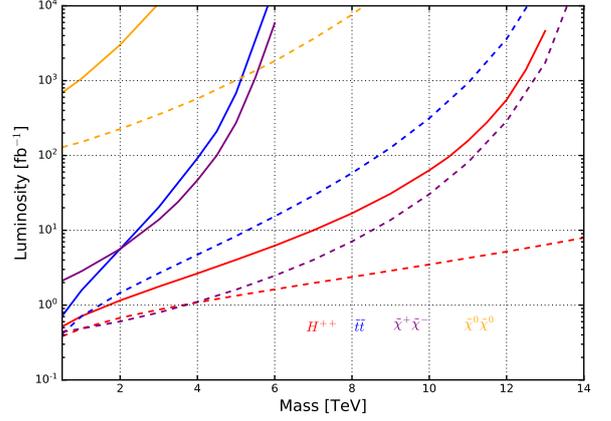
Figure 14.2: Required luminosity [fb] for a 5σ discovery of H^{++} (red) in the Georgi-Machacek model; $\bar{t}\bar{t}$ (blue), $\tilde{\chi}^+\tilde{\chi}^-$ (purple), and $\tilde{\chi}^0\tilde{\chi}^0$ (yellow) from in the MSSM, using VBF in $\sqrt{s} = 14$ TeV (solid) and 30 TeV (dashed) muon collisions. Adapted from Ref. [302].

where Φ is a scalar doublet under SU(2)$_L$ and T is a scalar triplet under SU(2)$_L$. We describe here the main feature of the model and the interested reader could find more detail in Ref. [315]. As already stated, the only difference with the SM relies in the scalar sector. Apart from the SM(-like) Higgs boson h_D, there is a second neutral Higgs boson h_T, a massive pseudoscalar a_P, and two massive charged scalars $h_{T,P}^\pm$. Due to symmetry reasons, the pseudoscalar and one of the charged Higgs bosons are aligned with their gauge eigenstates, even after EW symmetry breaking. The most important consequence is that the massive pseudoscalar is a natural dark matter candidate. In order to study the model one can apply the phenomenological constraint on relevant mass (m_{h_D}) and Higgs-mixing ($\mathcal{R}_{11}^S$) [315]:

$$m_{h_D} = 125.18 \pm 0.16\,\text{GeV}, \quad \left| \mathcal{R}_{11}^S \right| > .99, \quad (14.5)$$

and also make sure that the loop-induced interaction $h_D \gamma \gamma$, which are modified by the charged scalars $h_{T,P}^\pm$, is consistent with the Higgs in diphoton signal strength [322, 323]:

$$\mu_{\gamma\gamma}^{\text{ATLAS}} = 0.99^{+0.15}_{-0.14}, \quad \mu_{\gamma\gamma}^{\text{CMS}} = 1.10^{+0.20}_{-0.18}. \quad (14.6)$$

Results are presented in Fig. 14.3. In particular in the upper plot of Fig. 14.3 we show Ωh^2 versus m_{DM}, computed with MADDM v.3.0 [324]. The blue points satisfy Eq. 14.5 together with the constraint from the diphoton signal, and are allowed by the constraint on direct dark matter searches. By looking at the zoomed plots, one can see that the value for the DM mass for which the correct dark matter relic is achieved is

$$m_{DM} \equiv m_{a_P}^{min} \sim 1.5\,\text{TeV}, \quad (14.7)$$

Reference [315] has also considered the physics reach for some processes at a muon collider. These results are presented in Fig. 14.3 (lower plot), where the significance is plotted as
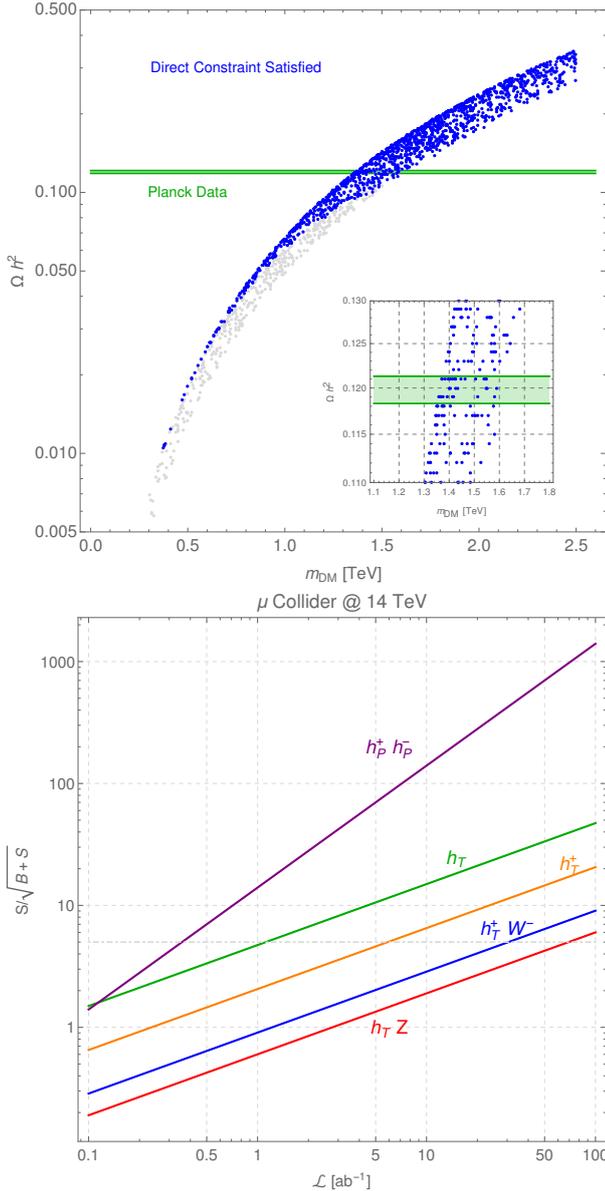
Figure 14.3: Upper: Relic density as a function of the DM. In blue (gray) the points that are allowed (disallowed) by the direct searches [325, 326, 327]. The green area represent the Planck results [328]. Lower: Significance vs luminosity for the h_T, $h_T^{\pm}$, $h_T^+ W^-$, $h_T Z$ and $h_P^+ h_P^-$ production processes through VBF at a 14 TeV muon collider. The production cross sections are multiplied by the branching ratios $Br(h_T \to W^+ W^-)$ or $Br(h_T^+ \to W^+ Z)$, depending on the channel considered. The background considered is the VBF production of $W^+ W^- Z$ in the SM, with $M(W^+ W^-) = m_{h_T}$ or $M(W^+ Z) = m_{h_T^+}$. The process $h_P^+ h_P^-$ is considered background-free because $h_P^{\pm}$ is a long-lived state. Adapted from Ref. [315].

function of the luminosity for the h_T, $h_T^{\pm}$, $h_T^+ W^-$, $h_T Z$ and $h_P^+ h_P^-$ production processes through VBF at a 14 TeV muon collider. In the definition of the significance, $\sigma = S / \sqrt{S + B}$, S and B stand for the number of events for the signal and the background

respectively,

$$S : \sigma(\mu^+ \mu^- \to h_T \, \nu_\mu \bar{\nu}_\mu) \times Br(h_T \to W^+ W^-) \cdot \mathcal{L}, \quad (14.8)$$

$$B : \sigma(\mu^+ \mu^- \to W^+ W^- \, \nu_\mu \bar{\nu}_\mu) \cdot \mathcal{L}, \quad (14.9)$$

with $M(W^+ W^-) = m_{h_T} \pm 5$ GeV.

A similar strategy is applied to the single production of $h_T^{\pm}$ and the pair-production $h_T Z$ and $h_T^+ W^-$. For the charged scalar Higgs $h_T^{\pm}$, the branching ratio $Br(h_T^+ \to W^+ Z)$ was considered. This give a conservative estimate on the significance vs luminosity not because of the signal but for the higher cross section (via VBS) of $W^+ W^- Z$ compared to $W^+ W^- H$ [302]. The pair production $h_P^+ h_P^-$ has been considered background-free. The pure charged triplet $h_P^{\pm}$ has a single decay channel, namely $h_P^+ \to a_P(W^+)^*$. Whereas the pseudoscalar is undetectable, the process will give rise to displaced off-shell W boons: there is no SM process that have this particular final state. This also gives rise to displaced leptons/jets plus missing energy in the final-state.

14.3 Summary

In this section, we explored a variety of simplified extensions of the SM and have shown how large VBS luminosities can maximize the direct search for new physics. This feature is similar in all the BSM models considered and constitutes a motivation for a multi-TeV muon collider, together of course with the sensitivity to SM and SMEFT that a muon collider can achieve. Also considered was a specific model with a scalar dark matter candidate showing the interplay between cosmological constraint and collider searches at a multi-TeV muon collider.

15 HH production from new particles at 100 TeV

In this final section, we turn to the outlook for HH production in the decays of new resonances at a hypothetical 100 TeV pp collider. In general, VBS offers a unique window into new dynamics in the Higgs sector. In a class of models [330, 331, 332, 333, 334, 335], the SM Higgs doublet field, which contains four real fields, is itself a set of Goldstone modes, and are generated from the spontaneous breaking of a larger global symmetry at a new compositeness scale f_η. The strong dynamics at this scale would produce resonances which couple to the longitudinal polarizations of W and Z bosons and the Higgs boson, leading to typical VBS processes as well as double Higgs production via VBF [336]. In phenomenological model of Ref. [337], the Lagrangian

$$\mathcal{L} = \mathcal{L}_{\text{SM}} + \frac{1}{2} \partial^\mu \eta \partial_\mu \eta - \frac{1}{2} m_\eta^2 \eta^2 + \frac{a_\eta}{f_\eta} \eta \partial^\mu \pi^a \partial_\mu \pi^a, \quad (15.1)$$

describes the interaction of a new scalar resonance η with π^a, the quartet of Goldstone modes in the Higgs doublet. The resemblance of the notation to chiral perturbation theory is intentional. In the high-mass limit, the decay width of the η resonance is given by [337]

$$\Gamma_\eta = \frac{a_\eta^2 m_\eta^3}{8\pi f_\eta^2} \quad (15.2)$$
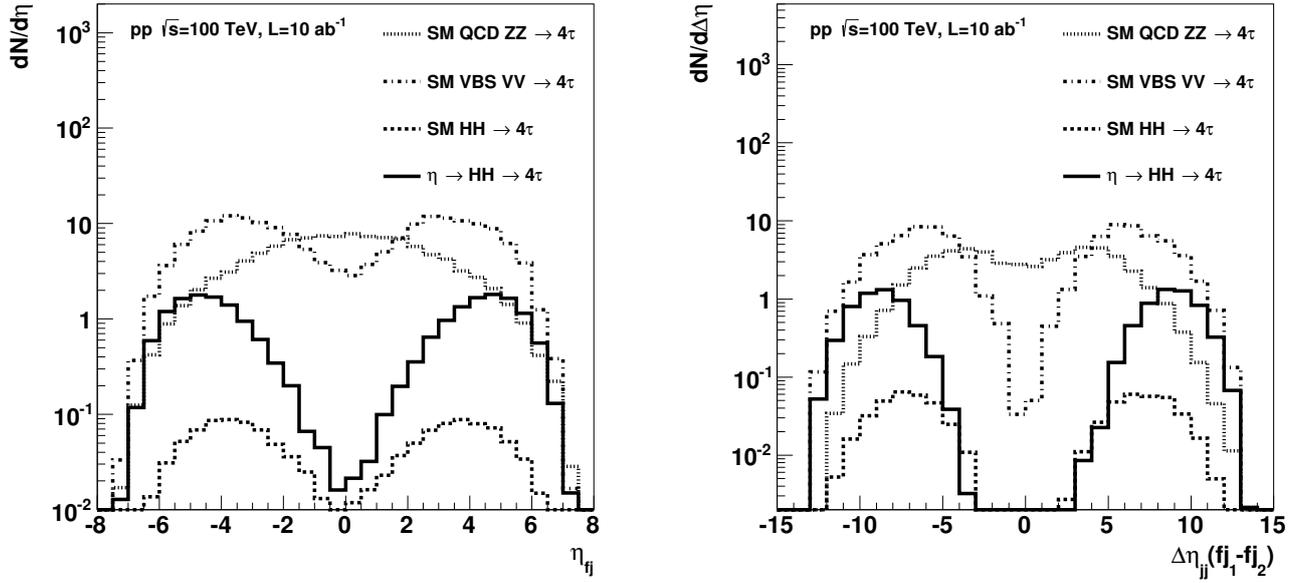
Figure 15.1: Left: The pseudo-rapidity distributions of the forward jets. Right: The distribution of the difference in pseudo-rapidities of the two forward jets. Figures are reproduced from Ref. [329].
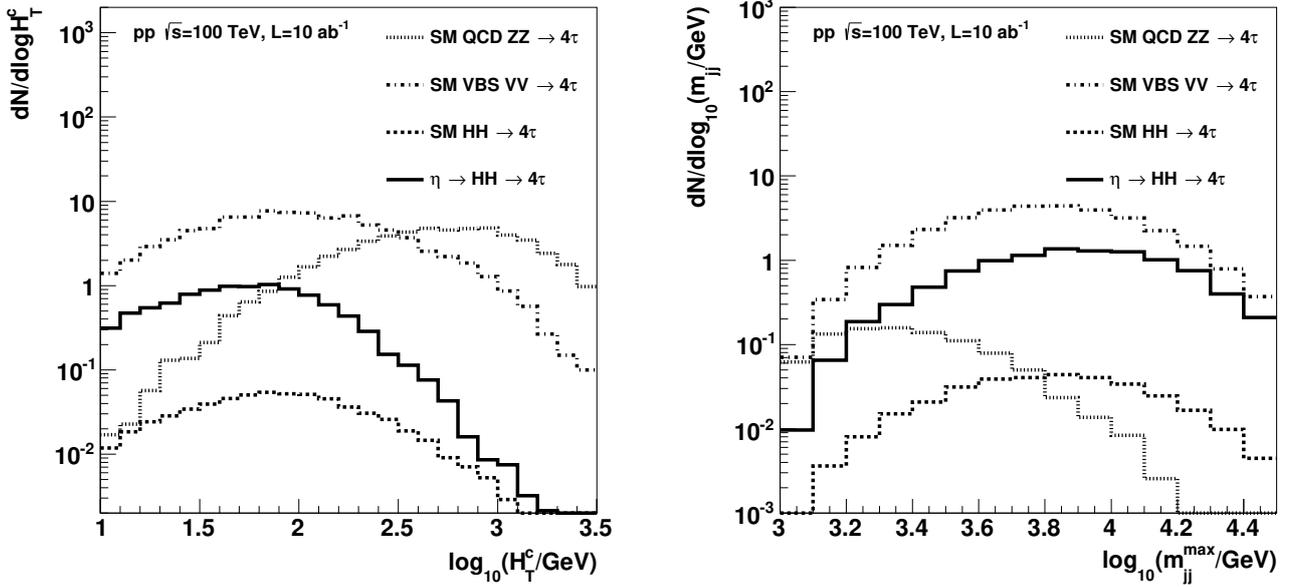
Figure 15.2: Left: The distribution of H_T^c, the scalar sum of the transverse momenta of the central jets. Right: The distribution of dijet mass of the forward jets. Figures are adapted from Ref. [329].

If the dimensionless coupling a_η is set to $a_\eta = 1$, the longitudinal VBS process is completely unitarized by the combination of Higgs boson and η boson exchange.

15.1 Results

A sensitivity study for this model was performed in Ref. [329] with the di-Higgs production channel in VBS, using the MADGRAPH5 [88, 89] and PYTHIA8 [301] generators to simulate pp collisions. The study focused on the $H \to \tau\tau$ decay mode, using a τ-tagging efficiency of 60%. The following irreducible

	m_η (TeV)					
$\mathcal{L}$ [ab^{-1}]	$\sqrt{s}$ = 50 TeV		$\sqrt{s}$ = 100 TeV		$\sqrt{s}$ = 200 TeV	
	20%	70%	20%	70%	20%	70%
1	1.26	1.89	1.75	2.81	2.27	3.85
3	1.58	2.31	2.25	3.42	2.88	4.65
10	2.02	2.83	2.90	4.18	3.66	5.63
30	2.49	3.36	3.56	4.94	4.44	6.60
100	3.06	3.97	4.33	5.83	5.38	7.74

(Table header above spans m_η (TeV).)

Table 15.1: 5σ discovery mass reach for the $\eta \to HH \to 4\tau$ resonance, as a function of the $\sqrt{s}$ of a pp collider. The fractional resonance width Γ_η/m_η is fixed at 20% and 70% respectively. These results are reproduced from [329].

background processes were included; (i) $VVjj \to 4\tau jj$ production ($V = Z, \gamma^*$) via purely EW couplings, (ii) $ZZjj \to 4\tau jj$ production via the presence of the strong coupling in the Feynman amplitudes, and (iii) $HHjj \to 4\tau jj$ production via purely EW couplings. Misidentified backgrounds were estimated and expected to be negligible due the to large τ multiplicity. More specifically, a $j \to \tau$ mis-identification rate of $\varepsilon_{j\to\tau} = 2\%$ would lead to a suppression factor of $(\varepsilon_{j\to\tau})^4 \lesssim 2 \cdot 10^{-5}\%$ for multi-jet processes, even before the application of strong selection cuts. In this analysis, all τ candidates were required to have $p_T(\tau_i) > 100$ GeV for $i = 1, \ldots, 4$, with the leading candidate having $p_T(\tau_1) > 300$ GeV, and a pseudorapidity of $|\eta(\tau_i)| < 3$. A multivariate analysis was used to combine the information from various kinematic quantities associated with the resonance decay products and the forward jets produced by the scattered partons. The discovery potential is shown in Table 15.1. Distributions of interest for the signal and background processes are shown in Figs. 15.1 and 15.2, which are reproduced from [329].

15.2 Summary

Using longitudinal VBS, a high-energy pp collider with energies beyond the LHC would be able to probe high-mass resonances due to new strong dynamics in the Higgs sector. The discovery reach extends into the multi-TeV mass range for such resonances, depending on the intrinsic width of the resonance and the collider energy and luminosity. At a 100 TeV pp collider with an integrated luminosity of 30 ab^{-1}, a scalar resonance of mass between 3.5 and 5 TeV (corresponding to a fractional width between 20% and 70%) is discoverable using the $H \to \tau\tau$ channel alone [329].

The trade-off between collider energy and integrated luminosity for a given discovery mass reach favors higher luminosities for a narrow, weakly-coupled resonance and higher energies for a wide, strongly-coupled resonance. For a fractional resonance width of 20% (70%), a factor of two in collider energy is equivalent to a factor of 4.3 (8.7) in integrated luminosity [329].

Part V
Conclusions

As outlined in the European Strategy Update for Particle Physics [16, 17], many open questions and mysteries exist in high energy physics. These range from the more definitive, with question such as, "How strongly does the Higgs couple to itself and other elementary particles?", to the more open-ended, with questions such as, "How does the EW sector behave in the massless limit?" In many cases, these mysteries can be understood through the presence of new particles and new interactions. That is to say, through the existence of new physics.

At TeV-scale colliders like the LHC, the HL-LHC, or their proposed successor experiments, these problems and solutions can be studied directly using the vector boson scattering (and fusion) mechanism [5, 6, 7, 8, 9, 10]. More specifically, with VBS one can study at the highest attainable energies: the self-coupling of the Higgs and EW bosons, the polarization of EW bosons and the respective roles played by longitudinal and transverse degrees of freedom, the existence of new particles and new interactions, boosted topologies and jet substructure, and even the behavior of top quarks and weak bosons in the near-massless limit. Exploring such rich physics, however, involves extreme challenges for detector development, which have since led to breakthroughs in hardware design, trigger design, and applications of machine learning. Such needs have also led to a revolution in theoretical developments, including: advances in EW parton showers and EW boson PDFs, advances in high-precision computations and simulation tools beyond NLO in QCD with parton shower matching, advances in Monte Carlo support for studying new physics models and EFTs at colliders, and novel investigations of VBS at future colliders.

These achievements and others have been made by a sizable component of the high-energy community. A snapshot of ongoing efforts to study VBS at current and future colliders is summarized in this report. The outlook is encouraging for the LHC and HL-LHC, and outright inspiring for future, multi-TeV colliders. With VBS, one hopes and anticipates to at last resolve some of the deepest questions surrounding how nature works.

Acknowledgments

The VBSCan (COST Action CA16108) and its companion networks are thanked for organizing the VBS at Snowmass meeting, which inspired this work, and for their financial support. All the members of the Action and also thanked for inspiring discussions. Talks presented at the VBS at Snowmass meeting are available from the URL:
https://indico.cern.ch/e/VSBCanSnowmass.

AC acknowledges support from FRS – FNRS under project T.04142.18. AD acknowledges financial support by the German Federal Ministry for Education and Research (BMBF) under contract no. 05H18WWCA1 and the German Research Foundation (DFG) under reference numbers DE 623/6-1 and DE 623/6-2. AVK acknowledges support from the U.S. Department of Energy, Office of High Energy Physics grant no. DE

The reproduction of this review or parts thereof is allowed as specified in the CC-BY-4.0 license.

References

[1] B. W. Lee, C. Quigg, H. B. Thacker, The Strength of Weak Interactions at Very High-Energies and the Higgs Boson Mass, Phys. Rev. Lett. 38 (1977) 883–885. doi:10.1103/PhysRevLett.38.883.

[2] B. W. Lee, C. Quigg, H. B. Thacker, Weak Interactions at Very High-Energies: The Role of the Higgs Boson Mass, Phys. Rev. D 16 (1977) 1519. doi:10.1103/PhysRevD.16.1519.

[3] M. S. Chanowitz, M. K. Gaillard, The TeV Physics of Strongly Interacting W's and Z's, Nucl. Phys. B 261 (1985) 379–431. doi:10.1016/0550-3213(85)90580-2.

[4] M. S. Chanowitz, M. K. Gaillard, Multiple Production of W and Z as a Signal of New Strong Interactions, Phys. Lett. B 142 (1984) 85–90. doi:10.1016/0370-2693(84)91141-9.

[5] M. Rauch, Vector-Boson Fusion and Vector-Boson Scattering (2016). arXiv:1610.08420.

[6] D. R. Green, P. Meade, M.-A. Pleier, Multiboson interactions at the LHC, Rev. Mod. Phys. 89 (2017) 035008. doi:10.1103/RevModPhys.89.035008. arXiv:1610.07572.

[7] C. F. Anders, et al., Vector boson scattering: Recent experimental and theory developments, Rev. Phys. 3 (2018) 44–63. doi:10.1016/j.revip.2018.11.001. arXiv:1801.04203.

[8] R. Bellan, et al., VBSCan Thessaloniki 2018 Workshop Summary, in: 2nd Vector Boson Scattering Coordination and Action Network Annual Meeting, 2019. arXiv:1906.11332.

[9] J. Baglio, et al., VBSCan Mid-Term Scientific Meeting, in: VBSCan Mid-Term Scientific Meeting, 2020. arXiv:2004.00726.

[10] R. Covarelli, M. Pellen, M. Zaro, Vector-Boson Scattering at the LHC: unravelling the Electroweak sector (2021). arXiv:2102.10991.

[11] A. M. Sirunyan, et al. (CMS collaboration), Observation of electroweak production of same-sign W boson pairs in the two jet and two same-sign lepton final state in proton-proton collisions at $\sqrt{s}$ = 13 TeV, Phys. Rev. Lett. 120 (2018) 081801. doi:10.1103/PhysRevLett.120.081801. arXiv:1709.05822.

[12] A. M. Sirunyan, et al. (CMS collaboration), Measurement of vector boson scattering and constraints on anomalous quartic couplings from events with four leptons and two jets in proton–proton collisions at $\sqrt{s}$ = 13 TeV, Phys. Lett. B 774 (2017) 682–705. doi:10.1016/j.physletb.2017.10.020. arXiv:1708.02812.

[13] M. Aaboud, et al. (ATLAS collaboration), Observation of electroweak $W^{\pm}Z$ boson pair production in association with two jets in pp collisions at $\sqrt{s}$ = 13 TeV with the ATLAS detector, Phys. Lett. B 793 (2019) 469–492. doi:10.1016/j.physletb.2019.05.012. arXiv:1812.09740.

[14] A. M. Sirunyan, et al. (CMS collaboration), Measurement of electroweak WZ boson production and search for new physics in WZ + two jets events in pp collisions at $\sqrt{s}$ =13 TeV, Phys. Lett. B 795 (2019) 281–307. doi:10.1016/j.physletb.2019.05.042. arXiv:1901.04060.

[15] ATLAS Collaboration, Observation of electroweak production of a same-sign W boson pair in association with two jets in pp collisions at $\sqrt{s}$ = 13 TeV with the ATLAS detector, Phys. Rev. Lett. 123 (2019) 161801. doi:10.1103/PhysRevLett.123.161801. arXiv:1906.03203.

[16] R. K. Ellis, et al., Physics Briefing Book: Input for the European Strategy for Particle Physics Update 2020 (2019). arXiv:1910.11775.

[17] 2020 Update of the European Strategy for Particle Physics, CERN Council, Geneva, 2020. doi:10.17181/ESU2020.

[18] V. Khachatryan, et al. (CMS collaboration), Study of vector boson scattering and search for new physics in events with two same-sign leptons and two jets, Phys. Rev. Lett. 114 (2015) 051801. doi:10.1103/PhysRevLett.114.051801. arXiv:1410.6315.

[19] ATLAS Collaboration, Evidence for Electroweak Production of $W^{\pm}W^{\pm}jj$ in pp Collisions at $\sqrt{s}$ = 8 TeV with the ATLAS Detector, Phys. Rev. Lett. 113 (2014) 141803. doi:10.1103/PhysRevLett.113.141803. arXiv:1405.6241.

[20] M. Aaboud, et al. (ATLAS collaboration), Search for anomalous electroweak production of WW/WZ in association with a high-mass dijet system in pp collisions at $\sqrt{s}$ = 8 TeV with the ATLAS detector, Phys. Rev. D 95 (2017) 032001. doi:10.1103/PhysRevD.95.032001. arXiv:1609.05122.

[21] V. Khachatryan, et al. (CMS collaboration), Measurement of electroweak-induced production of Wγ with two jets in pp collisions at $\sqrt{s}$ = 8 TeV and constraints on anomalous quartic gauge couplings, JHEP 06 (2017) 106. doi:10.1007/JHEP06(2017)106. arXiv:1612.09256.

[22] M. Aaboud, et al. (ATLAS collaboration), Measurement of $W^{\pm}W^{\pm}$ vector-boson scattering and limits on anomalous quartic gauge couplings with the ATLAS detector, Phys. Rev. D 96 (2017) 012007. doi:10.1103/PhysRevD.96.012007. arXiv:1611.02428.

[23] V. Khachatryan, et al. (CMS collaboration), Measurement of the cross section for electroweak production of Zγ in association with two jets and constraints on anomalous quartic gauge couplings in proton–proton collisions at $\sqrt{s}$ = 8 TeV, Phys. Lett. B 770 (2017) 380–402. doi:10.1016/j.physletb.2017.04.071. arXiv:1702.03025.

[24] M. Aaboud, et al. (ATLAS collaboration), Studies of Zγ production in association with a high-mass dijet system in pp collisions at $\sqrt{s}$ = 8 TeV with the ATLAS detector, JHEP 07 (2017) 107. doi:10.1007/JHEP07(2017)107. arXiv:1705.01966.

[25] M. Gallinaro, et al., Beyond the Standard Model in Vector Boson Scattering Signatures, in: International Workshop on BSM models in Vector Boson Scattering processes, 2020. arXiv:2005.09889.

[26] A. M. Sirunyan, et al. (CMS collaboration), Search for anomalous electroweak production of vector boson pairs in association with two jets in

proton-proton collisions at 13 TeV, Phys. Lett. B 798 (2019) 134985. doi:10.1016/j.physletb.2019.134985. arXiv:1905.07445.

[27] A. M. Sirunyan, et al. (CMS collaboration), Evidence for electroweak production of four charged leptons and two jets in proton-proton collisions at $\sqrt{s}$ = 13 TeV, Phys. Lett. B 812 (2021) 135992. doi:10.1016/j.physletb.2020.135992. arXiv:2008.07013.

[28] G. Aad, et al. (ATLAS collaboration), Observation of electroweak production of two jets and a Z-boson pair with the ATLAS detector at the LHC (2020). URL: https://arxiv.org/abs/2004.10612. arXiv:2004.10612.

[29] A. M. Sirunyan, et al. (CMS collaboration), Measurements of production cross sections of polarized same-sign W boson pairs in association with two jets in proton-proton collisions at $\sqrt{s}$ = 13 TeV, Phys. Lett. B 812 (2021) 136018. doi:10.1016/j.physletb.2020.136018. arXiv:2009.09429.

[30] M. Aaboud, et al. (ATLAS collaboration), Search for resonant WZ production in the fully leptonic final state in proton-proton collisions at $\sqrt{s}$ = 13 TeV with the ATLAS detector, Phys. Lett. B 787 (2018) 68–88. doi:10.1016/j.physletb.2018.10.021. arXiv:1806.01532.

[31] CMS collaboration, Measurement of the electroweak production of $Z\gamma$ and two jets in proton-proton collisions at $\sqrt{s}$ = 13 TeV and constraints on dimension 8 operators (2021). URL: https://cds.cern.ch/record/2759297.

[32] A. M. Sirunyan, et al. (CMS collaboration), Measurements of production cross sections of WZ and same-sign WW boson pairs in association with two jets in proton-proton collisions at $\sqrt{s}$ = 13 TeV, Phys. Lett. B 809 (2020) 135710. doi:10.1016/j.physletb.2020.135710. arXiv:2005.01173.

[33] M. Aaboud, et al. (ATLAS collaboration), Observation of electroweak $W^{\pm}Z$ boson pair production in association with two jets in pp collisions at $\sqrt{s}$ = 13 TeV with the ATLAS detector, Phys. Lett. B 793 (2019) 469–492. doi:10.1016/j.physletb.2019.05.012. arXiv:1812.09740.

[34] G. Aad, et al. (ATLAS collaboration), Search for the electroweak diboson production in association with a high-mass dijet system in semileptonic final states in pp collisions at $\sqrt{s}$ = 13 TeV with the ATLAS detector, Phys. Rev. D 100 (2019) 032007. doi:10.1103/PhysRevD.100.032007. arXiv:1905.07714.

[35] B. Biedermann, A. Denner, M. Pellen, Large electroweak corrections to vector-boson scattering at the Large Hadron Collider, Phys. Rev. Lett. 118 (2017) 261801. doi:10.1103/PhysRevLett.118.261801. arXiv:1611.02951.

[36] R. Frederix, S. Frixione, V. Hirschi, D. Pagani, H. S. Shao, M. Zaro, The automation of next-to-leading order electroweak calculations, JHEP 07 (2018) 185. doi:10.1007/JHEP07(2018)185. arXiv:1804.10017.

[37] M. Chiesa, A. Denner, J.-N. Lang, M. Pellen, An event generator for same-sign W-boson scattering at the LHC including electroweak corrections, Eur. Phys. J. C 79 (2019) 788. doi:10.1140/epjc/s10052-019-7290-6. arXiv:1906.01863.

[38] F. Caola, K. Melnikov, R. Röntsch, L. Tancredi, QCD corrections to ZZ production in gluon fusion at the LHC, Phys. Rev. D 92 (2015) 094028. doi:10.1103/PhysRevD.92.094028. arXiv:1509.06734.

[39] F. Caola, M. Dowling, K. Melnikov, R. Röntsch, L. Tancredi, QCD corrections to vector boson pair production in gluon fusion including interference effects with off-shell Higgs at the LHC, JHEP 07 (2016) 087. doi:10.1007/JHEP07(2016)087. arXiv:1605.04610.

[40] C. Li, Y. An, C. Charlot, R. Covarelli, Z. Guan, Q. Li, Loop-induced ZZ production at the LHC: An improved description by matrix-element matching, Phys. Rev. D 102 (2020) 116003. doi:10.1103/PhysRevD.102.116003. arXiv:2006.12860.

[41] A. M. Sirunyan, et al. (CMS collaboration), Observation of electroweak production of $W\gamma$ with two jets in proton-proton collisions at $\sqrt{s}$ = 13 TeV, Phys. Lett. B 811 (2020) 135988. doi:10.1016/j.physletb.2020.135988. arXiv:2008.10521.

[42] G. Aad, et al. (ATLAS collaboration), Evidence for electroweak production of two jets in association with a $Z\gamma$ pair in pp collisions at $\sqrt{s}$ = 13 TeV with the ATLAS detector, Phys. Lett. B 803 (2020) 135341. doi:10.1016/j.physletb.2020.135341. arXiv:1910.09503.

[43] A. M. Sirunyan, et al. (CMS collaboration), Measurement of the cross section for electroweak production of a Z boson, a photon and two jets in proton-proton collisions at $\sqrt{s}$ = 13 TeV and constraints on anomalous quartic couplings, JHEP 06 (2020) 076. doi:10.1007/JHEP06(2020)076. arXiv:2002.09902.

[44] G. Aad, et al. (ATLAS collaboration), Observation of electroweak production of two jets in association with an isolated photon and missing transverse momentum, and search for a Higgs boson decaying into invisible particles at 13 TeV with the ATLAS detector (2021). URL: https://arxiv.org/abs/2109.00925. arXiv:2109.00925.

[45] O. J. P. Eboli, M. C. Gonzalez-Garcia, J. K. Mizukoshi, $pp \rightarrow jje^{\pm}\mu^{\pm}\nu\nu$ and $jje^{\pm}\mu^{\mp}\nu\nu$ at $O(\alpha_{em}^6)$ and $O(\alpha_{em}^4\alpha_s^2)$ for the study of the quartic electroweak gauge boson vertex at CERN LHC, Phys. Rev. D 74 (2006) 073005. doi:10.1103/PhysRevD.74.073005. arXiv:hep-ph/0606118.

[46] G. Aad, et al. (ATLAS collaboration), Differential cross-section measurements for the electroweak production of dijets in association with a Z boson in proton–proton collisions at ATLAS, Eur. Phys. J. C 81 (2021) 163. doi:10.1140/epjc/s10052-020-08734-w. arXiv:2006.15458.

[47] D. Buarque Franzosi, O. Mattelaer, R. Ruiz, S. Shil, Automated predictions from polarized matrix elements, JHEP 04 (2020) 082. doi:10.1007/JHEP04(2020)082. arXiv:1912.01725.

[48] A. Ballestrero, E. Maina, G. Pelliccioli, Different polarization definitions in same-sign WW scattering at the LHC, Phys. Lett. B 811 (2020) 135856. doi:10.1016/j.physletb.2020.135856. arXiv:2007.07133.

[49] T. Melia, P. Nason, R. Rontsch, G. Zanderighi, W^+W^-, WZ and ZZ production in the POWHEG BOX, JHEP 11 (2011) 078. doi:10.1007/JHEP11(2011)078. arXiv:1107.5051.

[50] A. Ballestrero, et al., Precise predictions for same-sign W-boson scattering at the LHC, Eur. Phys. J. C 78 (2018) 671. doi:10.1140/epjc/s10052-018-6136-y. arXiv:1803.07943.

[51] J. Baglio, N. Le Duc, Fiducial polarization observables in hadronic WZ production: A next-to-leading order QCD+EW study, JHEP 04 (2019) 065. doi:10.1007/JHEP04(2019)065. arXiv:1810.11034.

[52] J. Baglio, L. D. Ninh, Polarization observables in WZ production at the 13 TeV LHC: Inclusive case, Commun. in Phys. 30 (2020) 35–47. doi:10.15625/0868-3166/30/1/14461. arXiv:1910.13746.

[53] A. Denner, G. Pelliccioli, Polarized electroweak bosons in W^+W^- production at the LHC including NLO QCD effects, JHEP 09 (2020) 164. doi:10.1007/JHEP09(2020)164. arXiv:2006.14867.

[54] A. Denner, G. Pelliccioli, NLO QCD predictions for doubly-polarized WZ production at the LHC, Phys. Lett. B 814 (2021) 136107. doi:10.1016/j.physletb.2021.136107. arXiv:2010.07149.

[55] R. Poncelet, A. Popescu, NNLO QCD study of polarised W^+W^- production at the LHC (2021). URL: https://arxiv.org/abs/2102.13583. arXiv:2102.13583.

[56] S. Chatrchyan, et al. (CMS collaboration), Measurement of the Polarization of W Bosons with Large Transverse Momenta in W+Jets Events at the LHC, Phys. Rev. Lett. 107 (2011) 021802. doi:10.1103/PhysRevLett.107.021802. arXiv:1104.3829.

[57] G. Aad, et al. (ATLAS collaboration), Measurement of the polarisation of W bosons produced with large transverse momentum in pp collisions at $\sqrt{s}$ = 7 TeV with the ATLAS experiment, Eur. Phys. J. C 72 (2012) 2001. doi:10.1140/epjc/s10052-012-2001-6. arXiv:1203.2165.

[58] G. Aad, et al. (CMS, ATLAS collaboration), Combination of the W boson polarization measurements in top quark decays using ATLAS and CMS data at $\sqrt{s}$ = 8 TeV, JHEP 08 (2020) 051. doi:10.1007/JHEP08(2020)051. arXiv:2005.03799.

[59] G. Aad, et al. (ATLAS collaboration), Measurement of the angular coefficients in Z-boson events using electron and muon pairs from data taken at $\sqrt{s}$ = 8 TeV with the ATLAS detector, JHEP 08 (2016) 159. doi:10.1007/JHEP08(2016)159. arXiv:1606.00689.

[60] V. Khachatryan, et al. (CMS collaboration), Angular coefficients of Z bosons produced in pp collisions at $\sqrt{s}$ = 8 TeV and decaying to $\mu^+\mu^-$ as a function of transverse momentum and rapidity, Phys. Lett. B 750 (2015) 154–175. doi:10.1016/j.physletb.2015.08.061. arXiv:1504.03512.

[61] R. K. Ellis, W. J. Stirling, B. R. Webber, QCD and collider physics, volume 8, Cambridge University Press, 2011.

[62] Z. Bern, et al., Left-Handed W Bosons at the LHC, Phys. Rev. D 84 (2011) 034008. doi:10.1103/PhysRevD.84.034008. arXiv:1103.5445.

[63] W. J. Stirling, E. Vryonidou, Electroweak gauge boson polarisation at the LHC, JHEP 07 (2012) 124. doi:10.1007/JHEP07(2012)124. arXiv:1204.6427.

[64] J. C. Collins, D. E. Soper, Angular Distribution of Dileptons in High-Energy Hadron Collisions, Phys. Rev. D 16 (1977) 2219. doi:10.1103/PhysRevD.16.2219.

[65] K. Kajantie, J. Lindfors, R. Raitio, QCD Angular Correlations for Muon Pair Production, Phys. Lett. B 74 (1978) 384–388. doi:10.1016/0370-2693(78)90685-8.

[66] J. C. Collins, Simple Prediction of QCD for Angular Distribution of Dileptons in Hadron Collisions, Phys. Rev. Lett. 42 (1979) 291. doi:10.1103/PhysRevLett.42.291.

[67] C. S. Lam, W.-K. Tung, A Parton Model Relation Sans QCD Modifications in Lepton Pair Productions, Phys. Rev. D 21 (1980) 2712. doi:10.1103/PhysRevD.21.2712.

[68] R. Gauld, A. Gehrmann-De Ridder, T. Gehrmann, E. W. N. Glover, A. Huss, Precise predictions for the angular coefficients in Z-boson production at the LHC, JHEP 11 (2017) 003. doi:10.1007/JHEP11(2017)003. arXiv:1708.00008.

[69] M. Aaboud, et al. (ATLAS collaboration), Measurement of $W^{\pm}Z$ production cross sections and gauge boson polarisation in pp collisions at $\sqrt{s}$ = 13 TeV with the ATLAS detector, Eur. Phys. J. C 79 (2019) 535. doi:10.1140/epjc/s10052-019-7027-6. arXiv:1902.05759.

[70] R. Aaij, et al. (LHCb collaboration), Search for lepton-universality violation in $B^{+} \rightarrow K^{+}\ell^{+}\ell^{-}$ decays, Phys. Rev. Lett. 122 (2019) 191801. doi:10.1103/PhysRevLett.122.191801. arXiv:1903.09252.

[71] J. P. Lees, et al. (BaBar collaboration), Measurement of an Excess of $\bar{B} \rightarrow D^{(*)}\tau^{-}\bar{\nu}_{\tau}$ Decays and Implications for Charged Higgs Bosons, Phys. Rev. D 88 (2013) 072012. doi:10.1103/PhysRevD.88.072012. arXiv:1303.0571.

[72] Y. Sato, et al. (Belle collaboration), Measurement of the branching ratio of $\bar{B}^{0} \rightarrow D^{*+}\tau^{-}\bar{\nu}_{\tau}$ relative to $\bar{B}^{0} \rightarrow D^{*+}\ell^{-}\bar{\nu}_{\ell}$ decays with a semileptonic tagging method, Phys. Rev. D 94 (2016) 072007. doi:10.1103/PhysRevD.94.072007. arXiv:1607.07923.

[73] R. Aaij, et al. (LHCb collaboration), Test of lepton universality in beauty-quark decays (2021). arXiv:2103.11769.

[74] A. Djouadi, The Anatomy of electro-weak symmetry breaking. II. The Higgs bosons in the minimal supersymmetric model, Phys. Rept. 459 (2008) 1–241. doi:10.1016/j.physrep.2007.10.005. arXiv:hep-ph/0503173.

[75] G. C. Branco, P. M. Ferreira, L. Lavoura, M. N. Rebelo, M. Sher, J. P. Silva, Theory and phenomenology of two-Higgs-doublet models, Phys. Rept. 516 (2012) 1–102. doi:10.1016/j.physrep.2012.02.002. arXiv:1106.0034.

[76] C. Degrande, K. Hartling, H. E. Logan, A. D. Peterson, M. Zaro, Automatic predictions in the Georgi-Machacek model at next-to-leading order accuracy, Phys. Rev. D 93 (2016) 035004. doi:10.1103/PhysRevD.93.035004. arXiv:1512.01243.

[77] B. Fuks, J. Neundorf, K. Peters, R. Ruiz, M. Saimpert, Majorana neutrinos in same-sign $W^{\pm}W^{\pm}$ scattering at the LHC: Breaking the TeV barrier, Phys. Rev. D 103 (2021) 055005. doi:10.1103/PhysRevD.103.055005. arXiv:2011.02547.

[78] B. Fuks, J. Neundorf, K. Peters, R. Ruiz, M. Saimpert, Probing the Weinberg operator at colliders, Phys. Rev. D 103 (2021) 115014. doi:10.1103/PhysRevD.103.115014. arXiv:2012.09882.

[79] V. Cirigliano, W. Dekens, J. de Vries, K. Fuyuto, E. Mereghetti, R. Ruiz, Leptonic anomalous magnetic moments in νSMEFT (2021). arXiv:2105.11462.

[80] G. Aad, et al. (ATLAS collaboration), Measurement of τ polarization in $W \rightarrow \tau\nu$ decays with the ATLAS detector in pp collisions at $\sqrt{s}$ = 7 TeV, Eur. Phys. J. C 72 (2012) 2062. doi:10.1140/epjc/s10052-012-2062-6. arXiv:1204.6720.

[81] M. Aaboud, et al. (ATLAS collaboration), Measurement of τ polarisation in $Z/\gamma^{*} \rightarrow \tau\tau$ decays in proton–proton collisions at $\sqrt{s}$ = 8 TeV with the ATLAS detector, Eur. Phys. J. C 78 (2018) 163. doi:10.1140/epjc/s10052-018-5619-1. arXiv:1709.03490.

[82] CMS collaboration, Updated search for a light charged Higgs boson in top quark decays in pp collisions at $\sqrt{s}$ = 7 TeV, Technical Report CMS-PAS-HIG-12-052, 2012.

[83] A. M. Sirunyan, et al. (CMS collaboration), A multi-dimensional search for new heavy resonances decaying to boosted WW, WZ, or ZZ boson pairs in the dijet final state at 13 TeV, Eur. Phys. J. C 80 (2020) 237. doi:10.1140/epjc/s10052-020-7773-5. arXiv:1906.05977.

[84] G. Aad, et al. (ATLAS collaboration), Reconstruction and identification of boosted di-τ systems in a search for Higgs boson pairs using 13 TeV proton-proton collision data in ATLAS, JHEP 11 (2020) 163. doi:10.1007/JHEP11(2020)163. arXiv:2007.14811.

[85] A. Denner, S. Dittmaier, P. Maierhöfer, M. Pellen, C. Schwan, QCD and electroweak corrections to WZ scattering at the LHC, JHEP 06 (2019) 067. doi:10.1007/JHEP06(2019)067. arXiv:1904.00882.

[86] A. Denner, R. Franken, M. Pellen, T. Schmidt, NLO QCD and EW corrections to vector-boson scattering into ZZ at the LHC, JHEP 11 (2020) 110. doi:10.1007/JHEP11(2020)110. arXiv:2009.00411.

[87] J. Baglio, et al., Release Note - VBFNLO 2.7.0 (2014). arXiv:1404.3940.

[88] T. Stelzer, W. F. Long, Automatic generation of tree level helicity amplitudes, Comput. Phys. Commun. 81 (1994) 357–371. doi:10.1016/0010-4655(94)90084-1. arXiv:hep-ph/9401258.

[89] J. Alwall, R. Frederix, S. Frixione, V. Hirschi, F. Maltoni, O. Mattelaer, H. S. Shao, T. Stelzer, P. Torrielli, M. Zaro, The automated computation of tree-level and next-to-leading order differential cross sections, and their matching to parton shower simulations, JHEP 07 (2014) 079. doi:10.1007/JHEP07(2014)079. arXiv:1405.0301.

[90] E. Bothmann, et al. (Sherpa collaboration), Event Generation with Sherpa 2.2, SciPost Phys. 7 (2019) 034. doi:10.21468/SciPostPhys.7.3.034. arXiv:1905.09127.

[91] P. Nason, A New method for combining NLO QCD with shower Monte Carlo algorithms, JHEP 11 (2004) 040. doi:10.1088/1126-6708/2004/11/040. arXiv:hep-ph/0409146.

[92] S. Frixione, P. Nason, C. Oleari, Matching NLO QCD computations with Parton Shower simulations: the POWHEG method, JHEP 11 (2007) 070. doi:10.1088/1126-6708/2007/11/070. arXiv:0709.2092.

[93] S. Alioli, P. Nason, C. Oleari, E. Re, A general framework for implementing NLO calculations in shower Monte Carlo programs: the POWHEG BOX, JHEP 06 (2010) 043. doi:10.1007/JHEP06(2010)043. arXiv:1002.2581.

[94] S. Actis, A. Denner, L. Hofer, A. Scharf, S. Uccirati, Recursive generation of one-loop amplitudes in the Standard Model, JHEP 04 (2013) 037. doi:10.1007/JHEP04(2013)037. arXiv:1211.6316.

[95] S. Actis, A. Denner, L. Hofer, J.-N. Lang, A. Scharf, S. Uccirati, RECOLA: REcursive Computation of One-Loop Amplitudes, Comput. Phys. Commun. 214 (2017) 140–173. doi:10.1016/j.cpc.2017.01.004. arXiv:1605.01090.

[96] A. Denner, S. Dittmaier, L. Hofer, Collier: a fortran-based Complex One-Loop LIbrary in Extended Regularizations, Comput. Phys. Commun. 212 (2017) 220–238. doi:10.1016/j.cpc.2016.10.013. arXiv:1604.06792.

[97] A. Denner, S. Pozzorini, One loop leading logarithms in electroweak radiative corrections. 1. Results, Eur. Phys. J. C 18 (2001) 461–480. doi:10.1007/s100520100551. arXiv:hep-ph/0010201.

[98] E. Accomando, A. Denner, S. Pozzorini, Logarithmic electroweak corrections to $e^{+}e^{-} \rightarrow \nu_{e}\bar{\nu}_{e}W^{+}W^{-}$, JHEP 03 (2007) 078. doi:10.1088/1126-6708/2007/03/078. arXiv:hep-ph/0611289.

[99] B. Biedermann, A. Denner, M. Pellen, Complete NLO corrections to $W^{+}W^{+}$ scattering and its irreducible background at the LHC, JHEP 10 (2017) 124. doi:10.1007/JHEP10(2017)124. arXiv:1708.00268.

[100] B. Fuks, M. Nemevšek, R. Ruiz, Doubly Charged Higgs Boson Production at Hadron Colliders, Phys. Rev. D 101 (2020) 075022. doi:10.1103/PhysRevD.101.075022. arXiv:1912.08975.

[101] P. Artoisenet, R. Frederix, O. Mattelaer, R. Rietkerk, Automatic spin-entangled decays of heavy resonances in Monte Carlo simulations, JHEP 03 (2013) 015. doi:10.1007/JHEP03(2013)015. arXiv:1212.3460.

[102] A. Ballestrero, E. Maina, G. Pelliccioli, W boson polarization in vector boson scattering at the LHC, JHEP 03 (2018) 170. doi:10.1007/JHEP03(2018)170. arXiv:1710.09339.

[103] A. Ballestrero, E. Maina, G. Pelliccioli, Polarized vector boson scattering in the fully leptonic WZ and ZZ channels at the LHC, JHEP 09 (2019) 087. doi:10.1007/JHEP09(2019)087. arXiv:1907.04722.

[104] CMS collaboration, Study of $W^{\pm}W^{\pm}$ production via vector boson scattering at the HL-LHC with the upgraded CMS detector (2018). URL:

50

http://cds.cern.ch/record/2646870.

[105] High-Luminosity Large Hadron Collider (HL-LHC): Technical Design Report V. 0.1 4/2017 (2017). doi:10.23731/CYRM-2017-004.

[106] A. Dainese, M. Mangano, A. B. Meyer, A. Nisati, G. Salam, M. A. Vesterinen (Eds.), Report on the Physics at the HL-LHC,and Perspectives for the HE-LHC, volume 7/2019 of *CERN Yellow Reports: Monographs*, CERN, Geneva, Switzerland, 2019. doi:10.23731/CYRM-2019-007.

[107] CMS collaboration, Prospects for the measurement of electroweak and polarized WZ to 3lv production cross sections at the High-Luminosity LHC, Technical Report CMS-PAS-FTR-18-038, 2018. URL: http://cds.cern.ch/record/2650774.

[108] CMS collaboration, Vector Boson Scattering prospective studies in the ZZ fully leptonic decay channel for the High-Luminosity and High-Energy LHC upgrades, Technical Report CMS-PAS-FTR-18-014, 2018. URL: http://cds.cern.ch/record/2650915.

[109] ATLAS collaboration, Studies on the impact of an extended Inner Detector tracker and a forward muon tagger on $W^{\pm}W^{\pm}$ scattering in pp collisions at the High-Luminosity LHC with the ATLAS experiment, ATL-PHYS-PUB-2017-023 (2017). URL: https://cds.cern.ch/record/2298958.

[110] ATLAS collaboration, Prospective study of vector boson scattering in WZ fully leptonic final state at HL-LHC, ATL-PHYS-PUB-2018-023 (2018). URL: https://cds.cern.ch/record/2645271.

[111] G. Aad, et al. (ATLAS collaboration), The ATLAS Experiment at the CERN Large Hadron Collider, JINST 3 (2008) S08003. doi:10.1088/1748-0221/3/08/S08003.

[112] ATLAS collaboration, Prospects for the measurement of the $W^{\pm}W^{\pm}$ scattering cross section and extraction of the longitudinal scattering component in pp collisions at the High-Luminosity LHC with the AT-LAS experiment, ATL-PHYS-PUB-2018-052 (2018). URL: http://cds.cern.ch/record/2652447.

[113] ATLAS collaboration, Technical Design Report: A High-Granularity Timing Detector for the ATLAS Phase-II Upgrade, Technical Report CERN-LHCC-2020-007, ATLAS-TDR-031, CERN, Geneva, 2020. URL: https://cds.cern.ch/record/2719855.

[114] ATLAS collaboration, Studies of Vector Boson Scattering And Triboson Production with an Upgraded ATLAS Detector at a High-Luminosity LHC, ATL-PHYS-PUB-2013-006 (2013). URL: http://cds.cern.ch/record/1558703.

[115] J. Kalinowski, P. Kozów, S. Pokorski, J. Rosiek, M. Szleper, S. Tkaczyk, Same-sign WW scattering at the LHC: can we discover BSM effects before discovering new states?, Eur. Phys. J. C 78 (2018) 403. doi:10.1140/epjc/s10052-018-5885-y. arXiv:1802.02366.

[116] R. Gomez-Ambrosio, Studies of Dimension-Six EFT effects in Vector Boson Scattering, Eur. Phys. J. C 79 (2019) 389. doi:10.1140/epjc/s10052-019-6893-2. arXiv:1809.04189.

[117] J. Y. Araz, S. Banerjee, R. S. Gupta, M. Spannowsky, Precision SMEFT bounds from the VBF Higgs at high transverse momentum, JHEP 04 (2021) 125. doi:10.1007/JHEP04(2021)125. arXiv:2011.03555.

[118] A. Dedes, P. Kozów, M. Szleper, SM EFT effects in Vector-Boson Scattering at the LHC (2020). arXiv:2011.07367.

[119] J. Ellis, M. Madigan, K. Mimasu, V. Sanz, T. You, Top, Higgs, Diboson and Electroweak Fit to the Standard Model Effective Field Theory (2020). arXiv:2012.02779.

[120] J. J. Ethier, R. Gomez-Ambrosio, G. Magni, J. Rojo, SMEFT analysis of vector boson scattering and diboson data from the LHC Run II (2021). arXiv:2101.03180.

[121] R. L. Delgado, A. Dobado, D. Espriu, C. Garcia-Garcia, M. J. Herrero, X. Marcano, J. J. Sanz-Cillero, Production of vector resonances at the LHC via WZ-scattering: a unitarized EChL analysis, JHEP 11 (2017) 098. doi:10.1007/JHEP11(2017)098. arXiv:1707.04580.

[122] R. L. Delgado, A. Dobado, D. Espriu, C. Garcia-Garcia, M. J. Herrero, X. Marcano, J. J. Sanz-Cillero, Collider phenomenology of vector resonances in WZ scattering processes, PoS Confinement2018 (2019) 220. doi:10.22323/1.336.0220. arXiv:1811.08720.

[123] R. L. Delgado, C. Garcia-Garcia, M. J. Herrero, Dynamical vector resonances from the EChL in VBS at the LHC: the WW case, JHEP 11 (2019) 065. doi:10.1007/JHEP11(2019)065. arXiv:1907.11957.

[124] B. Grzadkowski, M. Iskrzynski, M. Misiak, J. Rosiek, Dimension-Six Terms in the Standard Model Lagrangian, JHEP 10 (2010) 085. doi:10.1007/JHEP10(2010)085. arXiv:1008.4884.

[125] J. Ellis, C. W. Murphy, V. Sanz, T. You, Updated Global SMEFT Fit to Higgs, Diboson and Electroweak Data, JHEP 06 (2018) 146. doi:10.1007/JHEP06(2018)146. arXiv:1803.03252.

[126] S. Dawson, S. Homiller, S. D. Lane, Putting standard model EFT fits to work, Phys. Rev. D 102 (2020) 055012. doi:10.1103/PhysRevD.102.055012. arXiv:2007.01296.

[127] O. Domenech, A. Pomarol, J. Serra, Probing the SM with Dijets at the LHC, Phys. Rev. D 85 (2012) 074030. doi:10.1103/PhysRevD.85.074030. arXiv:1201.6510.

[128] Q. R. Ahmad, et al. (SNO collaboration), Direct evidence for neutrino flavor transformation from neutral current interactions in the Sudbury Neutrino Observatory, Phys. Rev. Lett. 89 (2002) 011301. doi:10.1103/PhysRevLett.89.011301. arXiv:nucl-ex/0204008.

[129] Y. Ashie, et al. (Super-Kamiokande collaboration), A Measurement of atmospheric neutrino oscillation parameters by SUPER-KAMIOKANDE I, Phys. Rev. D 71 (2005) 112005. doi:10.1103/PhysRevD.71.112005. arXiv:hep-ex/0501064.

[130] E. Ma, Pathways to naturally small neutrino masses, Phys. Rev. Lett. 81 (1998) 1171–1174. doi:10.1103/PhysRevLett.81.1171. arXiv:hep-ph/9805219.

[131] Y. Cai, J. Herrero-García, M. A. Schmidt, A. Vicente, R. R. Volkas, From the trees to the forest: a review of radiative neutrino mass models, Front. in Phys. 5 (2017) 63. doi:10.3389/fphy.2017.00063. arXiv:1706.08524.

[132] Y. Cai, T. Han, T. Li, R. Ruiz, Lepton Number Violation: Seesaw Models and Their Collider Tests, Front. in Phys. 6 (2018) 40. doi:10.3389/fphy.2018.00040. arXiv:1711.02180.

[133] A. M. Sirunyan, et al. (CMS collaboration), Search for heavy neutral leptons in events with three charged leptons in proton-proton collisions at $\sqrt{s}$ = 13 TeV, Phys. Rev. Lett. 120 (2018) 221801. doi:10.1103/PhysRevLett.120.221801. arXiv:1802.02965.

[134] A. M. Sirunyan, et al. (CMS collaboration), Search for heavy Majorana neutrinos in same-sign dilepton channels in proton-proton collisions at $\sqrt{s}$ = 13 TeV, JHEP 01 (2019) 122. doi:10.1007/JHEP01(2019)122. arXiv:1806.10905.

[135] G. Aad, et al. (ATLAS collaboration), Search for a Charged Higgs Boson Produced in the Vector-Boson Fusion Mode with Decay $H^{\pm} \to W^{\pm}Z$ using pp Collisions at $\sqrt{s}$ = 8 TeV with the ATLAS Experiment, Phys. Rev. Lett. 114 (2015) 231801. doi:10.1103/PhysRevLett.114.231801. arXiv:1503.04233.

[136] F. del Aguila, J. A. Aguilar-Saavedra, Distinguishing seesaw models at LHC with multi-lepton signals, Nucl. Phys. B 813 (2009) 22–90. doi:10.1016/j.nuclphysb.2008.12.029. arXiv:0808.2468.

[137] A. Atre, T. Han, S. Pascoli, B. Zhang, The Search for Heavy Majorana Neutrinos, JHEP 05 (2009) 030. doi:10.1088/1126-6708/2009/05/030. arXiv:0901.3589.

[138] F. F. Deppisch, P. S. Bhupal Dev, A. Pilaftsis, Neutrinos and Collider Physics, New J. Phys. 17 (2015) 075019. doi:10.1088/1367-2630/17/7/075019. arXiv:1502.06541.

[139] S. Pascoli, R. Ruiz, C. Weiland, Heavy neutrinos with dynamic jet vetoes: multilepton searches at $\sqrt{s}$ = 14 , 27, and 100 TeV, JHEP 06 (2019) 049. doi:10.1007/JHEP06(2019)049. arXiv:1812.08750.

[140] S. Weinberg, A Model of Leptons, Phys. Rev. Lett. 19 (1967) 1264–1266. doi:10.1103/PhysRevLett.19.1264.

[141] A. Pilaftsis, Radiatively induced neutrino masses and large Higgs neutrino couplings in the standard model with Majorana fields, Z. Phys. C 55 (1992) 275–282. doi:10.1007/BF01482590. arXiv:hep-ph/9901206.

[142] J. Kersten, A. Y. Smirnov, Right-Handed Neutrinos at CERN LHC and the Mechanism of Neutrino Mass Generation, Phys. Rev. D 76 (2007) 073005. doi:10.1103/PhysRevD.76.073005. arXiv:0705.3221.

[143] K. Moffat, S. Pascoli, C. Weiland, Equivalence between massless neutrinos and lepton number conservation in fermionic singlet extensions of the Standard Model (2017). arXiv:1712.07611.

[144] C. Degrande, O. Mattelaer, R. Ruiz, J. Turner, Fully-Automated Precision Predictions for Heavy Neutrino Production Mechanisms at Hadron Colliders, Phys. Rev. D 94 (2016) 053002. doi:10.1103/PhysRevD.94.053002. arXiv:1602.06957.

[145] D. A. Dicus, D. D. Karatas, P. Roy, Lepton nonconservation at supercollider energies, Phys. Rev. D 44 (1991) 2033–2037. doi:10.1103/

`PhysRevD.44.2033`.

[146] A. Datta, M. Guchait, A. Pilaftsis, Probing lepton number violation via majorana neutrinos at hadron supercolliders, Phys. Rev. D 50 (1994) 3195–3203. doi:`10.1103/PhysRevD.50.3195`. `arXiv:hep-ph/9311257`.

[147] P. S. B. Dev, A. Pilaftsis, U.-k. Yang, New Production Mechanism for Heavy Neutrinos at the LHC, Phys. Rev. Lett. 112 (2014) 081801. doi:`10.1103/PhysRevLett.112.081801`. `arXiv:1308.2209`.

[148] D. Alva, T. Han, R. Ruiz, Heavy Majorana neutrinos from $W\gamma$ fusion at hadron colliders, JHEP 02 (2015) 072. doi:`10.1007/JHEP02(2015)072`. `arXiv:1411.7305`.

[149] S. Pascoli, R. Ruiz, C. Weiland, Safe Jet Vetoes, Phys. Lett. B 786 (2018) 106–113. doi:`10.1016/j.physletb.2018.08.060`. `arXiv:1805.09335`.

[150] A. Flórez, K. Gui, A. Gurrola, C. Patiño, D. Restrepo, Expanding the Reach of Heavy Neutrino Searches at the LHC, Phys. Lett. B 778 (2018) 94–100. doi:`10.1016/j.physletb.2018.01.009`. `arXiv:1708.03007`.

[151] M. Magg, C. Wetterich, Neutrino Mass Problem and Gauge Hierarchy, Phys. Lett. B 94 (1980) 61–64. doi:`10.1016/0370-2693(80)90825-4`.

[152] J. Schechter, J. W. F. Valle, Neutrino Masses in SU(2) x U(1) Theories, Phys. Rev. D 22 (1980) 2227. doi:`10.1103/PhysRevD.22.2227`.

[153] T. P. Cheng, L.-F. Li, Neutrino Masses, Mixings and Oscillations in SU(2) x U(1) Models of Electroweak Interactions, Phys. Rev. D 22 (1980) 2860. doi:`10.1103/PhysRevD.22.2860`.

[154] R. N. Mohapatra, G. Senjanovic, Neutrino Masses and Mixings in Gauge Models with Spontaneous Parity Violation, Phys. Rev. D 23 (1981) 165. doi:`10.1103/PhysRevD.23.165`.

[155] G. Lazarides, Q. Shafi, C. Wetterich, Proton Lifetime and Fermion Masses in an SO(10) Model, Nucl. Phys. B 181 (1981) 287–300. doi:`10.1016/0550-3213(81)90354-0`.

[156] S. Parke, M. Ross-Lonergan, Unitarity and the three flavor neutrino mixing matrix, Phys. Rev. D 93 (2016) 113009. doi:`10.1103/PhysRevD.93.113009`. `arXiv:1508.05095`.

[157] S. A. R. Ellis, K. J. Kelly, S. W. Li, Leptonic Unitarity Triangles, Phys. Rev. D 102 (2020) 115027. doi:`10.1103/PhysRevD.102.115027`. `arXiv:2004.13719`.

[158] M. Muhlleitner, M. Spira, A Note on doubly charged Higgs pair production at hadron colliders, Phys. Rev. D 68 (2003) 117701. doi:`10.1103/PhysRevD.68.117701`. `arXiv:hep-ph/0305288`.

[159] I. Brivio, M. Trott, The Standard Model as an Effective Field Theory, Phys. Rept. 793 (2019) 1–98. doi:`10.1016/j.physrep.2018.11.002`. `arXiv:1706.08945`.

[160] I. Brivio, Y. Jiang, M. Trott, The SMEFTsim package, theory and tools, JHEP 12 (2017) 070. doi:`10.1007/JHEP12(2017)070`. `arXiv:1709.06492`.

[161] S. Weinberg, Baryon and Lepton Nonconserving Processes, Phys. Rev. Lett. 43 (1979) 1566–1570. doi:`10.1103/PhysRevLett.43.1566`.

[162] F. Bonnet, M. Hirsch, T. Ota, W. Winter, Systematic study of the d=5 Weinberg operator at one-loop order, JHEP 07 (2012) 153. doi:`10.1007/JHEP07(2012)153`. `arXiv:1204.5862`.

[163] M. Agostini, et al. (GERDA collaboration), Final Results of GERDA on the Search for Neutrinoless Double-β Decay, Phys. Rev. Lett. 125 (2020) 252502. doi:`10.1103/PhysRevLett.125.252502`. `arXiv:2009.06079`.

[164] A. Atre, V. Barger, T. Han, Upper bounds on lepton-number violating processes, Phys. Rev. D 71 (2005) 113014. doi:`10.1103/PhysRevD.71.113014`. `arXiv:hep-ph/0502163`.

[165] D. Contardo, A. Ball, et al. (CMS collaboration), The Phase-2 Upgrade of the CMS Endcap Calorimeter, Technical Report CERN-LHCC-2017-023, CMS-TDR-019, CERN, Geneva, 2017. URL: `http://cds.cern.ch/record/2293646`.

[166] A. M. Sirunyan, et al. (CMS collaboration), Particle-flow reconstruction and global event description with the CMS detector, JINST 12 (2017) P10003. doi:`10.1088/1748-0221/12/10/P10003`. `arXiv:1706.04965`.

[167] K. Kimmo, Quantitative Comparison of Deep Neural Networks for Quark/Gluon Jet Discrimination, 2019. URL: `http://urn.fi/URN:NBN:fi-fe201902286674`.

[168] J. Duarte, et al., Fast inference of deep neural networks in FPGAs for particle physics, JINST 13 (2018) P07027. doi:`10.1088/1748-0221/13/07/P07027`. `arXiv:1804.06913`.

[169] V. Loncar, et al., Compressing deep neural networks on FPGAs to binary and ternary precision with HLS4ML (2020). `arXiv:2003.06308`.

[170] C. N. Coelho, A. Kuusela, S. Li, H. Zhuang, T. Aarrestad, V. Loncar, J. Ngadiuba, M. Pierini, A. A. Pol, S. Summers, Automatic deep heterogeneous quantization of Deep Neural Networks for ultra low-area, low-latency inference on the edge at particle colliders (2020). `arXiv:2006.10159`.

[171] T. Aarrestad, et al., Fast convolutional neural networks on FPGAs with hls4ml (2021). `arXiv:2101.05108`.

[172] V. Khachatryan, et al. (CMS collaboration), Identification techniques for highly boosted W bosons that decay into hadrons, JHEP 12 (2014) 017. doi:`10.1007/JHEP12(2014)017`. `arXiv:1410.4227`.

[173] J. De Boer, A Deep Neural Network capable of discriminating between jets coming from the decay of longitudinally and transversely polarized W or Z bosons with a large Lorentz boost, CERN-STUDENTS-Note-2018-220 (2018). URL: `https://cds.cern.ch/record/2650187`.

[174] B. Henning, D. Lombardo, M. Riembau, F. Riva, Measuring Higgs Couplings without Higgs Bosons, Phys. Rev. Lett. 123 (2019) 181801. doi:`10.1103/PhysRevLett.123.181801`. `arXiv:1812.09299`.

[175] A. Azatov, R. Contino, C. S. Machado, F. Riva, Helicity selection rules and noninterference for BSM amplitudes, Phys. Rev. D 95 (2017) 065014. doi:`10.1103/PhysRevD.95.065014`. `arXiv:1607.05236`.

[176] R. Franceschini, G. Panico, A. Pomarol, F. Riva, A. Wulzer, Electroweak Precision Tests in High-Energy Diboson Processes, JHEP 02 (2018) 111. doi:`10.1007/JHEP02(2018)111`. `arXiv:1712.01310`.

[177] G. Panico, F. Riva, A. Wulzer, Diboson interference resurrection, Phys. Lett. B 776 (2018) 473–480. doi:`10.1016/j.physletb.2017.11.068`. `arXiv:1708.07823`.

[178] J. M. Butterworth, A. R. Davison, M. Rubin, G. P. Salam, Jet substructure as a new Higgs search channel at the LHC, Phys. Rev. Lett. 100 (2008) 242001. doi:`10.1103/PhysRevLett.100.242001`. `arXiv:0802.2470`.

[179] A. M. Sirunyan, et al. (CMS collaboration), Identification of heavy-flavour jets with the CMS detector in pp collisions at 13 TeV, JINST 13 (2018) P05011. doi:`10.1088/1748-0221/13/05/P05011`. `arXiv:1712.07158`.

[180] J. Thaler, K. Van Tilburg, Identifying Boosted Objects with N-subjettiness, JHEP 03 (2011) 015. doi:`10.1007/JHEP03(2011)015`. `arXiv:1011.2268`.

[181] A. J. Larkoski, I. Moult, B. Nachman, Jet Substructure at the Large Hadron Collider: A Review of Recent Advances in Theory and Machine Learning, Phys. Rept. 841 (2020) 1–63. doi:`10.1016/j.physrep.2019.11.001`. `arXiv:1709.04464`.

[182] R. Kogler, et al., Jet Substructure at the Large Hadron Collider: Experimental Review, Rev. Mod. Phys. 91 (2019) 045003. doi:`10.1103/RevModPhys.91.045003`. `arXiv:1803.06991`.

[183] S. Marzani, G. Soyez, M. Spannowsky, Looking inside jets: an introduction to jet substructure and boosted-object phenomenology, volume 958, Springer, 2019. doi:`10.1007/978-3-030-15709-8`. `arXiv:1901.10342`.

[184] A. J. Larkoski, S. Marzani, G. Soyez, J. Thaler, Soft Drop, JHEP 05 (2014) 146. doi:`10.1007/JHEP05(2014)146`. `arXiv:1402.2657`.

[185] E. A. Moreno, O. Cerri, J. M. Duarte, H. B. Newman, T. Q. Nguyen, A. Periwal, M. Pierini, A. Serikova, M. Spiropulu, J.-R. Vlimant, JEDI-net: a jet identification algorithm based on interaction networks, Eur. Phys. J. C 80 (2020) 58. doi:`10.1140/epjc/s10052-020-7608-4`. `arXiv:1908.05318`.

[186] H. Qu, L. Gouskos, ParticleNet: Jet Tagging via Particle Clouds, Phys. Rev. D 101 (2020) 056019. doi:`10.1103/PhysRevD.101.056019`. `arXiv:1902.08570`.

[187] M. Grossi, J. Novak, B. Kersevan, D. Rebuzzi, Comparing traditional and deep-learning techniques of kinematic reconstruction for polarization discrimination in vector boson scattering, Eur. Phys. J. C 80 (2020) 1144. doi:`10.1140/epjc/s10052-020-08713-1`. `arXiv:2008.05316`.

[188] G. Aad, et al. (ATLAS collaboration), Evidence for electroweak production of two jets in association with a $Z\gamma$ pair in pp collisions at $\sqrt{s} = 13$ TeV with the ATLAS detector, Phys. Lett. B 803 (2020) 135341. doi:`10.1016/j.physletb.2020.135341`. `arXiv:1910.09503`.

[189] J. Li, S. Yang, R. Zhang, Detecting anomaly in vector boson scattering (2020). arXiv:2010.13281.

[190] T. Han, D. Krohn, L.-T. Wang, W. Zhu, New Physics Signals in Longitudinal Gauge Boson Scattering at the LHC, JHEP 03 (2010) 082. doi:10.1007/JHEP03(2010)082. arXiv:0911.3656.

[191] E. Maina, Vector boson polarizations in the decay of the Standard Model Higgs (2020). arXiv:2007.12080.

[192] S. De, V. Rentala, W. Shepherd, Measuring the polarization of boosted, hadronic W bosons with jet substructure observables (2020). arXiv:2008.04318.

[193] J. Searcy, L. Huang, M.-A. Pleier, J. Zhu, Determination of the WW polarization fractions in $pp \rightarrow W^\pm W^\pm jj$ using a deep machine learning technique, Phys. Rev. D 93 (2016) 094033. doi:10.1103/PhysRevD.93.094033. arXiv:1510.01691.

[194] J. Lee, N. Chanon, A. Levin, J. Li, M. Lu, Q. Li, Y. Mao, Polarization fraction measurement in same-sign WW scattering using deep learning, Phys. Rev. D 99 (2019) 033004. doi:10.1103/PhysRevD.99.033004. arXiv:1812.07591.

[195] J. Lee, N. Chanon, A. Levin, J. Li, M. Lu, Q. Li, Y. Mao, Polarization fraction measurement in ZZ scattering using deep learning, Phys. Rev. D 100 (2019) 116010. doi:10.1103/PhysRevD.100.116010. arXiv:1908.05196.

[196] A. Vaswani, N. Shazeer, N. Parmar, J. Uszkoreit, L. Jones, A. N. Gomez, L. Kaiser, I. Polosukhin, Attention is all you need, 2017. arXiv:1706.03762.

[197] G. F. Giudice, C. Grojean, A. Pomarol, R. Rattazzi, The Strongly-Interacting Light Higgs, JHEP 06 (2007) 045. doi:10.1088/1126-6708/2007/06/045. arXiv:hep-ph/0703164.

[198] R. Contino, M. Ghezzi, C. Grojean, M. Muhlleitner, M. Spira, Effective Lagrangian for a light Higgs-like scalar, JHEP 07 (2013) 035. doi:10.1007/JHEP07(2013)035. arXiv:1303.3876.

[199] S. Jung, J. Lee, M. Perelló, J. Tian, M. Vos, Higgs, top and electroweak precision measurements at future e^+e^- colliders; a combined effective field theory analysis with renormalization mixing (2020). arXiv:2006.14631.

[200] M. Aoki, S. Kanemura, K. Tsumura, K. Yagyu, Models of Yukawa interaction in the two Higgs doublet model, and their collider phenomenology, Phys. Rev. D 80 (2009) 015017. doi:10.1103/PhysRevD.80.015017. arXiv:0902.4665.

[201] M. Aaboud, et al. (ATLAS collaboration), Combination of searches for heavy resonances decaying into bosonic and leptonic final states using 36 fb^{-1} of proton-proton collision data at $\sqrt{s} = 13$ TeV with the ATLAS detector, Phys. Rev. D 98 (2018) 052008. doi:10.1103/PhysRevD.98.052008. arXiv:1808.02380.

[202] A. M. Sirunyan, et al. (CMS collaboration), Search for a heavy Higgs boson decaying to a pair of W bosons in proton-proton collisions at $\sqrt{s} = 13$ TeV, JHEP 03 (2020) 034. doi:10.1007/JHEP03(2020)034. arXiv:1912.01594.

[203] D. Contardo, M. Klute, J. Mans, L. Silvestris, J. Butler, et al. (CMS collaboration), Technical Proposal for the Phase-II Upgrade of the CMS Detector, Technical Report CERN-LHCC-2015-010, LHCC-P-008, CMS-TDR-15-02, 2015. URL: https://cds.cern.ch/record/2020886.

[204] Technical proposal for a MIP timing detector in the CMS experiment Phase-2 upgrade, Technical Report, CERN, Geneva, 2017. URL: https://cds.cern.ch/record/2296612.

[205] J. N. Butler, T. Tabarelli de Fatis, et al. (CMS collaboration), A MIP Timing Detector for the CMS Phase-2 Upgrade, Technical Report CERN-LHCC-2019-003, CMS-TDR-020, 2019. URL: https://cds.cern.ch/record/2667167.

[206] G. Apollinari, I. Béjar Alonso, O. Brüning, M. Lamont, L. Rossi, High-Luminosity Large Hadron Collider (HL-LHC): Preliminary Design Report (2015). URL: https://cds.cern.ch/record/2116337. doi:10.5170/CERN-2015-005.

[207] ATLAS collaboration, Letter of Intent for the Phase-II Upgrade of the ATLAS Experiment, Technical Report LHCC-I-023, CERN-LHCC-2012-022, 2012. URL: https://cds.cern.ch/record/1502664.

[208] S. Paoletti (CMS collaboration), The CMS Tracker Upgrade for the High Luminosity LHC, Technical Report, CERN, Geneva, 2019. URL: http://cds.cern.ch/record/2723307.

[209] A. Tumasyan, et al. (CMS collaboration), The Phase-2 Upgrade of the CMS Tracker, Technical Report CERN-LHCC-2017-009, CMS-TDR-014, 2017. URL: https://cds.cern.ch/record/2272264.

[210] CMS collaboration, The Phase-2 Upgrade of the CMS Barrel Calorimeters, Technical Report CERN-LHCC-2017-011, CMS-TDR-015, CERN, Geneva, 2017. URL: https://cds.cern.ch/record/2283187.

[211] N. Marinelli (CMS collaboration), The CMS ECAL Upgrade for High Precision Timing and Energy Measurements at HL-LHC, PoS Lepton-Photon2019 (2019) 097. doi:10.22323/1.367.0097.

[212] CMS collaboration, CMS ECAL Laser monitoring up to 2017, $\pi^0/\eta \rightarrow \gamma\gamma$ spectrum and monitoring, ES calibration, Technical Report CERN-CMS-DP-2017-023, CERN, Geneva, 2017. URL: https://cds.cern.ch/record/2273269.

[213] C. Ochando (CMS collaboration), HGCAL: A High-Granularity Calorimeter for the endcaps of CMS at HL-LHC, J. Phys. Conf. Ser. 928 (2017) 012025. doi:10.1088/1742-6596/928/1/012025.

[214] T. Hebbeker, A. Korytov (CMS collaboration), The Phase-2 Upgrade of the CMS Muon Detectors (2017).

[215] M. Dong, et al. (CEPC Study Group collaboration), CEPC Conceptual Design Report: Volume 2 - Physics & Detector (2018). arXiv:1811.10545.

[216] A. Abada, et al. (FCC collaboration), FCC-ee: The Lepton Collider: Future Circular Collider Conceptual Design Report Volume 2, Eur. Phys. J. ST 228 (2019) 261–623. doi:10.1140/epjst/e2019-900045-4.

[217] The International Linear Collider Technical Design Report - Volume 2: Physics (2013). arXiv:1306.6352.

[218] H. Abramowicz, et al., The International Linear Collider Technical Design Report - Volume 4: Detectors (2013). arXiv:1306.6329.

[219] Physics and Detectors at CLIC: CLIC Conceptual Design Report (2012). doi:10.5170/CERN-2012-003. arXiv:1202.5940.

[220] A Multi-TeV Linear Collider Based on CLIC Technology: CLIC Conceptual Design Report (2012). doi:10.5170/CERN-2012-007.

[221] Proposal for the ILC Preparatory Laboratory (Pre-lab) (2021). doi:10.5281/zenodo.4742043. arXiv:2106.00602.

[222] M. Idzik (FCAL collaboration), FCAL R&D on Forward Calorimeters, Acta Phys. Polon. B 46 (2015) 1297–1308. doi:10.5506/APhysPolB.46.1297.

[223] J. S. Marshall, A. Münnich, M. A. Thomson, Performance of Particle Flow Calorimetry at CLIC, Nucl. Instrum. Meth. A 700 (2013) 153–162. doi:10.1016/j.nima.2012.10.038. arXiv:1209.4039.

[224] C. Fleper, W. Kilian, J. Reuter, M. Sekulla, Scattering of W and Z Bosons at High-Energy Lepton Colliders, Eur. Phys. J. C 77 (2017) 120. doi:10.1140/epjc/s10052-017-4656-5. arXiv:1607.03030.

[225] J. F. Gunion, A. Tofighi-Niaki, Heavy Higgs Production and W^-W^+ Scattering Processes in e^-e^+ Collisions at High-energy, Phys. Rev. D 36 (1987) 2671. doi:10.1103/PhysRevD.36.2671.

[226] A. Tofighi-Niaki, J. F. Gunion, Heavy Higgs Production and Vector Boson Scattering Processes in e^+e^- Collisions at High-energy, Phys. Rev. D 38 (1988) 1433. doi:10.1103/PhysRevD.38.1433.

[227] V. D. Barger, K.-m. Cheung, T. Han, R. J. N. Phillips, Probing strongly interacting electroweak dynamics through W^+W^-/ZZ ratios at future e^+e^- colliders, Phys. Rev. D 52 (1995) 3815–3825. doi:10.1103/PhysRevD.52.3815. arXiv:hep-ph/9501379.

[228] T. Han, H.-J. He, C. P. Yuan, Quartic gauge boson couplings at linear colliders: Interplay of WWZ/ZZZ production and WW fusion, Phys. Lett. B 422 (1998) 294–304. doi:10.1016/S0370-2693(98)00052-5. arXiv:hep-ph/9711429.

[229] E. Boos, H. J. He, W. Kilian, A. Pukhov, C. P. Yuan, P. M. Zerwas, Strongly interacting vector bosons at TeV e+ e- linear colliders, Phys. Rev. D 57 (1998) 1553. doi:10.1103/PhysRevD.57.1553. arXiv:hep-ph/9708310.

[230] E. Boos, H. J. He, W. Kilian, A. Pukhov, C. P. Yuan, P. M. Zerwas, Strongly interacting vector bosons at TeV e+- e- linear colliders: Addendum, Phys. Rev. D 61 (2000) 077901. doi:10.1103/PhysRevD.61.077901. arXiv:hep-ph/9908409.

[231] T. Abe, et al. (Linear Collider American Working Group collaboration), Linear Collider Physics Resource Book for Snowmass 2001 - Part 3: Studies of Exotic and Standard Model Physics (2001). arXiv:hep-ex/0106057.

[232] A. Denner, S. Dittmaier, T. Hahn, Radiative corrections to $ZZ \rightarrow ZZ$ in the electroweak standard model, Phys. Rev. D 56 (1997) 117–134.

doi:10.1103/PhysRevD.56.117. arXiv:hep-ph/9612390.

[233] A. Denner, T. Hahn, Radiative corrections to $W^+W^- \to W^+W^-$ in the electroweak standard model, Nucl. Phys. B 525 (1998) 27–50. doi:10.1016/S0550-3213(98)00287-9. arXiv:hep-ph/9711302.

[234] S. Liebler, G. Moortgat-Pick, G. Weiglein, Off-shell effects in Higgs processes at a linear collider and implications for the LHC, JHEP 06 (2015) 093. doi:10.1007/JHEP06(2015)093. arXiv:1502.07970.

[235] D. Dominici, Tests for a strong electroweak sector at future e^+e^- high-energy colliders, Riv. Nuovo Cim. 20N11 (1997) 1–64. doi:10.1007/BF02877375. arXiv:hep-ph/9711385.

[236] W. Kilian, Strongly interacting W bosons at e- e- colliders, Int. J. Mod. Phys. A 15 (2000) 2387–2396. doi:10.1016/S0217-751X(00)00245-5.

[237] R. Chierici, S. Rosati, M. Kobel, Strong electroweak symmetry breaking signals in w w scattering at tesla, AIP Conf. Proc. 578 (2001) 544–549. doi:10.1063/1.1394378.

[238] S. Rosati, Study of triple and quartic gauge couplings in e^+e^- collisions between 180 and 800 GeV, Ph.D. thesis, Bonn U., 2002.

[239] M. Beyer, W. Kilian, P. Krstonosic, K. Monig, J. Reuter, E. Schmidt, H. Schroder, Determination of New Electroweak Parameters at the ILC - Sensitivity to New Physics, Eur. Phys. J. C 48 (2006) 353–388. doi:10.1140/epjc/s10052-006-0038-0. arXiv:hep-ph/0604048.

[240] W. Kilian, T. Ohl, J. Reuter, WHIZARD: Simulating Multi-Particle Processes at LHC and ILC, Eur. Phys. J. C 71 (2011) 1742. doi:10.1140/epjc/s10052-011-1742-y. arXiv:0708.4233.

[241] S. Brass, W. Kilian, J. Reuter, Parallel Adaptive Monte Carlo Integration with the Event Generator WHIZARD, Eur. Phys. J. C 79 (2019) 344. doi:10.1140/epjc/s10052-019-6840-2. arXiv:1811.09711.

[242] A. Alboteanu, W. Kilian, J. Reuter, Resonances and Unitarity in Weak Boson Scattering at the LHC, JHEP 11 (2008) 010. doi:10.1088/1126-6708/2008/11/010. arXiv:0806.4145.

[243] W. Kilian, T. Ohl, J. Reuter, M. Sekulla, High-Energy Vector Boson Scattering after the Higgs Discovery, Phys. Rev. D 91 (2015) 096007. doi:10.1103/PhysRevD.91.096007. arXiv:1408.6207.

[244] S. Brass, C. Fleper, W. Kilian, J. Reuter, M. Sekulla, Transversal Modes and Higgs Bosons in Electroweak Vector-Boson Scattering at the LHC, Eur. Phys. J. C 78 (2018) 931. doi:10.1140/epjc/s10052-018-6398-4. arXiv:1807.02512.

[245] G. Aad, et al. (ATLAS collaboration), Observation of a new particle in the search for the Standard Model Higgs boson with the ATLAS detector at the LHC, Phys. Lett. B 716 (2012) 1–29. doi:10.1016/j.physletb.2012.08.020. arXiv:1207.7214.

[246] S. Chatrchyan, et al. (CMS collaboration), Observation of a New Boson at a Mass of 125 GeV with the CMS Experiment at the LHC, Phys. Lett. B 716 (2012) 30–61. doi:10.1016/j.physletb.2012.08.021. arXiv:1207.7235.

[247] J. P. Delahaye, M. Diemoz, K. Long, B. Mansoulié, N. Pastrone, L. Rivkin, D. Schulte, A. Skrinsky, A. Wulzer, Muon Colliders (2019). arXiv:1901.06150.

[248] A. Abada, et al. (FCC collaboration), FCC-hh: The Hadron Collider: Future Circular Collider Conceptual Design Report Volume 3, Eur. Phys. J. ST 228 (2019) 755–1107. doi:10.1140/epjst/e2019-900087-0.

[249] J. Tang, et al., Concept for a Future Super Proton-Proton Collider (2015). arXiv:1507.03224.

[250] J. Chen, T. Han, B. Tweedie, Electroweak Splitting Functions and High Energy Showering, JHEP 11 (2017) 093. doi:10.1007/JHEP11(2017)093. arXiv:1611.00788.

[251] C. W. Bauer, N. Ferland, B. R. Webber, Standard Model Parton Distributions at Very High Energies, JHEP 08 (2017) 036. doi:10.1007/JHEP08(2017)036. arXiv:1703.08562.

[252] C. W. Bauer, B. R. Webber, Polarization Effects in Standard Model Parton Distributions at Very High Energies, JHEP 03 (2019) 013. doi:10.1007/JHEP03(2019)013. arXiv:1808.08831.

[253] T. Han, Y. Ma, K. Xie, High energy leptonic collisions and electroweak parton distribution functions, Phys. Rev. D 103 (2021) L031301. doi:10.1103/PhysRevD.103.L031301. arXiv:2007.14300.

[254] T. Han, Y. Ma, K. Xie, Quark and Gluon Contents of a Lepton at High Energies (2021). arXiv:2103.09844.

[255] C. W. Bauer, D. Provasoli, B. R. Webber, Standard Model Fragmentation Functions at Very High Energies, JHEP 11 (2018) 030. doi:10.1007/

[256] Y. L. Dokshitzer, Calculation of the Structure Functions for Deep Inelastic Scattering and e+ e- Annihilation by Perturbation Theory in Quantum Chromodynamics., Sov. Phys. JETP 46 (1977) 641–653.

[257] V. N. Gribov, L. N. Lipatov, Deep inelastic e p scattering in perturbation theory, Sov. J. Nucl. Phys. 15 (1972) 438–450.

[258] L. N. Lipatov, The parton model and perturbation theory, Yad. Fiz. 20 (1974) 181–198.

[259] G. Altarelli, G. Parisi, Asymptotic Freedom in Parton Language, Nucl. Phys. B 126 (1977) 298–318. doi:10.1016/0550-3213(77)90384-4.

[260] M. Drees, R. M. Godbole, Virtual photon structure functions and the parton content of the electron, Phys. Rev. D 50 (1994) 3124–3133. doi:10.1103/PhysRevD.50.3124. arXiv:hep-ph/9403229.

[261] M. Ciafaloni, P. Ciafaloni, D. Comelli, Bloch-Nordsieck violating electroweak corrections to inclusive TeV scale hard processes, Phys. Rev. Lett. 84 (2000) 4810–4813. doi:10.1103/PhysRevLett.84.4810. arXiv:hep-ph/0001142.

[262] G. L. Kane, W. W. Repko, W. B. Rolnick, The Effective W+-, Z0 Approximation for High-Energy Collisions, Phys. Lett. B 148 (1984) 367–372. doi:10.1016/0370-2693(84)90105-9.

[263] S. Dawson, The Effective W Approximation, Nucl. Phys. B 249 (1985) 42–60. doi:10.1016/0550-3213(85)90038-0.

[264] G. Cuomo, L. Vecchi, A. Wulzer, Goldstone Equivalence and High Energy Electroweak Physics, SciPost Phys. 8 (2020) 078. doi:10.21468/SciPostPhys.8.5.078. arXiv:1911.12366.

[265] R. Frederix, S. Frixione, S. Prestel, P. Torrielli, On the reduction of negative weights in MC@NLO-type matching procedures, JHEP 07 (2020) 238. doi:10.1007/JHEP07(2020)238. arXiv:2002.12716.

[266] K. Danziger, S. Höche, F. Siegert, Reducing negative weights in Monte Carlo event generation with Sherpa (2021). arXiv:2110.15211.

[267] J. R. Andersen, C. Gütschow, A. Maier, S. Prestel, A Positive Resampler for Monte Carlo events with negative weights, Eur. Phys. J. C 80 (2020) 1007. doi:10.1140/epjc/s10052-020-08548-w. arXiv:2005.09375.

[268] B. Nachman, J. Thaler, Neural resampler for Monte Carlo reweighting with preserved uncertainties, Phys. Rev. D 102 (2020) 076004. doi:10.1103/PhysRevD.102.076004. arXiv:2007.11586.

[269] B. Stienen, R. Verheyen, Phase Space Sampling and Inference from Weighted Events with Autoregressive Flows, SciPost Phys. 10 (2021) 038. doi:10.21468/SciPostPhys.10.2.038. arXiv:2011.13445.

[270] A. Butter, T. Plehn, R. Winterhalder, How to GAN Event Subtraction (2019). doi:10.21468/SciPostPhysCore.3.2.009. arXiv:1912.08824.

[271] C. Gao, J. Isaacson, C. Krause, i-flow: High-dimensional Integration and Sampling with Normalizing Flows, Mach. Learn. Sci. Tech. 1 (2020) 045023. doi:10.1088/2632-2153/abab62. arXiv:2001.05486.

[272] C. Gao, S. Höche, J. Isaacson, C. Krause, H. Schulz, Event Generation with Normalizing Flows, Phys. Rev. D 101 (2020) 076002. doi:10.1103/PhysRevD.101.076002. arXiv:2001.10028.

[273] E. Bothmann, T. Janßen, M. Knobbe, T. Schmale, S. Schumann, Exploring phase space with Neural Importance Sampling, SciPost Phys. 8 (2020) 069. doi:10.21468/SciPostPhys.8.4.069. arXiv:2001.05478.

[274] P. F. Monni, P. Nason, E. Re, M. Wiesemann, G. Zanderighi, MiNNLO$_{PS}$: a new method to match NNLO QCD to parton showers, JHEP 05 (2020) 143. doi:10.1007/JHEP05(2020)143. arXiv:1908.06987.

[275] D. Lombardi, M. Wiesemann, G. Zanderighi, Advancing MiNNLO$_{PS}$ to diboson processes: $Z\gamma$ production at NNLO+PS (2020). arXiv:2010.10478.

[276] M. Dasgupta, F. A. Dreyer, K. Hamilton, P. F. Monni, G. P. Salam, G. Soyez, Parton showers beyond leading logarithmic accuracy, Phys. Rev. Lett. 125 (2020) 052002. doi:10.1103/PhysRevLett.125.052002. arXiv:2002.11114.

[277] Z. Nagy, D. E. Soper, Summations of large logarithms by parton showers (2020). arXiv:2011.04773.

[278] J. R. Forshaw, J. Holguin, S. Plätzer, Building a consistent parton shower, JHEP 09 (2020) 014. doi:10.1007/JHEP09(2020)014. arXiv:2003.06400.

[279] H. T. Li, P. Skands, A framework for second-order parton showers, Phys.

Lett. B 771 (2017) 59–66. doi:`10.1016/j.physletb.2017.05.011`. `arXiv:1611.00013`.

[280] S. Höche, F. Krauss, S. Prestel, Implementing NLO DGLAP evolution in Parton Showers, JHEP 10 (2017) 093. doi:`10.1007/JHEP10(2017) 093`. `arXiv:1705.00982`.

[281] K. Hamilton, R. Medves, G. P. Salam, L. Scyboz, G. Soyez, Colour and logarithmic accuracy in final-state parton showers (2020). `arXiv:2011.10054`.

[282] Z. Nagy, D. E. Soper, Effects of subleading color in a parton shower, JHEP 07 (2015) 119. doi:`10.1007/JHEP07(2015)119`. `arXiv:1501.00778`.

[283] S. Plätzer, M. Sjodahl, J. Thorén, Color matrix element corrections for parton showers, JHEP 11 (2018) 009. doi:`10.1007/JHEP11(2018) 009`. `arXiv:1808.00332`.

[284] J. R. Forshaw, J. Holguin, S. Plätzer, Parton branching at amplitude level, JHEP 08 (2019) 145. doi:`10.1007/JHEP08(2019)145`. `arXiv:1905.08686`.

[285] J. Isaacson, S. Prestel, Stochastically sampling color configurations, Phys. Rev. D 99 (2019) 014021. doi:`10.1103/PhysRevD.99.014021`. `arXiv:1806.10102`.

[286] J. R. Christiansen, T. Sjöstrand, Weak Gauge Boson Radiation in Parton Showers, JHEP 04 (2014) 115. doi:`10.1007/JHEP04(2014)115`. `arXiv:1401.5238`.

[287] F. Krauss, P. Petrov, M. Schoenherr, M. Spannowsky, Measuring collinear W emissions inside jets, Phys. Rev. D 89 (2014) 114006. doi:`10.1103/PhysRevD.89.114006`. `arXiv:1403.4788`.

[288] R. Kleiss, R. Verheyen, Collinear electroweak radiation in antenna parton showers, Eur. Phys. J. C 80 (2020) 980. doi:`10.1140/epjc/ s10052-020-08510-w`. `arXiv:2002.09248`.

[289] E. Bothmann, D. Napoletano, Automated evaluation of electroweak Sudakov logarithms in Sherpa, Eur. Phys. J. C 80 (2020) 1024. doi:`10.1140/epjc/s10052-020-08596-2`. `arXiv:2006.14635`.

[290] C. W. Bauer, N. Ferland, Resummation of electroweak Sudakov logarithms for real radiation, JHEP 09 (2016) 025. doi:`10.1007/ JHEP09(2016)025`. `arXiv:1601.07190`.

[291] C. W. Bauer, N. L. Rodd, B. R. Webber, Dark Matter Spectra from the Electroweak to the Planck Scale (2020). `arXiv:2007.15001`.

[292] R. Ruiz, A. Costantini, F. Maltoni, O. Mattelaer, The Effective Vector Boson Approximation in High-Energy Muon Collisions (2021). `arXiv:2111.02442`.

[293] H. Brooks, C. T. Preuss, P. Skands, Sector Showers for Hadron Collisions, JHEP 07 (2020) 032. doi:`10.1007/JHEP07(2020)032`. `arXiv:2003.00702`.

[294] H. Contopanagos, E. Laenen, G. F. Sterman, Sudakov factorization and resummation, Nucl. Phys. B 484 (1997) 303–330. doi:`10.1016/ S0550-3213(96)00567-6`. `arXiv:hep-ph/9604313`.

[295] D. A. Kosower, Antenna factorization of gauge theory amplitudes, Phys. Rev. D 57 (1998) 5410–5416. doi:`10.1103/PhysRevD.57. 5410`. `arXiv:hep-ph/9710213`.

[296] D. A. Kosower, Antenna factorization in strongly ordered limits, Phys. Rev. D 71 (2005) 045016. doi:`10.1103/PhysRevD.71.045016`. `arXiv:hep-ph/0311272`.

[297] A. J. Larkoski, J. J. Lopez-Villarejo, P. Skands, Helicity-Dependent Showers and Matching with VINCIA, Phys. Rev. D 87 (2013) 054033. doi:`10.1103/PhysRevD.87.054033`. `arXiv:1301.0933`.

[298] N. Fischer, A. Lifson, P. Skands, Helicity Antenna Showers for Hadron Colliders, Eur. Phys. J. C 77 (2017) 719. doi:`10.1140/epjc/ s10052-017-5306-7`. `arXiv:1708.01736`.

[299] J. Chen, Electroweak Splitting Functions and High Energy Showering, Ph.D. thesis, U. Pittsburgh (main), 2017.

[300] J. Chen, On the Feynman Rules of Massive Gauge Theory in Physical Gauges (2019). `arXiv:1902.06738`.

[301] T. Sjöstrand, S. Ask, J. R. Christiansen, R. Corke, N. Desai, P. Ilten, S. Mrenna, S. Prestel, C. O. Rasmussen, P. Z. Skands, An introduction to PYTHIA 8.2, Comput. Phys. Commun. 191 (2015) 159–177. doi:`10. 1016/j.cpc.2015.01.024`. `arXiv:1410.3012`.

[302] A. Costantini, F. De Lillo, F. Maltoni, L. Mantani, O. Mattelaer, R. Ruiz, X. Zhao, Vector boson fusion at multi-TeV muon colliders, JHEP 09 (2020) 080. doi:`10.1007/JHEP09(2020)080`. `arXiv:2005.10289`.

[303] M. Lu, A. M. Levin, C. Li, A. Agapitos, Q. Li, F. Meng, S. Qian, J. Xiao, T. Yang, The physics case for an electron-muon collider,

[304] H. Al Ali, et al., The Muon Smasher's Guide (2021). `arXiv:2103.14043`.

[305] R. Franceschini, M. Greco, Higgs and BSM Physics at the future Muon Collider (2021). `arXiv:2104.05770`.

[306] R. Palmer, et al., Muon collider design, Nucl. Phys. B Proc. Suppl. 51 (1996) 61–84. doi:`10.1016/0920-5632(96)00417-3`. `arXiv:acc-phys/9604001`.

[307] C. M. Ankenbrandt, et al., Status of muon collider research and development and future plans, Phys. Rev. ST Accel. Beams 2 (1999) 081001. doi:`10.1103/PhysRevSTAB.2.081001`. `arXiv:physics/9901022`.

[308] R. Capdevilla, F. Meloni, R. Simoniello, J. Zurita, Hunting wino and higgsino dark matter at the muon collider with disappearing tracks (2021). `arXiv:2102.11292`.

[309] T. Han, S. Li, S. Su, W. Su, Y. Wu, Heavy Higgs Bosons in 2HDM at a Muon Collider (2021). `arXiv:2102.08386`.

[310] W. Liu, K.-P. Xie, Probing electroweak phase transition with multi-TeV muon colliders and gravitational waves, JHEP 04 (2021) 015. doi:`10. 1007/JHEP04(2021)015`. `arXiv:2101.10469`.

[311] R. Capdevilla, D. Curtin, Y. Kahn, G. Krnjaic, A No-Lose Theorem for Discovering the New Physics of $(g - 2)_\mu$ at Muon Colliders (2021). `arXiv:2101.10334`.

[312] D. Buttazzo, R. Franceschini, A. Wulzer, Two Paths Towards Precision at a Very High Energy Lepton Collider (2020). `arXiv:2012.11555`.

[313] W. Yin, M. Yamaguchi, Muon $g - 2$ at multi-TeV muon collider (2020). `arXiv:2012.03928`.

[314] D. Buttazzo, P. Paradisi, Probing the muon g-2 anomaly at a Muon Collider (2020). `arXiv:2012.02769`.

[315] P. Bandyopadhyay, A. Costantini, Obscure Higgs boson at Colliders, Phys. Rev. D 103 (2021) 015025. doi:`10.1103/PhysRevD.103. 015025`. `arXiv:2010.02597`.

[316] T. Han, Z. Liu, L.-T. Wang, X. Wang, WIMPs at High Energy Muon Colliders, Phys. Rev. D 103 (2021) 075004. doi:`10.1103/PhysRevD. 103.075004`. `arXiv:2009.11287`.

[317] T. Han, D. Liu, I. Low, X. Wang, Electroweak couplings of the Higgs boson at a multi-TeV muon collider, Phys. Rev. D 103 (2021) 013002. doi:`10.1103/PhysRevD.103.013002`. `arXiv:2008.12204`.

[318] R. Capdevilla, D. Curtin, Y. Kahn, G. Krnjaic, Discovering the physics of $(g - 2)_\mu$ at future muon colliders, Phys. Rev. D 103 (2021) 075028. doi:`10.1103/PhysRevD.103.075028`. `arXiv:2006.16277`.

[319] M. Chiesa, F. Maltoni, L. Mantani, B. Mele, F. Piccinini, X. Zhao, Measuring the quartic Higgs self-coupling at a multi-TeV muon collider, JHEP 09 (2020) 098. doi:`10.1007/JHEP09(2020)098`. `arXiv:2003.13628`.

[320] R. Capdevilla, D. Curtin, Y. Kahn, G. Krnjaic, Systematically Testing Singlet Models for $(g - 2)_\mu$ (2021). `arXiv:2112.08377`.

[321] D. Buttazzo, D. Redigolo, F. Sala, A. Tesi, Fusing Vectors into Scalars at High Energy Lepton Colliders, JHEP 11 (2018) 144. doi:`10.1007/ JHEP11(2018)144`. `arXiv:1807.04743`.

[322] M. Aaboud, et al. (ATLAS collaboration), Measurements of Higgs boson properties in the diphoton decay channel with 36 fb^{-1} of pp collision data at $\sqrt{s} = 13$ TeV with the ATLAS detector, Phys. Rev. D 98 (2018) 052005. doi:`10.1103/PhysRevD.98.052005`. `arXiv:1802.04146`.

[323] A. M. Sirunyan, et al. (CMS collaboration), Measurements of Higgs boson properties in the diphoton decay channel in proton-proton collisions at $\sqrt{s} = 13$ TeV, JHEP 11 (2018) 185. doi:`10.1007/JHEP11(2018) 185`. `arXiv:1804.02716`.

[324] F. Ambrogi, C. Arina, M. Backovic, J. Heisig, F. Maltoni, L. Mantani, O. Mattelaer, G. Mohlabeng, MadDM v.3.0: a Comprehensive Tool for Dark Matter Studies, Phys. Dark Univ. 24 (2019) 100249. doi:`10. 1016/j.dark.2018.11.009`. `arXiv:1804.00044`.

[325] E. Aprile, et al. (XENON collaboration), First Dark Matter Search Results from the XENON1T Experiment, Phys. Rev. Lett. 119 (2017) 181301. doi:`10.1103/PhysRevLett.119.181301`. `arXiv:1705.06655`.

[326] C. Amole, et al. (PICO collaboration), Dark Matter Search Results from the PICO-60 C_3F_8 Bubble Chamber, Phys. Rev. Lett. 118 (2017) 251301. doi:`10.1103/PhysRevLett.118.251301`. `arXiv:1702.07666`.

[327] D. S. Akerib, et al. (LUX collaboration), Limits on spin-

dependent WIMP-nucleon cross section obtained from the complete LUX exposure, Phys. Rev. Lett. 118 (2017) 251302. doi:10.1103/PhysRevLett.118.251302. arXiv:1705.03380.

[328] P. A. R. Ade, et al. (Planck collaboration), Planck 2015 results. XIII. Cosmological parameters, Astron. Astrophys. 594 (2016) A13. doi:10.1051/0004-6361/201525830. arXiv:1502.01589.

[329] A. V. Kotwal, S. Chekanov, M. Low, Double Higgs Boson Production in the 4τ Channel from Resonances in Longitudinal Vector Boson Scattering at a 100 TeV Collider, Phys. Rev. D 91 (2015) 114018. doi:10.1103/PhysRevD.91.114018. arXiv:1504.08042.

[330] H. Georgi, D. B. Kaplan, Composite Higgs and Custodial SU(2), Phys. Lett. B 145 (1984) 216–220. doi:10.1016/0370-2693(84)90341-1.

[331] H. Georgi, D. B. Kaplan, P. Galison, Calculation of the Composite Higgs Mass, Phys. Lett. B 143 (1984) 152–154. doi:10.1016/0370-2693(84)90823-2.

[332] D. B. Kaplan, H. Georgi, SU(2) x U(1) Breaking by Vacuum Misalignment, Phys. Lett. B 136 (1984) 183–186. doi:10.1016/0370-2693(84)91177-8.

[333] M. J. Dugan, H. Georgi, D. B. Kaplan, Anatomy of a Composite Higgs Model, Nucl. Phys. B 254 (1985) 299–326. doi:10.1016/0550-3213(85)90221-4.

[334] K. Agashe, R. Contino, A. Pomarol, The Minimal composite Higgs model, Nucl. Phys. B 719 (2005) 165–187. doi:10.1016/j.nuclphysb.2005.04.035. arXiv:hep-ph/0412089.

[335] R. Contino, L. Da Rold, A. Pomarol, Light custodians in natural composite Higgs models, Phys. Rev. D 75 (2007) 055014. doi:10.1103/PhysRevD.75.055014. arXiv:hep-ph/0612048.

[336] F. Bishara, R. Contino, J. Rojo, Higgs pair production in vector-boson fusion at the LHC and beyond, Eur. Phys. J. C 77 (2017) 481. doi:10.1140/epjc/s10052-017-5037-9. arXiv:1611.03860.

[337] R. Contino, D. Marzocca, D. Pappadopulo, R. Rattazzi, On the effect of resonances in composite Higgs phenomenology, JHEP 10 (2011) 081. doi:10.1007/JHEP10(2011)081. arXiv:1109.1570.